CHARACTERIZATION OF THE PROEUTECTOID CEMENTITE NETWORKS OBSERVED
IN THE SAE 1092 WIRE ROD STEEL GRADE

by

Fábio da Silva Borchardt

Metallurgical Engineer, Universidade Federal de Ouro Preto, 1997

Submitted to the Graduate Faculty of

School of Engineering in partial fulfillment

of the requirements for the degree of

Masters of Science in Materials Science and Engineering

University of Pittsburgh

2004

UNIVERSITY OF PITTSBURGH

SCHOOL OF ENGINEERING

This thesis was presented

by

Fábio da Silva Borchardt

It was defended on

April 14, 2004

and approved by

Dr. I. Nettleship, Associate Professor, Materials Science and Engineering Department

Dr. C. I. Garcia, Research Professor, Materials Science and Engineering Department

Thesis Advisor: Dr. A. J. DeArdo, William Keplar Whiteford Professor, Materials Science and
Engineering Department

ABSTRACT

CHARACTERIZATION OF THE PROEUTECTOID CEMENTITE NETWORKS OBSERVED
IN THE SAE 1092 WIRE ROD STEEL GRADE

Fábio da Silva Borchardt

University of Pittsburgh, 2004

Currently, the trend around the world is to produce lighter wires with higher strength for long span bridge applications and the automobile tire industry. Increasing the carbon content in the steel is the most common way to achieve higher strength in these applications. The chosen steel in this study was SAE 1092. The advantage of this steel is its higher strength but the disadvantage is the formation of a brittle phase. In this type of hypereutectoid steel, the proeutectoid cementite precipitates along the austenite grain boundaries prior to the formation of the pearlite. As the amount of carbon increases above the eutectoid point, more of this brittle phase precipitates. At the beginning of this work, two proeutectoid cementite networks were identified; one in the center and the other close to the surface of the wire rod. Electron Backscattered Diffraction (EBSD) was used to crytallographically define that proeutectoid cementite forms at certain grain boundaries of a given orientation. Dilatometric tests were carried out to verify the minimum cooling rate necessary to avoid the formation of the proeutectoid cementite. It was also used to verify the influence of the environment on the transformation of

austenite and the precipitation of the proeutectoid cementite. Industrial experiments were also carried out in order to determine what conditions should be used to produce wire rods with large diameters and free of proeutectoid cementite network.

TABLE OF CONTENTS

LIST OF TABLES

LIST OF FIGURES

xi

xiv

ACKNOWLEDGEMENTS

1.0 INTRODUCTION

Recently, lighter, higher-strength materials have been demanded by customers. Important applications such as long-span bridges, rails, high-rise buildings, and automobiles are examples of these demands. The automotive industry has been working to reduce the weight of the cars using stronger materials. The goal is to manufacture cars that are lighter, thus, saving money by using thinner gage steel while maintaining strength and resistance against impact. The reduction in weight while increasing the strength and crash worthiness, are the driving forces in the continued use of steel in the automotive industry. The advantages for the consumers in purchasing lighter vehicles are: economical fuel consumption and safety.

One of the heaviest components of the cars is the tire, so great efforts have been made in order to produce a lighter tire. To reduce the weight, one of the options is to reduce the amount of steel cord used to reinforce it. To do so, the cord strength has to be increased in order to allow the manufactures to have the same final strength in the tires with less material.[1] Figure 1.1 shows how the reinforcement is built. It consists of very fine cords of hard drawn steel filaments. The cords have a diameter of 0.5mm up to 3.0mm and are composed of an assembly of hard drawn steel filaments. The filament size ranges from 0.15 up to 0.40mm in diameter.[2]

---

[1] Parenthetical references placed superior to the line of the text refer to the bibliography.

1
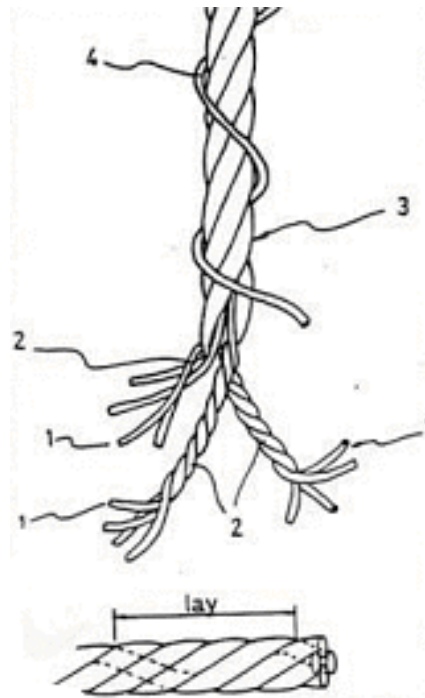
Figure 1.1 – Steel cord components.: 1) Wire filament, 2) Strand, 3) Cord, 4) Wrap

Traditionally, the high carbon steel containing approximately 0.72wt%C was used to produce tire cord steel. Currently, high carbon steel with eutectoid carbon content is used in this application since it can be easily strengthened by cold drawing.[3] The microstructure of this steel is a typical fine lamellar structure. It has been known that the lamellar spacing is controlled by the transformation temperature and is related to the mechanical properties. The lamellar spacing can be reduced to about 0.1 µm by heat treatment using a molten lead bath known as patenting.[4]

As pointed out by Y. Kanetsuk et al.,[4] it is difficult to obtain a fine lamellar spacing in the core of a thick wire rod due to the mass effect during the patenting. Therefore, many researchers have tried to increase the strength of the wire by improving the hardenability using

alloying elements, such as chromium, in order to obtain fine and homogeneous lamellar spacing distribution in a thick wire rod.

The strength of the wire with enough tensile and torsional ductility, which is required for industrial use, depends on the wire diameter because the larger the wire rod diameter, the lower the maximum drawing strain without generating delamination (longitudinal splitting of the wire in shear bands) during torsional deformation.[4] The strength of the carbon steel increases with the carbon content. The potential for increasing the strength of wires used as tire cord is illustrated in Figure 1.2, which shows wire strength as a function of carbon content.[5] The wire diameter (0.28mm) and the amount of cold work are constant for all data points given as solid marks. The ultrahigh-carbon steels (UHCSs) are projected to have wire strengths in excess of 4000MPa. These ultrahigh strength UHCS wires are expected to be significantly stronger than the 3400MPa wire currently used in premium tires. At 1.8wt%C, the UHCS wires are projected to have a strength approaching 6000MPa. Therefore, the strength of hypereutectoid steel is higher than the strength of the eutectoid steel. However, the hypereutectoid steel has not been so used for steel wire because of its lower drawability due to the cementite forming at grain boundaries when it is cooled from the austenite range.

The properties produced in UHCS are superior to those found in eutectoid carbon steel and are important for commercial high strength wire and rod applications including tire cord, bridge cable, wire rope, reinforcing bar, springs and drill rod. A good example of these improved properties is the ultrahigh strength obtained in high carbon steel wire that is used in tires for automobiles and light trucks. This ultrahigh strength wire is the primary component that defines the structural performance of the tire as well as its weight and rolling resistance.
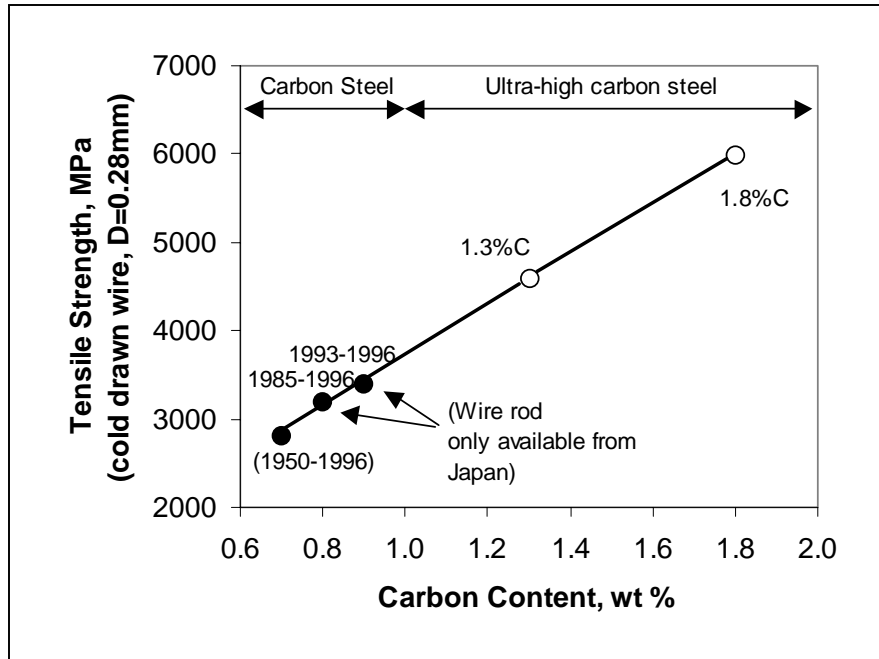
Figure 1.2 – Influence of carbon content on the strength of cold drawn steel wire. Current premium radial tires use high carbon steel wire with a strength of 3400MPa. The projected strengths for ultrahigh carbon steels containing 1.3wt% and 1.8wt%C are shown in figure by open circle symbols.

Proeutectoid cementite at grain boundaries has been identified as a source of embrittlement in high carbon steels. This proeutectoid cementite can be eliminated by the use of the patenting process, i.e., isothermal transformation in a Pb bath. However, this process raises production costs, thereby decreasing its competitiveness. Another deterrent in using the patenting process is the environmental concerns over the pollution of the Pb fumes.

Tempering can also be used to eliminate the proeutectoid cementite by means of spheroidization.[6] Figure 1.3 shows an spheroidizing structure compared to an air cooled structure that shows the proeutectoid cementite network. However, tempering also increases the production costs as well as changing the lamellar structure to a spheroidized one.

4
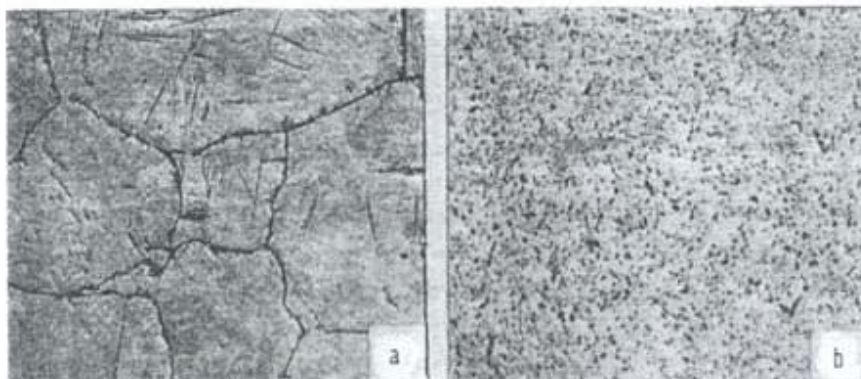
Figure 1.3 – Two different structures are shown: 2a) air cooled structure; 2b) tempered structure[6]

Another possible option is to add alloying element, which has been a cheap, and successful choice. Silicon has great influence on the precipitation behavior of cementite, as shown by Heckel and Paxton.[7] They suggested that the nucleation and growth of proeutectoid cementite depended on the rate of silicon rejection from the austenite grain boundary by diffusion because of a lower solubility of silicon in cementite. Cobalt [4,5] can also be used to suppress the formation of cementite due to its low solubility in cementite. In the case of cobalt, the partitioning coefficient is 0.23.[4] Nickel has many physical properties similar to those of cobalt, such as atomic size, melting point and density.[8] Hence, it is a likely potential element to suppress the proeutectoid cementite formation during transformation. Other elements will also be included in this research in order to clarify and improve the knowledge of the potential elements on the suppression of the proeutectoid cementite.

The last option would be an increase of the cooling rate. Since the formation of the proeutectoid cementite and the pearlite are the result of the nucleation and growth processes, the sooner the pearlite reaction starts the less proeutectoid cementite should be formed. Hence, for each steel grade there will be a minimum cooling rate necessary to suppress the formation of the proeutectoid cementite network.

2.0 BACKGROUND

2.1 STRENGTHENING MECHANISMS

One way to increase the strength of steel is to provide a large amount of cold work. This increase in cold work causes a decrease in the grain size, and, according to the Hall-Petch equation, discussed by A. J. DeArdo et al.,[9] the yield strength varies as the inverse square root of the ferritic grain size, as shown in Equation (2.1);

$$\sigma_y = \sigma_0 + kd^{-1/2} \tag{2.1}$$

where σ_y is the yield strength, σ_0 is the resistance to dislocation motion, and d is the average grain size.

This is just one of the strengthening mechanisms that could be applied. Dislocations, precipitation, and texture are other examples of strengthening mechanisms that could be applied. However, the main approaches for increasing the wire strength have been to increase, incrementally, the carbon content used in high carbon steels for tire cord (solid solution strengthening), and the amount of cold work.

Furthermore, as shown by Eric M. Taleff et al.,[10] the strengthening mechanisms contribute to the yield strength in an additive manner and, for eutectoid and hypereutectoid steels, the following equation has been derived.

$$\sigma_y = (\sigma_0)_{SS} + 145(D^*s)^{-1/2} + 460(L)^{-1/2} \tag{2.2}$$

7

where σ_y is the yield strength, $(\sigma_0)_{SS}$ is the resistance to dislocation motion resulting from solid solution atoms, $(D_s^*)^{-1/2}$ is the carbide spacing (interlamellar spacing or particle spacing) and L is the ferrite grain size or pearlite colony size.

A further equation was developed by Donald R. Lesuer et al.,[5] where, by analogy with the experimental work of Taleff et al.,[10] one might expect that the strength of a pearlitic steel results from the sum of strengthening contributions from different barriers to dislocation motion. Thus for a severely worked pearlitic steel,

$$\sigma_y \quad = \quad (\sigma_0)_{SS} \quad + \quad \sigma_{pearlite} \quad + \quad \sigma_{colony} \quad + \quad \sigma_{cell} \tag{2.3}$$

where $(\sigma_0)_{SS}$, $\sigma_{pearlite}$, σ_{colony} and σ_{cell} represent the resistance to dislocation motion resulting from solid solution additions ($(\sigma_0)_{SS}$), pearlite spacing ($\sigma_{pearlite}$), pearlite colony size (σ_{colony}) and dislocation cell size (σ_{cell}). The $(\sigma_0)_{SS}$, $\sigma_{pearlite}$, σ_{colony} terms for hypereutectoid steels are given in equation (2.2). The σ_{cell} term is shown as a function of drawing strain in Fig. 2.1 (assuming in a severely drawn wire that the yield strength equals the tensile strength). The data in Fig. 2.1 suggests that for severely drawn wire, the cell size dominates the strength of the wire, and the pearlite spacing and pearlite colony size are secondary contributions.

2.2 CEMENTITE

Cementite, or iron carbide, contains 6.67wt%C, corresponding to the formula Fe_3C. In carbon alloy steels, some of the carbide-forming elements, for example, manganese and chromium, will replace some of the iron in cementite. Therefore, the formula for cementite is often referred to as M_3C, where M represents the carbide–forming elements present. Pure Fe_3C has a hardness value

of 800 HV and is brittle. Substituting other elements for some of the iron in cementite will increase the hardness appreciably. Because of the brittleness of cementite, only limited amounts are permitted to be present in steels.[11]
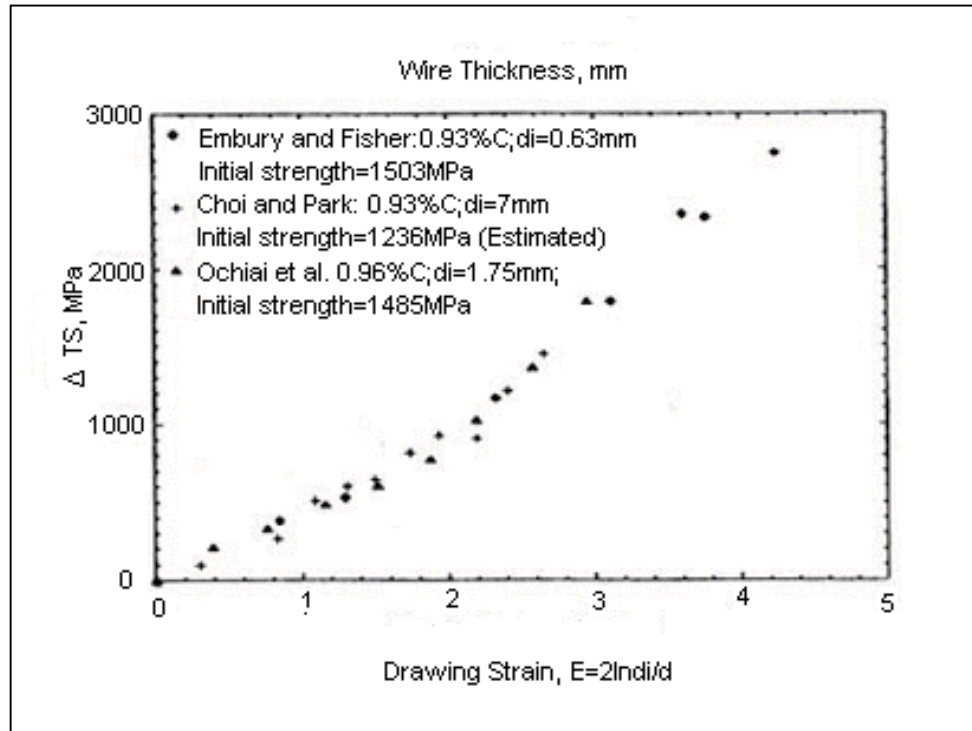
Figure 2.1 - Strength increment as a function of wire drawing strain in hypereutectoid steels with similar composition.

In order to make the effect of silicon more clear, M. Kaiso et al.[3] made a further nano-order microstructure observation by transmission electron microscopy (TEM). Figure 2.2 shows a schematic illustration of cementite in pearlite and the observation directions for TEM.

The cementite structure is orthorhombic with 12 iron atoms and 4 carbon atoms in the unit cell. Its cell dimensions are a = 4.5155Å, b = 5.0773Å and c = 6.7265Å [12] or a = 5.0896Å,

9

b = 6.7443Å and c = 4.5248Å.[13] Therefore, these two authors are in good agreement with respect to the cementite unit cell dimensions.

In cubic close-packed (FCC) iron, (γ-Fe), the volume per atom is 11.47Å^3, and in the body-centered structure (α-Fe), it is about 3 percent greater. The corresponding free volume per iron atom in Fe$_3$C is 12.94 Å^3. This is 12 percent greater than the close-packed volume. Cementite has a different crystal structure and is an ordered compound. Pearlite is composed of approximately 12 percent of cementite. The iron lattice in the cementite structure differs from that of a close-packed structure by reason of the necessity to accommodate carbon atoms in the ratio of 1:3.[13]
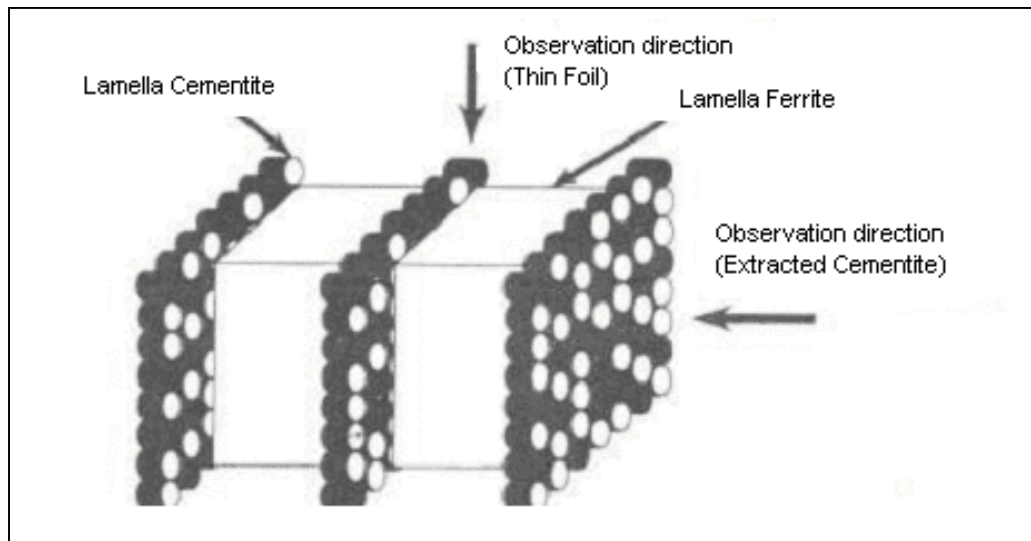
Figure 2.2 - Three-dimensional schematic illustration for nano substructure of lamellar cementite.

W. J. Kim and O. D. Sherby [14] measured the influence of the volume fraction of the cementite on the hardness. Figure 2.3 clearly shows that hardness increases as volume fraction of

cementite (or carbon content) increases. This result indicates that the strength of the cementite phase is much higher than that of the ferrite phase at low temperatures.[14] They also measured the influence of the volume fraction of cementite (or carbon content) on the superplasticity. Figure 2.4 shows the tensile elongation data from ingot-processed Fe-C alloys as a function of volume fraction of cementite at a given temperature (923K) and strain rate (1.64×10^{-4} s^{-1}). Some data obtained under different testing conditions are also plotted. As can be seen from the plot, tensile ductility of the ingot processed Fe-C alloys is increased as carbon content increases from 0.8 (12%Fe_3C) to about 1.6wt%C (24%Fe_3C), and has its optimum value of elongation between 1.6 (24%Fe_3C) and 1.8wt%C (27%Fe_3C). Tensile elongation, however, starts to decrease with an increase in carbon content beyond 1.8wt%C (27%Fe_3C). The increase of tensile ductility with carbon content, observed between 0.8 (12%Fe_3C) and 1.8wt%C (27%Fe_3C), can be attributed to an increase in the volume fraction of proeutectoid cementite. The increase of fine cementite particles per unit volume provides more pinning points for grain boundaries. This effect, in turn, reduces the grain growth rate, and thus the initial fine-grained microstructure can be maintained throughout testing. The decrease of tensile ductility above 2.1wt%C (31.5%Fe_3C) can be explained by the impossibility of obtaining a fully austenitic structure at any temperature. As a consequence, undissolved coarse cementite particles remain even after the solid solution treatment. These carbides are extremely difficult to be refined by subsequent thermo-mechanical treatments and tend to reduce tensile ductility by providing sites for cavity formation.[14]
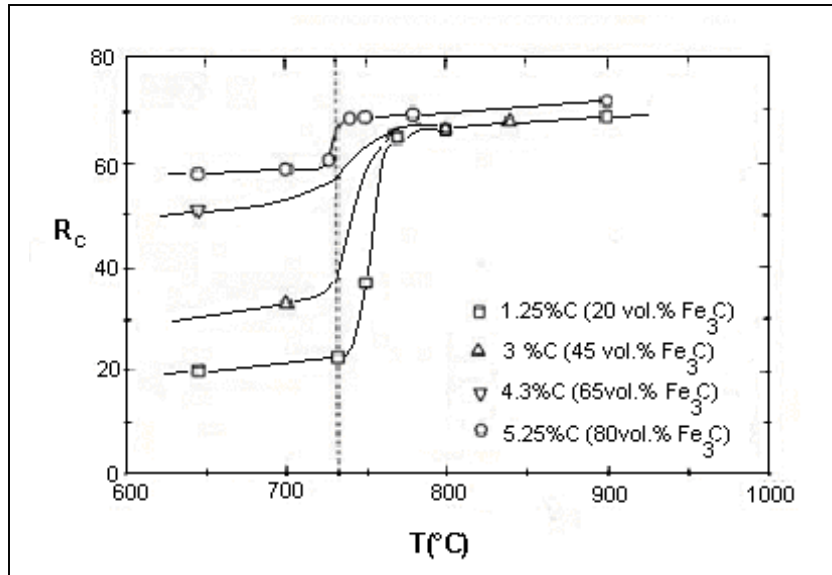
Figure 2.3 - Hardness test results for Fe-C alloys.
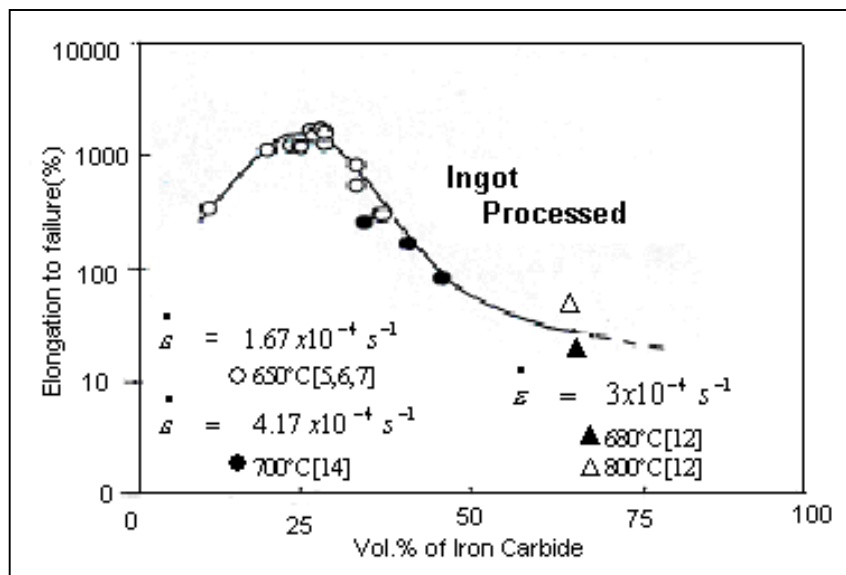
Figure 2.4 - Tensile elongation data as a function of volume fraction of cementite.

12

During wiredrawing, lamellar cementite undergoes partial dissolution and 20~50 percent of the volume fraction of the initial cementite dissolves[18] during wiredrawing. Decomposition of the cementite supplies carbon atoms for dislocation pinning; the process involves an activation energy of 28Kcal/mol. This phenomenon is generally associated with the second stage aging. However, as stated by Gonzalez et al.,[15] cementite decomposition in drawn and aged pearlitic steels occurs during deformation and not during aging.

The strength of drawn wires is significantly affected by the cementite at large deformations since cementite is plastically deformed and hardened, and the cementite/ferrite interface acts as the dislocation generation and sink source.

2.3 PROEUTECTOID CEMENTITE

In steel with carbon content higher than the eutectoid composition (hypereutectoid steels), proeutectoid cementite exists along the austenite grain boundaries prior to the formation of pearlite, and it is often crystallographically continuous with pearlitic cementite.[16] The cementite formed upon cooling between Ar_{cm} and Ar_1 is referred to as proeutectoid cementite. Figure 2.5 shows an example of proeutectoid cementite in hypereutectoid steel. The cementite has formed as a thin network along the grain boundaries of the austenite, and the balance of the microstructure is martensite, which formed when the specimen was quenched from a temperature between A_{cm} and A_1. A much closer examination made by M. V. Kral and G. Spanos [17] shows that the cementite grain boundary film reveals "fernlike" or "dendritic" characteristics, as illustrated on Figure 2.6 a. It is seen in plane views of a grain boundary film that the fernlike cementite precipitates cover austenitic grain boundaries (Figure 2.6 b). In a higher magnification

micrograph, it is possible to see the cementite morphology exhibiting primary and secondary dendritic arms (Figure 2.6 c). Dendrite arms extend only along austenite grain boundaries or along grain edges at triple junctions; however, they do not reach into grains.[17]

The cementite and its interfaces are preferred sites for fracture initiation and propagation, and, as a result, proeutectoid cementite networks make hypereutectoid steels extremely brittle. Therefore, the increase of the carbon content in steels reduce the drawability due to the increase in the volume fraction of cementite, as a hard phase.[18] Intercritical annealing treatments that break up and spheroidize the cementite are, therefore, used to increase toughness.[6,19]
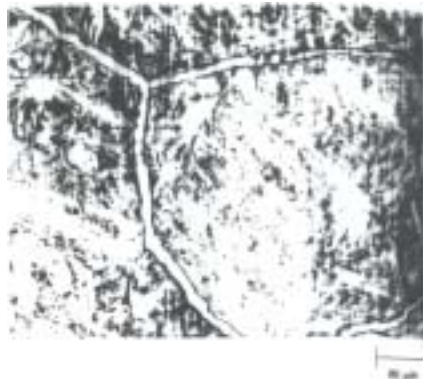
Figure 2.5 - Light micrograph showing cementite network on prior-austenite grain boundaries in an Fe-1.12wt%C - 1.5wt%Cr alloy.
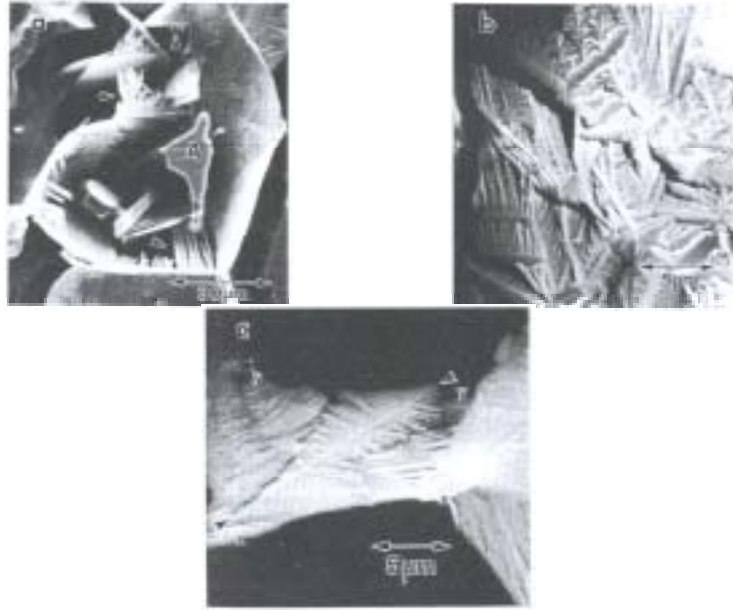
Figure 2.6 - SEM micrographs of deep etched samples. a) cementite grain boundary film with "fernlike" or "dendritic" features. b) fernlike cementite precipitates covering austenitic grain boundaries. c) cementite morphology exhibiting primary and secondary dendritic arms.

The precipitation of thick proeutectoid cementite onto the austenite grain boundaries deteriorates the drawability of wire rod. In order to extend the application of hypereutectoid steel from a limited sphere such as needles, tools, etc., to general wire products, it is critical to make the precipitation behavior of proeutectoid cementite clear and establish a suppression technique to avoid its precipitation.[20] Toughness is another property that is deteriorated as cementite films cover more of the austenite grain boundaries.[21] Steels with the same grain size, pearlite content, carbide grain boundary network, and strength can differ significantly in impact transition temperature; this has been related to differences in carbide film thickness.[21]

The effect of substitutional solutes on the suppression of cementite formation has long been a subject of considerable interest. Although several researchers have been studying the

15

effect of various alloying elements on cementite precipitation, the prediction of how each element will modify the rate of precipitation, the type of precipitate, and nucleation sites is not completely understood. An alloying element having a higher solubility in the carbide than in ferrite is not likely to have a large effect on the rate of growth of the carbide, although it may govern the structure of the carbide precipitated, the rate of nucleation, and the nucleation sites. On the other hand, if the alloying element is essentially insoluble in the carbide, it can have a very large effect on the rate of growth of the carbide.[22]

2.4 PEARLITE

Pearlite is a microconstituent composed of two phases; ferrite and cementite. It results from an eutectoid transformation when austenite, containing approximately 0.78wt%C is cooled below the A1 temperature. When the austenite is cooled below A1 temperature, the austenite becomes simultaneously supersaturated with respect to cementite and ferrite. This reaction is represented as:

$$\gamma \ \rightarrow \ \alpha \ + \ Fe_3C$$
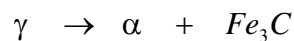
In the case of Fe-C alloys, the pearlite has a lamellar pattern with the alternated laths of cementite and ferrite, as shown in Figure 2.7.
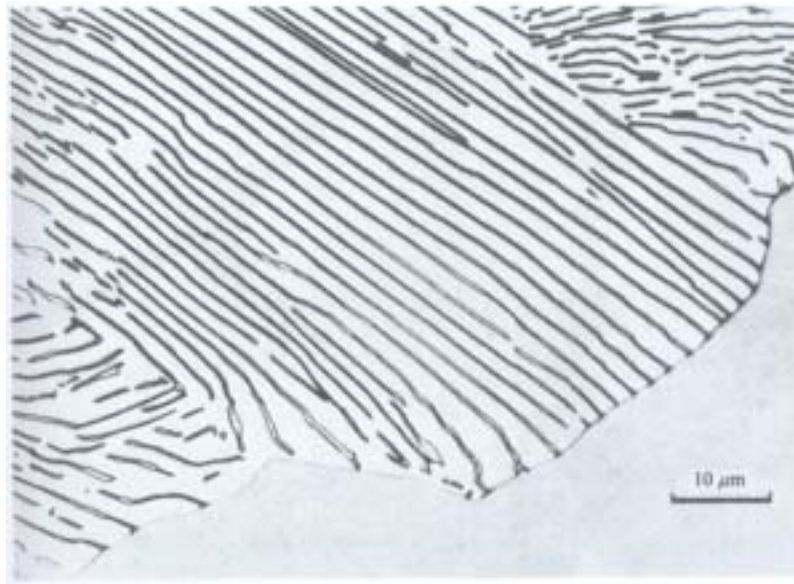
Figure 2.7 - A pearlite colony advancing into an austenite grain.

Pearlite nodules nucleate on grain boundaries and grow with a roughly constant radial velocity into the surrounding austenite grains.[23,24] The number of pearlite nodules that nucleates is proportional to the undercooling below A1 and the austenitic grain size. The finer the austenitic grain size, the higher the rate of isothermal transformation.[24] In other words, if the undercooling below A1 is small, the number of nodules is small and can grow as hemispheres or spheres without interfering with each other. On the other hand, if the undercooling is large, the nucleation rate is much higher and site saturation occurs. That is, all boundaries become quickly covered with nodules which grow together forming layers of pearlite outlining the prior austenite grain boundaries, Figure 2.8.
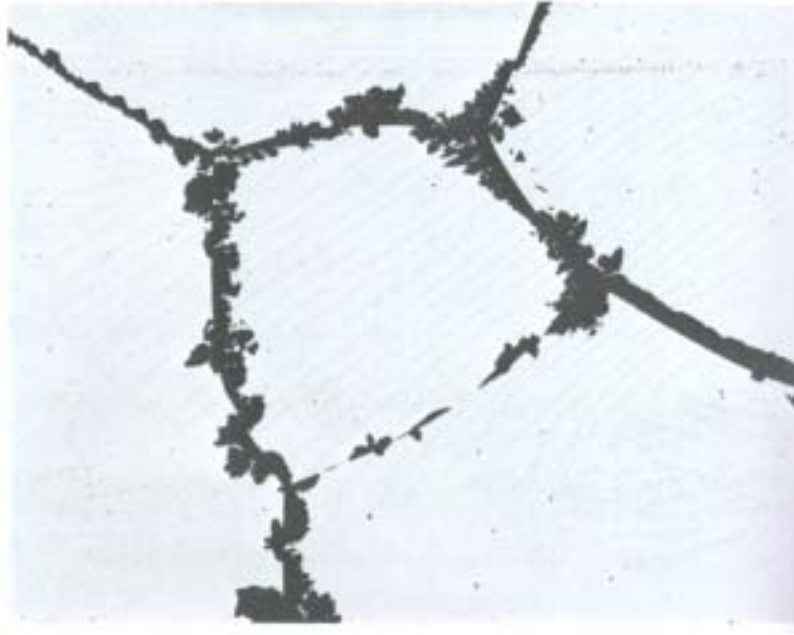
Figure 2.8 - A partially transformed eutectoid steel. Pearlite has nucleated on grain boundaries and inclusions (100X).

2.4.1 Nucleation of Pearlite

The first stage in the formation of pearlite is the nucleation of either cementite or ferrite on an austenite grain boundary. Depending on the grain boundary structure, the cementite will form prior to or after the formation of ferrite. In other to clarify this mechanism, let us suppose cementite forms first. The cementite will minimize the activation energy barrier to nucleation. The austenite surrounding this nucleus will become depleted of carbon, which will increase the driving force for the precipitation of ferrite, and a ferrite nucleus forms adjacent to the cementite. If this process is repeated, the colony will spread along the grain boundary.[23]

When the alloy composition does not correspond to the eutectoid point, either proeutectoid ferrite or proeutectoid cementite might be covering the austenitic grain boundary prior to the eutectoid transformation.

The nucleation of pearlite requires the establishment of cooperative growth of the two phases. This takes time and the rate of colony nucleation, therefore, increases with time. In some cases, this cooperation is not established and the ferrite and cementite grow in a non-lamellar manner producing so-called degenerate pearlite.[23]

2.4.2 Pearlite Growth

The pearlite growth in binary Fe-C is similar to the lamellar eutectic with austenite replacing the liquid.

The minimum possible interlamellar spacing, (S*), varies inversely to the undercooling below the eutectoid temperature (A1),[23,24] and assuming the observed spacing, (S_0), is proportional to S*, gives

$$S_0 \quad \alpha \quad S* \quad \alpha \quad (\Delta T)^{-1} \tag{2.4}$$

The growth rate of pearlite is given by the following relationship

$$v \quad = \quad kD_C^\gamma (\Delta T)^2 \tag{2.5}$$

where k is a thermodynamic term which is roughly constant, D_C^γ is the diffusion coefficient of carbon in the austenite phase, and ΔT is the undercooling below the A1 line.

The lamellar spacing has been observed to vary between 1μm at high temperatures and approximately 0.1μm at the lowest temperatures. However, it has been noticed that the S_0 is usually twice as great as the S*. That means that the maximum growth rate criterion is not what

19

determines the observed spacing. Therefore, it can be determined by the need to create new cementite lamellae as the perimeter of the pearlite nodules increases.

Figure 2.9 shows measured and calculated growth rates as a function of temperature. The calculated line is based on an equation similar to Equation 2.5 and shows that the measured growth rates are reasonably consistent with volume-diffusion control.
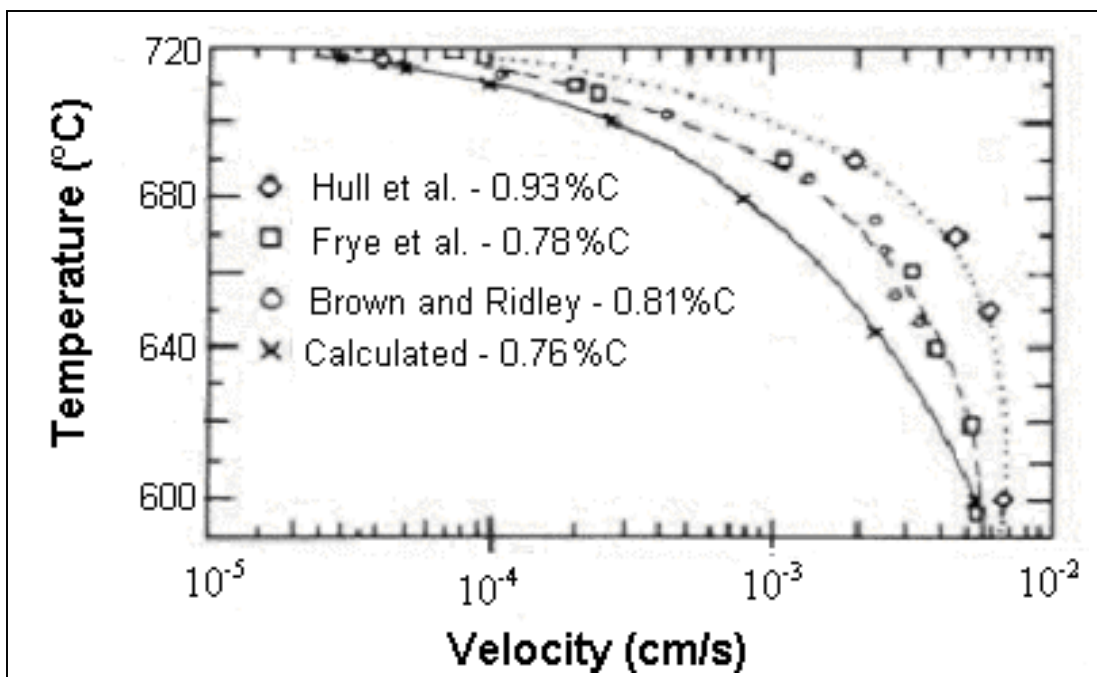
Figure 2.9 - Pearlite growth rate vs. temperature for plain carbon steels.

2.4.3 Pearlite in Off-Eutectoid Fe-C Alloys

If austenite containing less or more carbon than the eutectoid point is isothermally transformed below the A1 temperature, a proeutectoid phase will form before the formation of the pearlite. Therefore, if an Fe-C alloy containing less carbon than the eutectoid point is cooled from the austenitic region, some proeutectoid ferrite will be formed. On the other hand, if an Fe-C alloy contains more carbon than the eutectoid point, proeutectoid cementite is expected to form. However, if the departure from the eutectoid composition is not too great, both proeutectoid phases can be avoided by increasing the undercooling temperature below A1. The region in which this is possible corresponds, approximately, to the condition that the austenite is saturated simultaneously with respect to both cementite and ferrite; i.e. the hatched area in Figure 2.10.
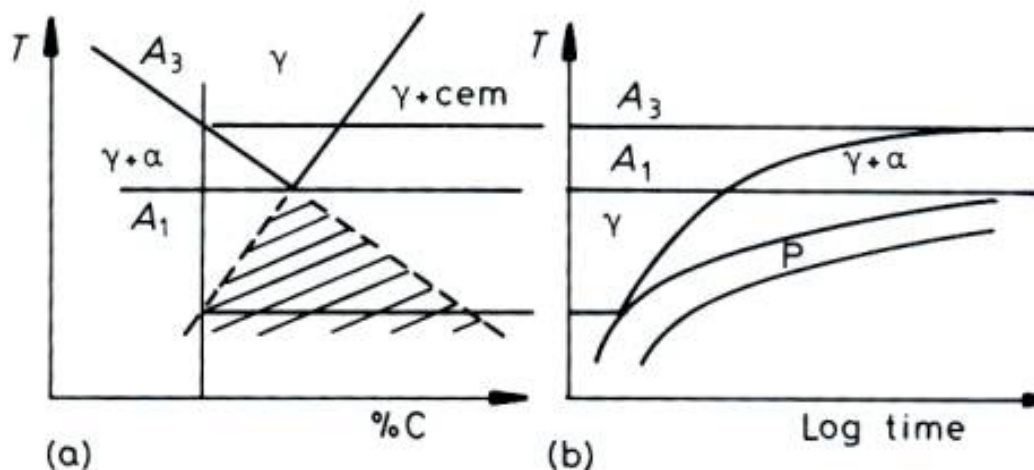
Figure 2.10 - Effect of transformation temperature on the volume fraction of proeutectoid ferrite.

2.5 INFLUENCE OF ALLOYING ELEMENTS ON THE SUPPRESSION OF PROEUTECTOID CEMENTITE AND MECHANICAL PROPERTIES

Besides those elements already mentioned to be effective for the suppression of the proeutectoid cementite, a couple of others have also been studied. Table 2.1 shows a comparison of the properties of cobalt, silicon, manganese, phosphorus, copper, aluminum, chromium, boron, vanadium, niobium, and nickel. Whether or not these elements play a role on the suppression of the cementite network is discussed in this section. Niobium and nickel are the only exceptions because no study on the suppression of the cementite network by these elements was found by the author.

Table 2.1: Properties of cobalt, silicon, nickel, copper, manganese, vanadium, boron, aluminum, niobium, phosphorus, and chromium.[25]

Property		Co	Si	Ni	Cu	Mn	V	B	Al	Nb	P	Cr
Atomic number		27	14	28	29	25	23	5	13	41	15	24
Atomic weight		58.9	28.1	58.7	63.55	54.93	50.9	10.8	26.9	92.9	30.97	51.9
Boiling point [°C]		2927	2900	2913	2927	2061	3407	3927	2519	4744	277	2671
Melting point [°C]		1495	1414	1455	1084	1246	1910	2076	660	2477	44.2	1907
Density of solid [$kg*m^{-3}$]		8900	2330	8908	8920	7470	6110	2460	2700	8570	1823	7140
Molar volume [cm^3]		6.67	12.1	6.58	7.11	7.35	8.32	4.39	10.00	10.8	17.02	7.23
Velocity of sound [$m*s^{-1}$]		4720	2200	4970	3570	5150	4560	16200	5100	3480	-	5940
Atomic radius [pm]		135	110	135	135	140	135	85	125	145	100	140
Covalent radius [pm]		126	111	121	138	139	125	82	118	137	106	127
Van der Waals radius [pm]		-	210	163	140	-	-	-	-	-	180	-
Young modulus [Gpa]		209	47	200	130	198	128	-	70	105	-	279
Bulk Modulus [Gpa]		180	100	180	140	120	160	320	76	170	11	160
Mineral hardness		5.0	6.5	4.0	3.0	6.0	7.0	9.3	2.75	6.0	-	8.5
Electrical resistivity [$10^{-8}\Omega m$]		6	$1x10^5$	7.0	1.7	160	20	$>1x10^{12}$	2.65	15	10	12.7
Reflectivity [%]		67	28	72	90	-	61	-	71	-	-	-
Electron affinity [$kJ*mol^{-1}$]		63.7	133.6	112	118.4	0	50.6	26.7	42.5	86.1	72	64.3
Electron Binding energies	K 1S [ev]	7709	1839	8333	8979	6539	5465	188	1559	18986	2146	5989
	2S [ev]	925.1	149.7	1009	1097	769.1	626.7	-	117.8	2698	189	696
	2p ½ [ev]	793.2	99.8	870	952.3	649.9	519.8	-	72.9	2465	136	583.8
	2p 3/2 [ev]	778.1	99.2	852.7	932.7	638.7	512.7	-	72.5	2371	135	574.1
Pauling electronegativity		1.88	1.90	1.91	1.90	1.55	1.63	2.04	1.61	1.60	2.19	1.66
Sanderson electronegativity		2.56	2.14	1.94	1.98	2.20	1.39	2.28	1.71	1.42	2.52	1.66
Allred Rochow Electronegativity		1.70	1.74	1.75	1.75	1.60	1.45	2.01	1.47	1.23	2.06	1.56
Bond length [pm]		250.6	235.2	249.2	255.6	273.1	262.2	258.9	286.3	286	221	249.8
Thermal conductivity [$W*m^{-1}*K^{-1}$]		100	150	91	400	7.8	31	27	235	54	0.236	94
Coefficient of linear thermal expansion [$K^{-1}*10^6$]		13.0	2.6	13.4	16.5	21.7	8.4	6	23.1	7.3	-	4.9
Enthalpy of fusion [$kJ*mol^{-1}$]		16.2	50.2	17.2	13.1	13.2	22.8	50	10.7	26.8	0.64	20.5
Entalpy of Vaporization [$kJ*mol^{-1}$]		375	359	378	300	220	453	507	293	690	12.4	339
Enthalpy of atomization [$kJ*mol^{-1}$]		426	456	431	338	281	515	563	326	733	315	397

Table 2.1. Continued

Property	Co	Si	Ni	Cu	Mn	V	B	Al	Nb	P	Cr
$\Delta_f H°$ (solid) [kJ/mol]	0	0	0	0	0	0	0	0	0	0	0
$\Delta_f G°$ (solid) [kJ/mol]	0	0	0	0	0	0	0	0	0	0	0
S° (solid) [J/K*mol]	30.0	18.81	29.9	33.15	32	28.9	5.9	28.3	36.4	41.1	23.8
$C_p H$ (solid) [J/K*mol]	24.8	20.0	26.1	24.4	26.3	24.9	11.1	24.4	24.6	23.8	23.3
$H°_{298.15}$ (solid) [kJ/mol]	4.7	3.22	4.79	5.0	5.0	4.64	1.22	4540	5.25	5.4	4.06
$\Delta_f H°$ (gas) [kJ/mol]	452	450	430	337.4	281	514.2	565.0	330	726	58.9	397
$\Delta_f G°$ (gas) [kJ/mol]	380	411	385	298.6	238	453.2	529.0	286	681	24.5	352
S° (gas) [J/K*mol]	179.4	167.9	182.1	166.4	173.6	182.2	153.4	164.5	186	280	174.4
$C_p H$ (gas) [J/K*mol]	23.02	22.3	23.4	20.8	20.8	26.01	20.8	21.4	30.2	67.2	20.8
$H°_{298.15}$ (gas) [kJ/mol]	6.36	7.6	6.8	6.2	6.2	4.0	6.3	6.9	8.36	14.1	6.20

2.5.1 Influence of Cobalt on the Suppression of the Proeutectoid Cementite

2.5.1.1 Influence of Cobalt Addition on the Transformation Behavior of Hypereutectoid Steel.
Table 2.2 shows the chemical composition for the steels used by Yutaka Kanetsuki, [4] in order to
study the influence of cobalt on cementite precipitation.

Table 2.2: Chemical composition of the steels (wt%).

Steel	C	Si	Mn	P	S	Cu	Co
A	1.01	0.20	0.48	0.004	0.002	<0.01	0.49
B	1.15	0.23	0.52	0.008	0.003	<0.01	0.98
C	1.15	0.21	0.49	0.005	0.002	<0.01	0.51
D	1.14	0.22	0.52	0.005	0.002	<0.01	1.96
E	1.28	0.19	0.50	0.004	0.005	<0.01	3.05
F	1.48	0.19	0.49	0.001	0.004	<0.01	2.98

Figure 2.11 shows the results observed by SEM as a function of carbon and cobalt
contents. Solid marks indicate the specimens with grain boundary cementite and/or
Widmanstätten cementite after the patenting treatment and the open marks indicate a fully
pearlitic microstructure without grain boundary cementite. It was indicated in Figure 2.11 that
the addition of cobalt was effective to avoid the formation of the proeutectoid cementite in
hypereutectoid steels with carbon content up to 1.3wt%.

Figure 2.12 shows the hardness distribution of the steels B to D in patented and air cooled
conditions. Broken lines represent the precipitation of proeutectoid cementite, and solid lines

represent the suppression of the precipitation. This figure shows that suppression of proeutectoid cementite was also influenced by the cooling rate.

The addition of cobalt in the steel decreases its hardenability.[8] Cobalt also has some influence on the lamellar spacing. The lamellar spacing shows a slight dependence on the amount of cobalt, a strong dependence on carbon content and the conventional dependence on transformation temperature.[4]
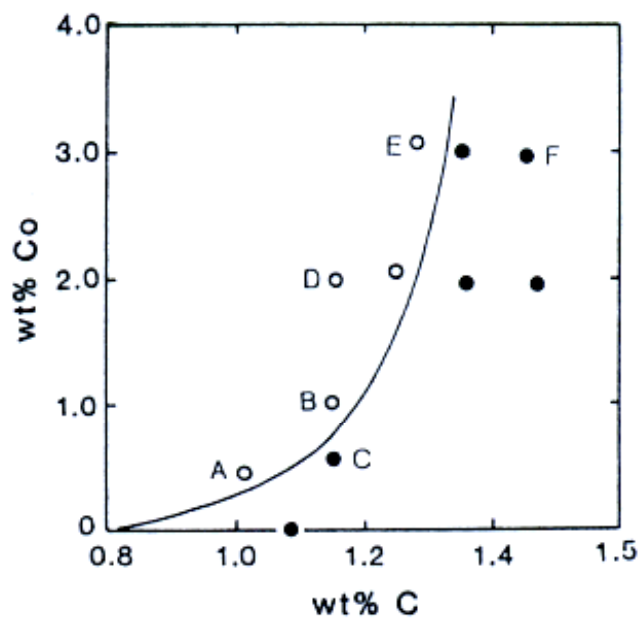
A-F: Steel code shown in Table 2.2
○ : Grain boundary precipitation free
● : Grain boundary precipitation observed

Figure 2.11 - Relation between carbon and cobalt contents required for suppression of the grain boundary cementite and/or Widmanstätten cementite precipitation.
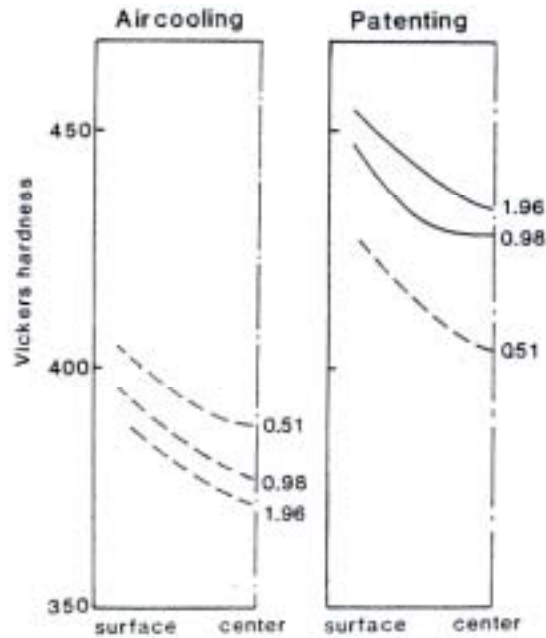
Broken lines: The samples that grain boundary cementite and/or Widmanstätten cementite were observed.
Numbers: The cobalt content (wt%)

Figure 2.12 - Effect of cooling conditions and cobalt addition on the hardness distribution and morphology change of 1.15 wt% C steels. (Steels B and D).

2.5.1.2 Mechanical Properties of Drawn Hypereutectoid Steel. Wires Figure 2.13 shows the mechanical properties of drawn wires as a function of drawing strain. Compared with the strength of the eutectoid indicated by the broken line in Figure 2.13, the tensile strength of steels A and B have increased. The ductility was enough to be drawn up to a drawing strain of 2.5.

Figure 2.14 shows that there is a linear relationship between ductility and carbon content. The amount of decrease in ductility of hypereutectoid steel wire is small.[4]
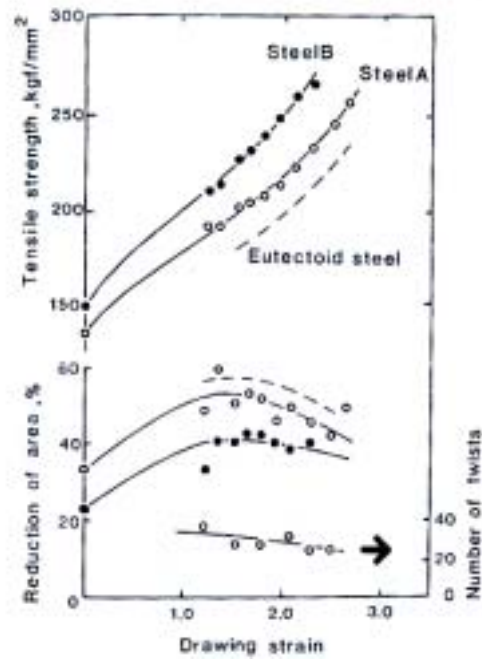
Figure 2.13 - Mechanical properties of drawn hypereutectoid steels with cobalt addition compared with eutectoid steel shown by broken lines.
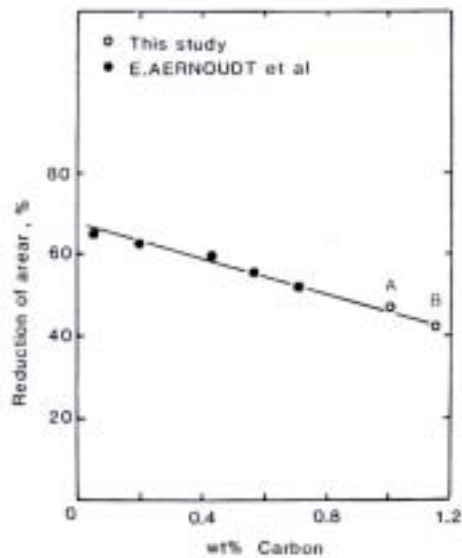
Figure 2.14 - Relation between ductility of the wires drawn up to $\varepsilon = 1.5$ and the carbon content. Ductility was evaluated by reduction of area after tensile testing.

28

2.5.1.3 Effect of Cobalt Addition on the Precipitation of Grain Boundary Cementite. In the case of the silicon-bearing hypereutectoid steel, Heckel and Paxton suggested that nucleation and growth of proeutectoid cementite depended on the rate of silicon rejection from the austenite grain boundary by diffusion because of a lower solubility of silicon in cementite.[7] In the case of cobalt, the partitioning coefficient is 0.23.[4] The suppression of boundary cementite precipitation by cobalt addition is caused not only by the low partitioning of cobalt in cementite but also by other factors, such as the diffusion rate of cobalt and the chemical reaction with carbon in the austenite phase.[4]

Ikuo Ochiai et al., have also suggested that Co can be used in order to suppress the formation of cementite. [20]

2.5.1.4 Drawability of Cobalt-Bearing Hypereutectoid Steel. Houin et al. showed the lamellar spacing of hypoeutectoid steel with a fully pearlitic microstructure as a function of carbon content.[26] Figure 2.15 shows that the lamellar spacing is reduced by increasing the carbon content and saturates at about 1.3wt%C. It also seems that tensile strength increases linearly with increasing carbon content. In the case of a plain eutectoid steel, when the cooling rate is increased, the transformation temperature and the interlamellar spacing decrease, as shown in Table 2.3.[26] The drawability of the fully pearlitic microstructure of both the hypereutectoid and the eutectoid steel is good. The tensile strength and the work hardening rate increased due to the increase in carbon content.[4] The increase of the tensile strength due to the refined interlamellar spacing, is also reported by C. M. Bae.[18]

Table 2.3: Interlamellar spacing of eutectoid pearlite as a function of the cooling conditions.

Cooling rate (K/s)	Transformation range (K)	Temperature at 50% transformation	Interlamellar spacing, (Å)
35	878 – 833	560	680
29	903 – 865	600	890
18.5	935 – 900	632	1140
10	948 – 923	637	1150
5.5	958 – 940	662	1660
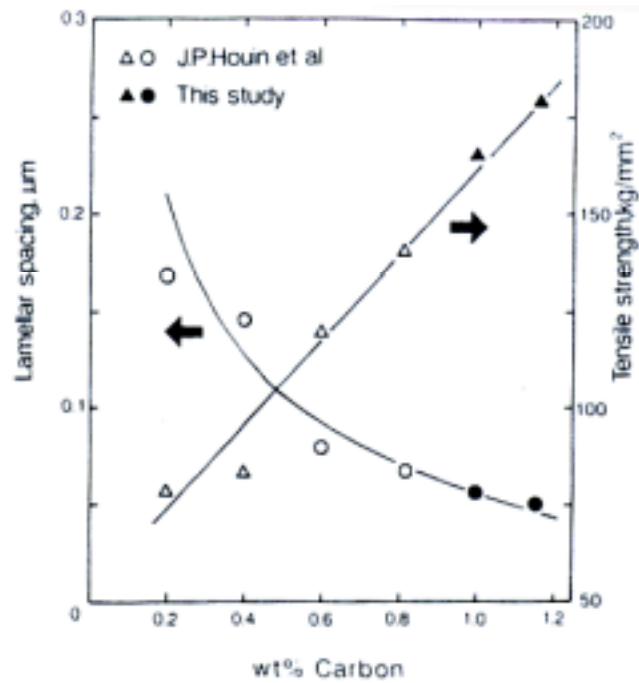
Figure 2.15 - Effect of carbon content on the lamellar spacing and the tensile strength of a fully pearlitic microstructure.

2.5.2 The Influence of Silicon on the Suppression of the Cementite in Hypereutectoid Steels

Heckel and Paxton[7] showed the influence of the silicon on the suppression of the cementite. Two steels with the chemical composition described below were used:

Table 2.4: Chemical composition of the steels used in the Heckel and Paxton study.

Steel	wt%C	wt%Mn	wt%Si
C	1.20	0.91	0.23
F	1.16	0.001	0.001

The difference between the thickness of cementite films in steels C and F is shown in Figure 2.16. This difference can be attributed to the silicon content. Silicon rejection at the advancing interface would cause a continually increased build-up here because of its low diffusivity. This leads to a retardation in growth by a combination of the necessity of silicon removal before cementite can form and its effect on increasing the activity of carbon in austenite, thus reducing, locally, the carbon activity gradient.[7]

Ikuo Ochiai et al., [20] Donald R. Lesuer et al., [5] and K. Han et al.,[27] have also reported that Si can be used in order to suppress the formation of cementite.

The cementite unit cell dimensions were not changed when silicon was introduced into iron-carbon alloys. It is concluded that the solubility of silicon in the carbide phase is negligible.[12,22]

The presence of silicon decreases the relative stability of cementite.[22] Smith[13] determined the influence of silicon on activity coefficients of carbon in both ferrite and austenite,

in equilibrium with graphite at 1273K. He found that silicon significantly increases the activity coefficient of carbon in both ferrite and austenite; the addition of silicon accordingly decreases the solubility of carbon in ferrite with respect to cementite.
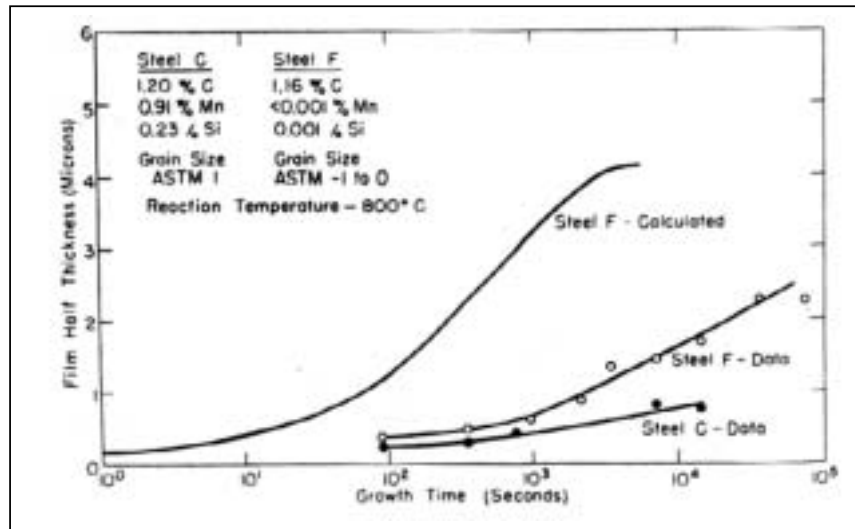
Figure 2.16 - The data for both steels C and F reacted at 800°C are shown for comparison. Calculated half thicknesses of cementite films in steel F (ASTM-1 to 0) reacted at 800°C.

Silicon has negligible solubility in cementite; hence, it retards the cementite precipitation[22] and inhibits the cementite growth.[27] An extra addition of Si also prevents the decrease in tensile strength during the galvanizing process.[3] It is also known that Si helps the formation of proeutectoid ferrite which reduces the drawability since cracks initiate at ferrite/pearlite boundaries, and they can cause delamination.[18]

Kaiso et al.[3] have made a further nano-order microstructure observation by transmission electron microscopy (TEM) making the effects of Si clearer. When the steel wire needs to pass through a galvanizing process, the temperature reaches 673K or higher, so the lamellar cementite

32

in the steel wire is converted into nano-size particles. As the process proceeds, the particles grow

coarser and the tensile strength as well as ductility, deteriorates, as shown in Figure 2.17. Silicon,

which is derived from lamellar cementite, is enriched on the lamellar cementite surfaces and

prevents the nano-particles from coarsening, thus preventing the decrease in tensile strength and

ductility.
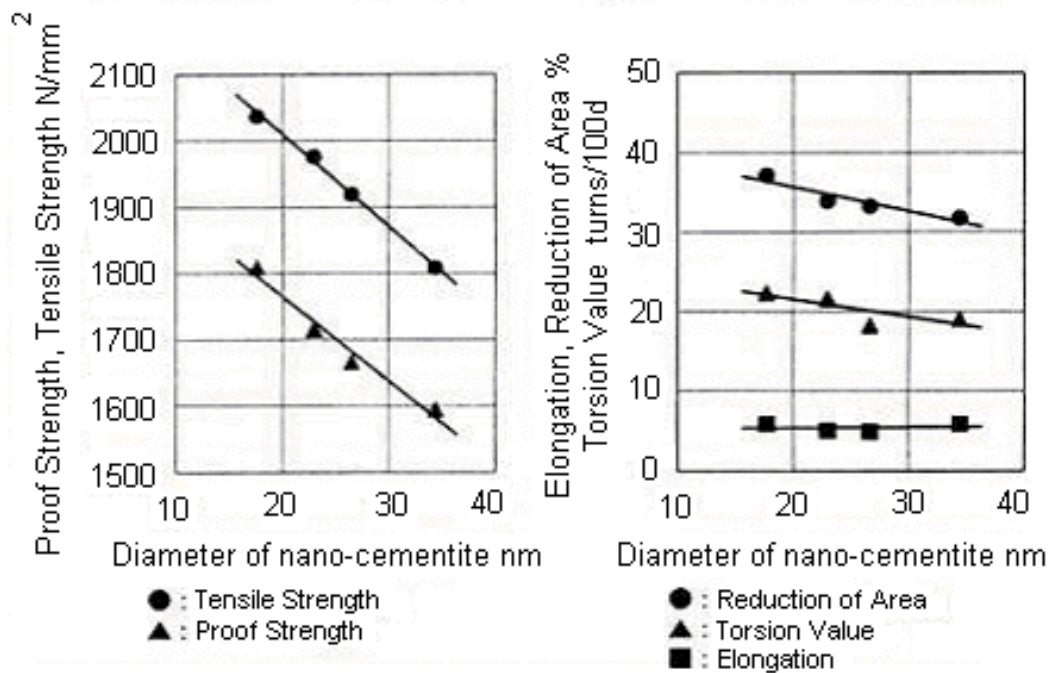
Figure 2.17 - Relation between mechanical properties of wires and the diameter of nano-cementite.

Kaiso et al.[3] used four types of steel to study the influence of the silicon on the tensile

strength and cementite formation after the galvanizing process. The steels used are presented in

Table 2.5: Chemical composition of the steels used to reach a tensile strength of the 2000N/mm^2.

Steel	wt%C	wt%Si	wt%Mn	wt%P	wt%S	wt%Cr
A	0.87	1.21	0.73	0.006	0.004	-
B	0.92	1.25	0.50	0.005	0.001	0.2
C	0.92	1.25	0.50	0.005	0.001	0.2
D	0.95	1.44	0.51	0.007	0.006	-

They used two steels to compare to those mentioned above. The first one is referred to as 1600N/mm^2 and the second one as 1800N/mm^2. Their compositions are described below.

Table 2.6: Compositions of the base steels.

Steel grade	wt%C	wt%Si	wt%Mn
1600 N/mm^2 grade	0.77	0.25	0.75
1800 N/mm^2 grade	0.82	0.90	0.75

The manufacturing process for galvanized wire is described below:

```
┌─────────────────────────────────────┐
│         Hot Rolled Wire rod         │
└─────────────────────────────────────┘
                  │
                  ▼
┌─────────────────────────────────────┐
│             Patenting               │
└─────────────────────────────────────┘
                  │
                  ▼
┌─────────────────────────────────────┐
│  Pickling and Zinc-phosphate Coating │
└─────────────────────────────────────┘
                  │
                  ▼
┌─────────────────────────────────────┐
│           Cold Drawing              │
│     (with Direct Cooling System)    │
└─────────────────────────────────────┘
                  │
                  ▼
┌─────────────────────────────────────┐
│           Straightening             │
└─────────────────────────────────────┘
                  │
                  ▼
┌─────────────────────────────────────┐
│          Zinc-galvanizing           │
└─────────────────────────────────────┘
```
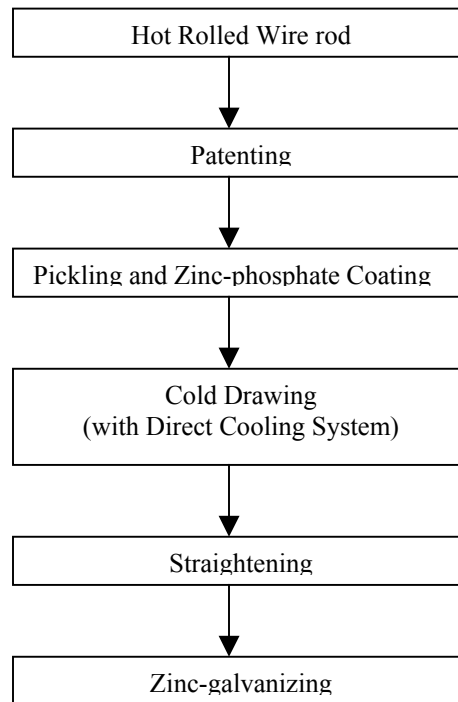
Figure 2.18 - Manufacturing process for galvanized wire.

As compared with the 1600N/mm^2-grade galvanized steel wire, the 1800N/mm^2-grade wire, containing an increased amount of Si, has finer cementite particles. The 2000N/mm^2-grade wire containing Cr and an increased amount of Si has even finer cementite particles. The addition of Cr and Si improves the tensile strength of galvanized steel wire by preventing the coarsening of nano-cementite particles.[3]

In addition to this property of the silicon in suppressing the formation of the proeutectoid cementite, it strengthens the wire because of the fact that its atomic radius is smaller than that of the iron and has a significant solid solution strengthening property in the ferrite phase.[28,29] C. E. Lacy and M. Gensamer [30] reported that 1 wt%Si has the effect of increasing tensile strength by 12.1kgf/mm^2.

2.5.3 The Influence of Manganese on the Suppression of the Cementite in Hypereutectoid Steels

Manganese would probably have little effect on growth kinetics of the cementite, because of the complete miscibility of Fe_3C and Mn_3C.[7,22] On the other hand, manganese reduces the proeutectoid ferrite volume fraction and the transformation temperature by increasing hardenability.[18]

The influence of manganese on the activity coefficient of carbon in ferrite has not been determined. It is known, however, that manganese causes a decrease in the activity coefficient of carbon in austenite with respect to graphite. [22]

Manganese distributes preferentially to cementite and lowers the temperature at which cementite begins to form.[22] Since manganese is soluble in both ferrite and cementite, there is no necessity for manganese diffusion. The presence of manganese does, however, make cementite more stable, and increases the driving force for its precipitation.[22]

2.5.4 The Influence of Phosphorus on the Suppression of the Cementite in Hypereutectoid Steels

There are two different opinions on the influence of phosphorus on the precipitation of cementite. The first one, by T. Ando and G. Krauss, is that phosphorus, in the 52100 steel grade, segregates to the austenite grain boundaries during the process of austenitization, thereby accelerating the formation of the cementite on the austenite grain boundaries.[31] The second one, by S. K. Ray, S. Mishra and O. N. Mohanty, based on work carried out in low carbon steel, is that phosphorus delays or inhibits the formation of Fe_3C precipitates with considerable effectiveness. [32,33] These authors reported a sharp increase in the solubility of carbon in ferrite caused by small additions of phosphorus. Such a sharp increase in the solubility can indicate a remarkable decrease in the activity of carbon, with respect to carbide formation, in the presence of phosphorus. This can lead to a retardation of cementite precipitation.

Also as pointed out by Leslie et al.,[22] if an alloying element is essentially insoluble in the carbide it can have a large effect on its growth. Hence, phosphorus, like silicon[7,12] or aluminum,[22] is also expected to inhibit carbide growth.[33] Moreover, being a surface-active element, phosphorus is likely to segregate at the carbide-ferrite interface, thereby restricting growth.[33]

2.5.5 The Influence of Copper on the Suppression of the Cementite in Hypereutectoid Steels

In addition to its significance as a sintering aid in powder metallurgy and as an impurity in recycled steel, copper is sometimes chosen as an alloying element because it does not form stable carbides, and it has very little solubility in cementite.[34,35] Thus, there is a strong thermodynamic tendency for it to partition away from cementite. Wasynczuk et al., used Fe-C and Fe-C-Cu

alloys in order to evaluate the effect of copper on the suppression of the cemenite by comparing the isothermal transformation kinetics and microstructure.[34] The TTT diagram generated for the Fe-1.43wt%C and Fe-1.49wt%C-4.90wt%Cu alloys is shown in Figure 2.19. It shows that copper significantly delayed the initiation of the pearlite transformation. The proeutectoid cementite transformation start curves for the Fe-1.43wt%C and Fe-1.49wt%C-4.90wt%Cu alloys were found to be the same.
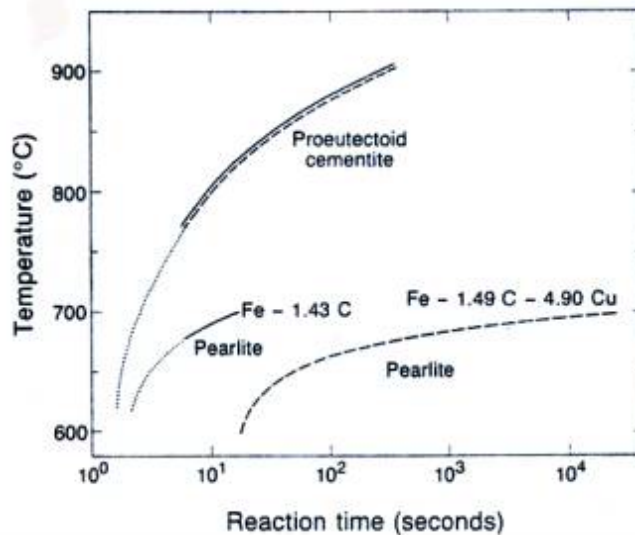
Figure 2.19 - TTT diagram for Fe-1.43wt%C and Fe-1.49wt%C-4.90wt%Cu[34]

The thickness of the grain boundary films of proeutectoid cementite was the same for both Fe-1.43wt%C and Fe-1.49wt%C-4.90wt%Cu, for a transformation temperature of 1023K, for one minute.

No retained austenite was observed in these microstructures, which is surprising in view of their high carbon content.[34]

However, Wasynczuk et al., concluded that copper does not have a large influence on the kinetics of proeutectoid cementite precipitation.[34]

2.5.6 The Influence of Aluminum on the Suppression of the Cementite in Hypereutectoid Steels

The addition of aluminum inhibits the formation of a hypereutectoid carbide network and stabilizes the ferrite phase. The addition of 1.6wt%Al raises the A_1 transformation temperature from 1000K to approximately 1053K.[10] Figure 2.20 shows an approximation of the Fe-C phase diagram for alloys containing 1.6wt%Al, 1.5wt%Cr, and 0.5wt%Mn.
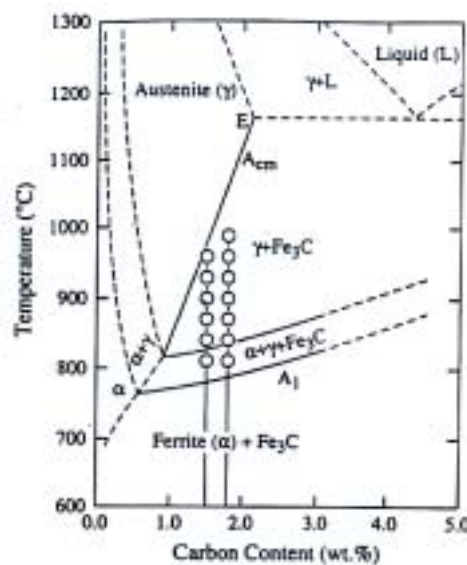
Figure 2.20 - An approximate phase diagram of the Fe-C system for alloys containing 1.6wt%Al, 1.5wt%Cr, and 0.5wt%Mn. Open circles represent austenitizing temperature select in this study.

Aluminum increases the cementite initiation temperature for a given aging time, and greatly increases the time required for cementite formation at a given temperature.[22] It has no

39

significant solubility in cementite, decreases the relative stability of cementite, and retards the cementite precipitation.[22] In the Fe-Al-C alloys, cementite forms at temperatures too low to permit extensive diffusion of aluminum.

Therefore, aluminum additions to low-carbon iron inhibit the precipitation of cementite and increase the time and temperature required for cementite to replace the transition carbide.[22] However, in hypereutectoid steel, addition of aluminum is prohibited since it forms hard inclusions.[1,2,36]

2.5.7 The Influence of Chromium on the Suppression of the Cementite in Hypereutectoid Steels

The effect of Cr on the suppression of the proeutectoid cementite is not been completely understood, however, it is known that the addition of Cr inhibits the graphitization and stabilizes the carbides, making coarsening more difficult.[10] M. Kaiso et al.,[3] also stated that when Cr and Si are added to the steel, the improvement of the tensile strength is due to the prevention of the coarsening of the nano-cementite particles.

2.5.8 The Influence of Boron on the Suppression of the Cementite in Hypereutectoid Steels

Since very small amounts of boron have a strong effect on the steel properties, it is a very important microalloying element in steels. Its effect has been studied mainly in low-carbon steels, in which it is well known that small amounts retard the nucleation of the ferrite and bainite; hence it increases the hardenability. The increase in the hardenability is true for steels containing up to 0.4wt%C.

Boron has a high solubility in Fe_3C and can be substituted for carbon in percentages close to 80% (atomic percent) to form borocementite.[37] Figure 2.21 shows the influence of the addition of boron on the lattice parameter of the cementite orthorhombic cell. The b lattice parameter increases drastically with the addition of boron, whereas the a, and c parameters decrease consistently. As a result of the huge increase of the b parameter, the volume of the unit cell increases as boron is substituted for carbon.
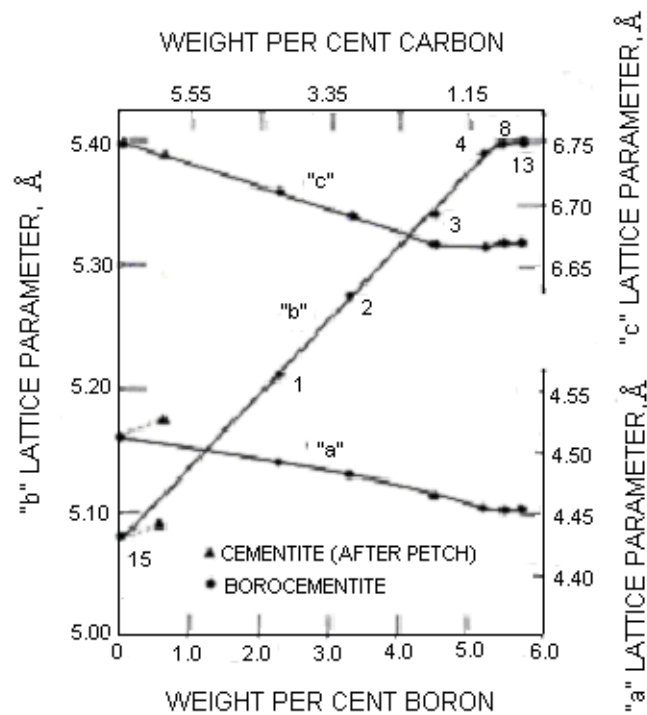
Figure 2.21 - Lattice parameter of $Fe_3(C,B)$ as a function of boron content of $Fe_3(C,B)$[37]

Furthermore, the carbide dissolution takes more time in the case of boron steel,[38] since cementite in boron steel would be more stable than that of plain carbon steel. Boron stabilizes

the hypothetical phase, $Fe_{23}C$. It is pointed out by L. Lanier et al.,[38] that massive precipitation of $Fe_{23}(B, C)_6$ takes place along austenitic grain boundaries when samples are air cooled from high austenitizing temperatures.

2.5.9 The Influence of Vanadium on the Suppression of the Cementite in Hypereutectoid Steels

Despite the fact that vanadium is known as an element that decreases the eutectoid carbon content, it promotes the formation of what is called "free ferrite".[39] The opposite effect might have been expected. Vanadium also increases the formation of the grain boundary ferrite at the eutectoid composition range.[27]

Experiments carried out by K. Han et al.,[39] showed that the thickness of proeutectoid cementite decreases when vanadium is added to hypereutectoid steels. The thickness of the proeutectoid cementite decreases so much that it is not even detectable by means of optical microscopy. However, SEM analyses showed that grain boundary cementite did exist in these steels. The cementite, however, seemed to be much less continuous than in plain carbon steels.[27,39,40] These results indicate that vanadium additions were promoting the nucleation of independent carbide particles on the grain boundary. Such a distribution of cementite should be less deleterious to mechanical properties than the continuous grain boundary cementite network.

The addition of vanadium was also found to decrease the austenitic grain size.[27,39] Therefore, the grain boundary cementite has more austenite grain boundary area to occupy per unit volume of the steel. This can lead to a decrease in the number of cementite particles forming on the boundary and also make them thinner.[27] It is not necessarily true that the thinner the grain boundary cementite, the lower the volume fraction of proeutectoid cementite in vanadium steels. Instead, the grain boundary cementite is less continuous. This discontinuity of the

cementite reduces the tendency for intergranular cracking in vanadium steels.[39] The hypereutectoid vanadium-bearing steels, therefore, are expected to have better mechanical properties because of the different grain boundary cementite morphology.[27]

The thickness of the proeutectoid cementite, formed in steels containing vanadium, is much smaller than that observed in plain hypereutectoid steels, as mentioned above. Therefore, incorrect conclusions can be made if measurements are performed using only light microscopy. Thus, the use of the SEM is recommended to really determine whether the steel is completely free of proeutectoid cementite.[27]

In order to really suppress the formation of the proeutectoid cementite and strengthen the pearlite on hypereutectoid steels, vanadium and silicon should be used together;[40] thus making it possible to draw a ultrahigh-carbon pearlite into high strength wire.

2.5.10 Summary of the effect of the elements on the suppression of the cementite

Table 2.7, which summarizes the effect of some elements on the suppression of the cementite, it provides a meaning of reviewing the effect of each element on the suppression of cementite.

Table 2.7: Summary of the effect of some elements on the suppression of the cementite.

Element	Effect on Fe₃C	Range	Comments	References
Co	Suppress	0.2 to 1.3wt%C		Y. Kanetsuk et al. ISIJ 1991.[4]
Si	Suppress	0.15 to 1.2wt%C		R. W. Heckel and H. W Paxton. Trans. of Metall. Society of AIME. 1960.[7] / M. Kaiso et al. Wire Journal Inter. 2002.[3]
Cu	No effect	wt%C > 1.3		J. A. Wasynczuk et al. Metall. Trans. A. 1986.[34]
Cr	Suppress		Even though some authors have supported this idea, no data were found by the writer.	E. M. Taleff et al. Metall. and Materials Trans. A. 1996.[10]
Mn	No effect			R. W. Heckel and H. W Paxton. Trans. of Metall. Society of AIME. 1960.[7] / W. C Leslie and G. C. Rauch Metall. Trans. A. 1978.[22]
Al	Suppress	Low carbon steel		W. C Leslie and G. C. Rauch Metall. Trans. A. 1978.[22] / E. M. Taleff et al. Metall. and Materials Trans. A. 1996.[10]
P	Accelerate	1.00 wt%C	There is a disagreement among authors relating to the effect of P on the suppression of Fe₃C.	T. Ando and G. Krauss. Metall. Trans. A.1981.[31]
	Suppress	Low carbon		S. K. Ray et al. Scripta Metall. 1982.[33]
B	No effect	High Carbon		Nicholson Journal of Metals 1957.[37] / L. Lanier et al. Mikrochim. Acta 1994.[38]
V	It decreases the thickness and fragments the cementite. It inhibits cementite network formation.	Hypereutectoid steels.	It does not necessarily decrease the proeutectoid cementite volume fraction, but it fragments it because vanadium acts as the driving force for carbide formation.	K. Han et. al. Materials Science & Engineering A. 1995.[39]

2.6 THE INFLUENCE OF THE COOLING RATE ON THE SUPPRESSION OF THE CEMENTITE

Ikuo Ochiai et al., carried out a study using vacuum-melted 0.2wt%Si – 0.5wt%Mn steels having different C contents. They investigated the effect of carbon content and cooling rate on the precipitation of the proeutectoid cementite onto the austenite grain boundaries. An alkaline sodium picrate etching solution (JIS G0551) was employed to analyze the proeutectoid cementite.[20]

The experimental results are shown in Figure 2.22. In general, the cooling rate of 5.5mm wire rod in the cooling conveyor is 10 to 15K/s at the center of the wire rod. From Figure 2.22, it can be concluded that no proeutectoid cementite is precipitated in a cooling conveyor, as long as the C content of steel is less than approximately 1.10 wt percent. This means that even a hypereutectoid wire rod steel can be drawn without lead patenting.[20] This graph also shows that higher cooling rates tend to suppress the formation of a network even for steels containing more than 1.10%wt of carbon. In addition, as the carbon concentration in a hypereutectoid steel is increased, faster cooling rates are required to obtain pearlitic structures without a network.

Yutaka Kanetsuk et al.,[4] plotted the CCT diagrams for steels A and B with the composition described in Table 2.8.
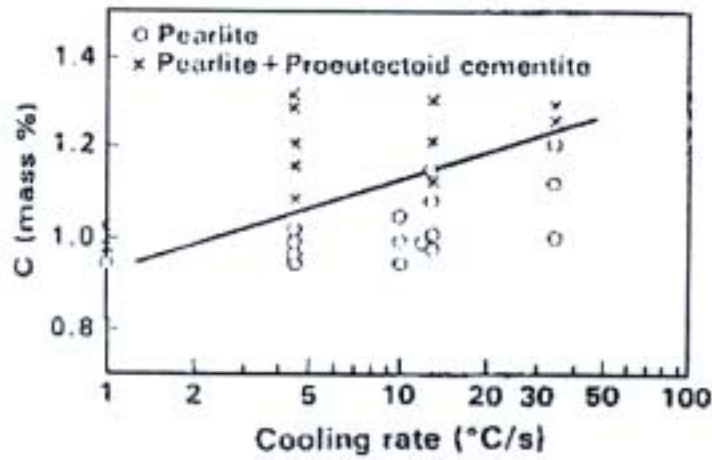
Figure 2.22 - Effects of C content and cooling rate on proeutectoid cementite precipitation in 0.2wt%Si – 0.5wt%Mn steel[20]

Table 2.8: Chemical composition of steels A an B used in the Yutaka Kanetsuk et al. study.

Steel	wt%C	wt%Si	wt%Mn	wt%P	wt%S	wt%Cu	wt%Co
A	1.01	0.20	0.48	0.004	0.002	<0.01	0.49
B	1.15	0.23	0.52	0.008	0.003	<0.01	0.98

Figure 2.23 shows the CCT curves for steels A and B, respectively. The A_{cm} and M_S temperatures were changed due to the difference in carbon content. It is well known that the hardenability of low plain carbon steel is lower than that of eutectoid steel due to the proeutectoid reaction. However, the critical cooling rates for steels A and B are very similar to that of the of eutectoid steel.[4]

46

Figure 2.24 shows four microstructures for different cooling rates used to cool the steel A. Figures 2.24a and 2.24b show the absence of apparent proeutectoid cementite precipitation, but Figures 2.24c and 2.24d show boundary cementite precipitation. Hence, the reduced nucleation and growth rates of the proeutectoid cementite reaction could be attributed to the effect of the cooling rate.[4]
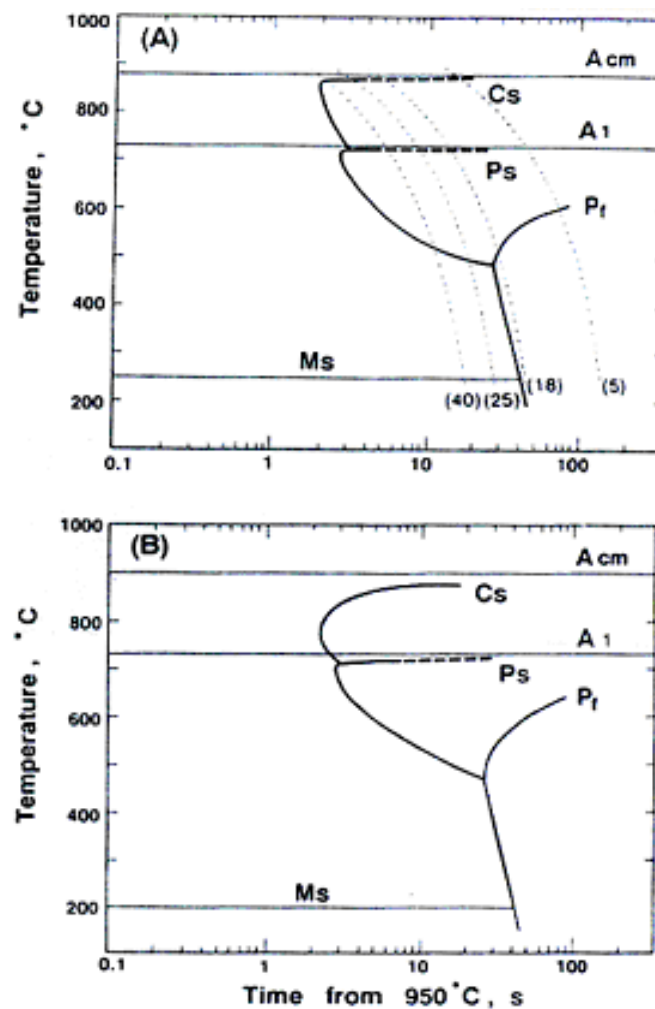
Figure 2.23 - CCT diagram of steels A and B. (Austenitization: 950°C or 1223K, 10 min).
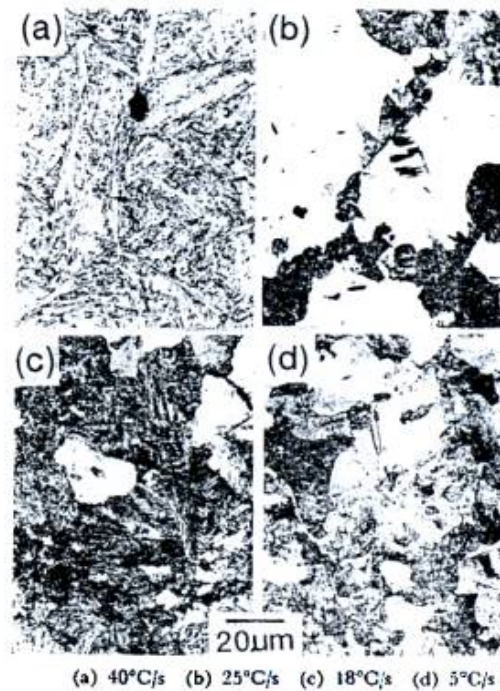
Figure 2.24 - Optical micrographs showing the microstructure of steel A observed at various cooling rates.

2.7 SEGREGATION TO GRAIN BOUNDARIES

Net migration of solute atoms to grain boundaries during thermal processing of metals has been called grain boundary segregation. In many systems, the local grain boundary structural and composition determines the grain boundary strength and the propensity for intergranular fracture. It is, therefore, necessary to understand the process of grain boundary segregation in order to understand the causes of intergranular fracture. Grain boundary segregation involves diffusion of atomic species to the grain boundary and, therefore, it is a thermally activated process.[41]

The association between grain boundary weakness and altered composition was deduced from careful experiments on pure metals containing known elements. One example is iron with oxygen, phosphorus, antimony, tin and sulphur. All of these additives increase the ductile to brittle transition temperature and promote failure by grain boundary decohesion. Figure 2.25 shows this phenomenon. In Figure 2.25, the parameter known as grain boundary enrichment factor is plotted as a function of the inverse of the species' solid solubility at the temperature of the measurement. This shows two tendencies. The first tendency, to enrich the grain boundaries, varies inversely with the solid solubility. The second is that systems shown to have been studied so far which have a high enrichment factor are also systems that have been reported to be intergranularly weak (some exceptions are Fe-B, Fe-C and Ni-B).[42]

2.7.1 Quantitative Grain Boundary Composition

For certain situations, qualitative evidence of grain boundary enrichment is sufficient. However, a more complete in-depth study of segregation, especially if segregation mechanisms are to be considered, requires a quantitative analysis of grain boundary composition. This is particularly important if the temperature dependence of segregation is required in order to determine the temperature range of maximum or minimum embrittlement.[42]
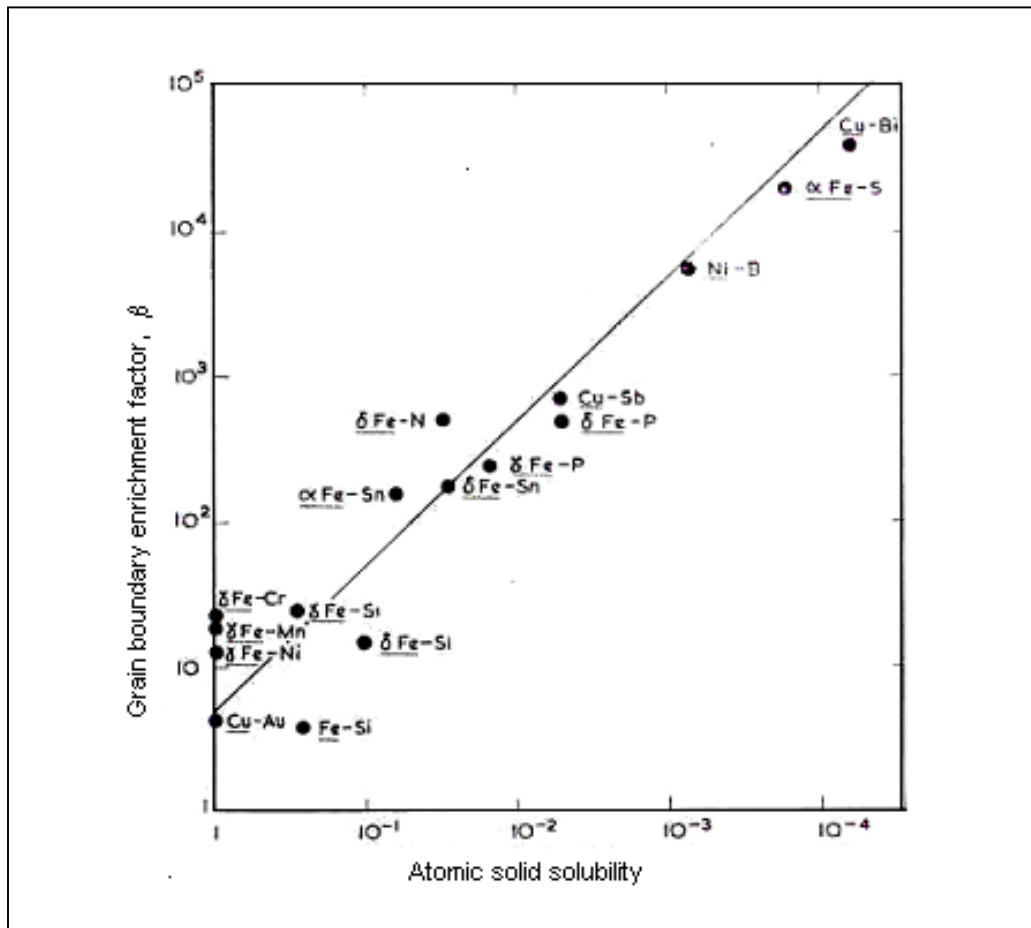
Figure 2.25 - Relation between the grain boundary enrichment factor, β, and the inverse of solid solution solubility. The parent element is underlined in each pair.

2.7.2 Solute Concentration at Grain Boundaries – Equilibrium Segregation

The idea that solute elements in equilibrium sometimes concentrate at grain boundaries while remaining in solution has been used from time to time to explain particular phenomena. To distinguish the segregation in question from the segregation to grain boundaries occurring during freezing, which is a non-equilibrium phenomenon, it is called "equilibrium segregation".[43]

50

2.7.3 Factors Contributing to Equilibrium Segregation

The C-Curve relates the rate of crystal growth and the rate of homogeneous nucleation. For small undercooling, the rate of crystal growth is large, but the rate of nucleation is small. As the undercooling increases, the rate of homogeneous nucleation also increases. On the other hand, the diffusion of atoms gets more sluggish. Therefore, there is a certain undercooling at which the rate of reaction reaches its maximum and the equilibrium condition can be reached faster.

The thermodynamic approach to the problem of ascertaining the concentration of solute at grain boundaries follows the lines laid down by Gibbs. He showed that, as a rule, solute elements that decrease the surface tension should concentrate at the surface, and those that increase the surface tension should avoid the surface.[43]

More progress in order to elucidate the reason for equilibrium segregation can be made by considering the lattice distortion energy around solute atoms. A solute atom larger than the site it occupies in the solvent lattice should fit more easily in a site that is already expanded than in a site that is compressed. In other words, it should cause less extra lattice distortion. On the other hand, a solute atom smaller than the site it occupies in the solvent lattice should fit more easily in a site, which is already compressed than in a site that is expanded. Hence, in a crystal with a distorted lattice in which the volume of the spaces to be occupied by solute atoms varies from place to place, a higher concentration should build up at certain regions than at others. Therefore, at grain boundaries, some atoms have more space around them and others have less space around them than would be normal for the undistorted lattice. Large solute atoms will tend to replace the former and small ones the latter. Therefore, we expect equilibrium segregation to grain boundaries. Another region where segregation has important consequences is that around a dislocation.

51

The equation below gives the concentration at a grain boundary (C_d) as a function of the grain interior concentration (C), activation energy for diffusion (Q), gas constant (R), and temperature (T), equation 2.6.

$$C_d \quad = \quad \frac{Ce^{Q/RT}}{1+Ce^{Q/RT}} \tag{2.6}$$

where $C \ll 1$

Figures 2.26 and 2.27[42] show that the grain boundary concentration depends, sensitively, on the magnitude of Q. Figures 2.26 and 2.27 also show that the grain boundary concentration decreases at higher temperatures. It is, therefore, with highly distorting solutes that the most marked effects can occur in practice. With these, a large grain boundary concentration may be produced by a very small grain interior concentration, so that highly distorting solute elements present only in traces might have important practical consequences.
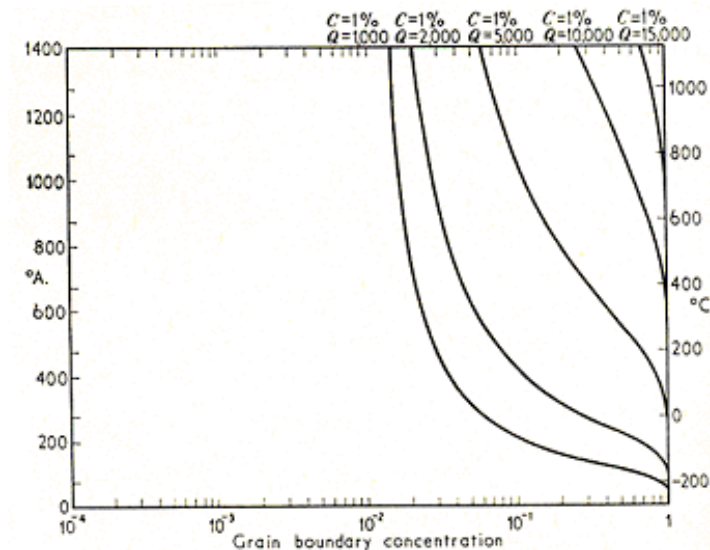
Figure 2.26 - Relation between grain boundary concentration and temperature. C = grain interior concentration in atomic per cent[42]

52
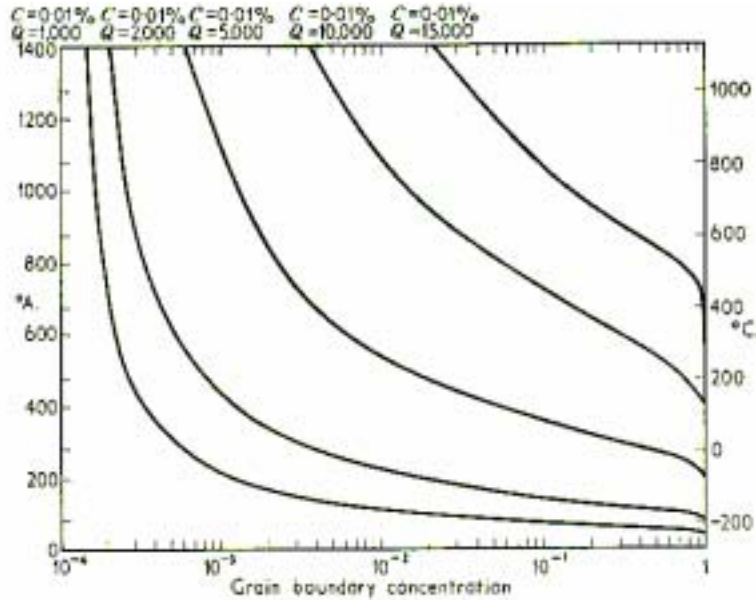
Figure 2.27 - Relation between grain boundary concentration and temperature. C = grain interior concentration in atomic per cent[42]

In general, to avoid high grain boundary concentration, it is necessary to quench from a temperature high enough to disperse the solute to one low enough to prevent diffusion. A high grain boundary concentration will subsequently increase if the material is heated to a temperature at which diffusion can occur. This will then be dispersed again by raising the temperature sufficiently. Concentration and dispersal can be repeated indefinitely.

Even if all boundaries are identical, a range of values of Q presumably occurs in practice since the volumes associated with individual grain boundary atoms must vary between upper and lower limits. This will have the effect of widening the lines in Figures 2.26 and 2.27 into bands. Segregation will be more pronounced in some boundaries than in others and may be uneven along individual boundaries.

No effect of lattice type exists for substitutional solutes, but it does exist for interstitial solutes. This is because the interstitial holes are larger in the face-centered cubic and hexagonal closed-packed lattices than in body-centered cubic lattice. The diameters of the largest spheres that fit into the interstitial positions, expressed as a fraction of the diameter of the lattice atoms, are 0.414 of FCC and HCP, and 0.155 for BCC lattices. Therefore, interstitial atoms produce more distortion in BCC than in FCC and HCP lattices, and should segregate strongly in the former.

Other properties of solute atoms besides size might affect the tendency to segregate to distorted regions. The electron arrangement is one of these.

2.7.4 Types of Segregation Species

According to published accounts of segregation phenomena, there is practically no limit to the type of segregation element. Generally, in the case of the iron, in conformity with the relation in Figure 2.25, gaseous species such as oxygen, sulphur and nitrogen are the most surface active in decreasing order. The segregation tendency of carbon is not clear, but it is believed to enter into competitive interactions with other elements, for example with tin and phosphorus in iron.[42]

In general, elements with low atomic numbers appear to be the most active. For example, the role of nickel, chromium, molybdenum and manganese in controlling segregation during the temper embrittlement of low carbon steels is a feature that is often alluded to by work in this field.[42]

The solutes present in the matrix (for example, carbon) have a tendency to segregate to the grain boundaries to decrease their free energy. However, the species does not have the same tendency to segregate to every single grain boundary.[44] Generally, the boundary energy

increases drastically with increasing boundary angle in the low grain boundary region until 15~20°, and saturates after this value except in the case of the coincidence site lattice (CSL) boundary.[45] A. F. Gourgues[44] divided the grain boundary misorientation angle ,$\Delta\theta$, (the minimum rotation angle between the two grains) as low angle boundaries if $\Delta\theta \leq 15°$ and as high angle boundaries if $\Delta\theta > 15°$. High angle boundaries are sensitive to diffusion and segregation phenomena.[44] Thus, the segregation of the elements to high angle misorientation boundaries is more probable compared to the segregation of the elements to low angle misorientation boundaries.

2.8 SUMMARY

The demand for higher strength steels has increased in order to reduce the amount of steel used in several applications, such as long-span bridges, rails, high-rise buildings, and automobiles. In the case of automobile components the steel tire cord, which is used to reinforce the structure of the automobile tires, was the main focus of this literature review. Among those strengthening mechanisms discussed previously, the most important one for this application is solid solution strengthening. The solid solution strengthening used in steel tire cord applications is reached when the carbon content of the bulk composition is increased. Currently, hypereutectoid steels are being tested as a substitute for steel tire cord with eutectoid composition (approximately 0.8wt%C). The advantage of the hypereutectoid steel is its higher strength but the disadvantage is its potential to fracture during the cold drawing process. The tendency to fracture depends primarily on the formation of the proeutectoid cementite which varies with the amount of carbon in solid solution that can segregate to certain grain boundaries. These grain boundaries are

believed to be those with high misorientation angle ($\Delta\theta > 15°$) due to the strong tendency of the solutes to segregate to these grain boundaries. At this time, the suppression of this proeutectoid cementite can be done in two very different ways: the first one is to increase the cooling rate, since the formation of the proeutectoid cementite is a diffusion process; the second one is the addition of some elements like Co and Si. These elements can suppress the formation of cementite because of their low solubility in the proeutectoid cementite. Mn, on the other hand, has no effect on suppression of the cementite since its solubility in the cementite is very high. The influence of the Cu in the suppression of the cementite is not confirmed. The idea of using the Cu is based on the fact that it shares common properties with Si and Co. However, it was tested in some alloys with more than 1.3wt%C, the limit of carbon with which Co can be efficient for suppressing the formation of the cementite. Unfortunately, further studies on the suppression of the cementite network by Cu in steels containing less carbon than 1.3wt% are necessary to determine its effectiveness.

3.0 STATEMENT OF OBJECTIVES

The primary objective of this work is to characterize the proeutectoid cementite network in a hypereutectoid steel with 0.92wt% of carbon, and determine its distribution along the transversal sections of different wire rod diameters.

The influence of the cooling rate on the suppression of this brittle phase is also a major objective of this work.

Upon understanding the formation of the proeutectoid cementite network and gaining knowledge of the effective cooling rate needed to suppress its formation, some industrial experiments will be conducted. The industrial experiments will be designed aiming the minimization of the proeutectoid cementite network in such a way that the wire rod can be drawn to wires.

4.0 EXPERIMENTAL PROCEDURES

4.1 SAMPLE PRODUCTION

The chemical composition to the studied material is given in Table 4.1.

Table 4.1: Chemical composition of the heat used in this research

wt%C	wt%Mn	wt%Si	wt%Cr
0.92	0.3	0.18	0.2

Billets of this heat were hot rolled to different diameters, i.e., 5.5, 7.0, 8.0, 9.0, 10.0, and 11.5mm. The cooling rate on the cooling conveyor was measured using a pyrometer during the rolling of each gage. Samples of these different diameters were collected and the proeutectoid cementite was analyzed.

4.2 MATERIAL PROCESSING

A heat of approximately 100t of liquid steel was produced in the BOF converter. For the purpose of fine chemical and temperature adjustments, the heat was passed through a ladle furnace. After that, it was solidified in a six-strand continuous casting machine to produce billets of 155mm square by 12m long. These billets were reheated in a walk beam furnace and then hot rolled to several different gages. The rods went through some water boxes aimed at the appropriate temperature to be air cooled on the cooling conveyor. Figure 4.1 shows the flow chart for this sequence of operations.
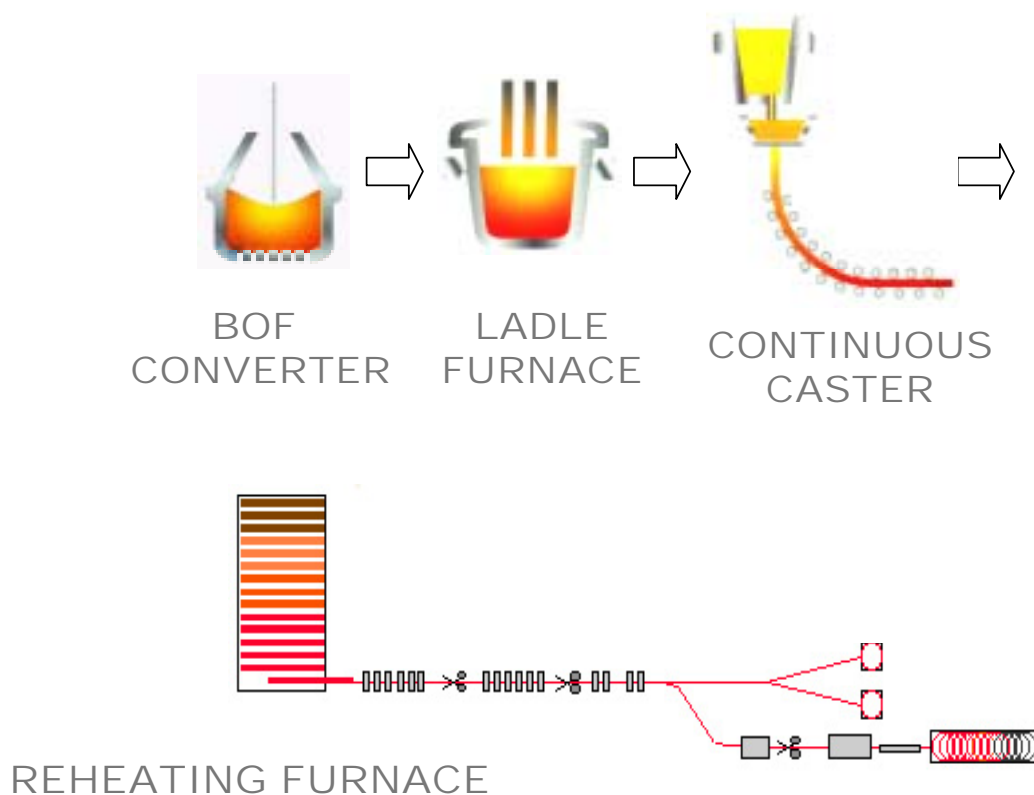
Figure 4.1 – Flow chart of the production line of Belgo at Monlevade's plant.

4.3 MICROSTRUCTURAL ANALYSIS

4.3.1 Optical Microscopy Analysis

Metallographic analyses of the received wire rods were performed by sectioning the samples transversely to the rolling direction, and mounting them in bakelite. The samples were rough polished by using 180, 240, 320, 400, and 600 grit grinding paper. The final polishing was done by using 1μm, and 0.05μm alumina powders, respectively. The etching was performed by immersing the samples in a picric acid solution containing 2g of picric acid and 25g of sodium, balanced with distilled water for 100ml, for 7 minutes at approximately 343K. The cementite looks dark while ferrite remains uncolored.

Optical micrographs were taken using a Sony digital camera attached to a Nikon Microscope. "Bioquant image analysis" software was utilized to save the images on the computer in jpg format.

4.3.2 Scanning Electron Microscopy (SEM)

Samples for SEM analyses were prepared in exactly the same way as the ones for optical microscopy analyses. Analyses were performed on a Philips XL 30 FEG SEM with an acceleration of 15kV, spot size 3, and usually by secondary electrons (SE) or back-scattered electrons (BSE) functions.

4.3.3 Electron Backscattered Diffraction Analyses (EBSD)

The EBSD was used to obtain and compare orientation maps between areas where the proeutectoid cementite network was present and where it was absent. The sample preparation was very similar to the one used for optical microscopy up to final polishing, after which the samples were further polished in a Vibromet 2 polishing machine for 7 hours using 0.05μm alumina. This final step achieved the deserved flat surface. The samples were then etched following the same procedure used in optical microscopy. In other to check whether the etching could be influencing the results, a 100μm thick foil was also polished up to 0.05 microns, etched to find the region with the proeutectoid cementite network and then a 3.0mm diameter disc from the region where the proeutectoid cementite network was located, was obtained. The disc was then polished using the ion miling with both guns tilted two degrees with respect to the upper surface.

For the EBSD examinations, the samples were tilted 80° and in focus at 18mm working distance. Parameters for the SEM were acceleration voltage of 15kV, spot size 5, and step size of 2μm. Tests using different magnifications were also used to ensure that the results were not a function of the parameters of the SEM.

4.4 DILATOMETRIC EXPERIMENTS

An Adamel-Lhomargy LK02 dilatometer was used in this research because of its computer controlled furnace with a completely enclosed sample chamber. The dilatometry samples were machined as cylinders of 2.0mm diameter by 12mm length. The sample temperature was monitored through a k-type thermocouple spot welded to the surface of the sample.

A pre-cycle was applied to every sample in order to have homogeneous samples. This pre-cycle was composed of a heating rate of the 10K/s from the room temperature up to 1193K and a cooling rate of the 10K/s up to room temperature. The samples were heated again with 10K/s from the room temperature up to 1193K and cooled with many different cooling rates to room temperature. They were also cooled in vacuum and in two different atmospheres: helium, and air. Figure 4.1 shows, schematically, how the process of homogenization and final tests were performed.
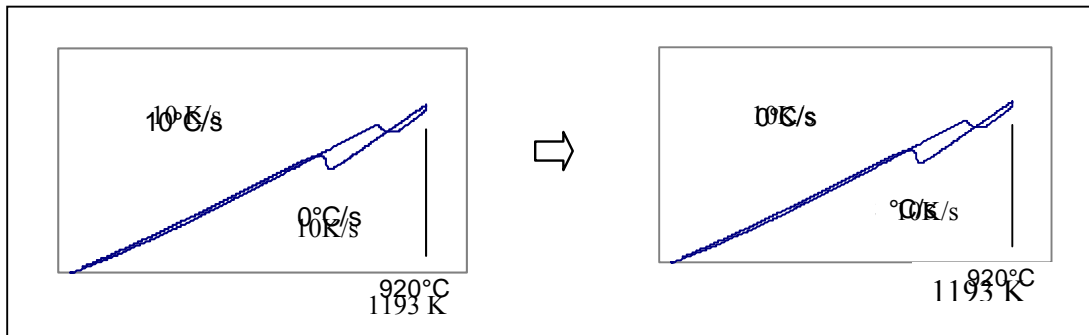
Figure 4.2 - Schematic representation of the dilatometric test.

The cooling rates and the atmosphere used to perform the dilatometry experiments are described in Table 4.2.

Table 4.2: Cooling rate and atmosphere used in the dilatometric tests

CR (K/s) atmosphere	1	2	3	6	9	12	15	18	21
Helium	■	■	■	■	■	■	■	■	■
Air	■	■	■	■	■	■	■		
Vacuum	■	■	■	■	■	■			

■ Cooling rate used for the corresponding atmosphere.

The sample for each test was then cut transversely to the length in order for one to analyze the proeutectoid cementite formed during each condition of cooling rate and atmosphere. Samples were prepared in exactly the same way as those for optical microscopy. In order to quantify the amount of cementite formed, the austenitic grain boundaries covered with proeutectoid cementite were counted individually.

4.5 INDUSTRIAL EXPERIMENTS

The industrial experiments were performed according to a statistical technique known as DOE (Design of Experiments) – Two-Level Factorial Design.

To perform a general factorial design, an investigator selects a fixed number of "levels" (or "versions") for each of a number of variables (factors) and then runs the experiments with all possible combinations. Two billets were rolled for each designed experiment. The first one was used to adjust the conditions of the test itself and the second one was used to measure the influence of each variable on the formation of proeutectoid cementite, tensile strength, and cooling rate.

The software Minitab was used to quantify the influence of each variable and level on the mentioned responses.

The proeutectoid cementite was analyzed in the same way as the one for optical microscopy. The tensile strength was calculated using the Wolper/Trebel-60 TUZ machine. Finally, the cooling rate was measured using a MINOLTA/LAND Cyclops 152 pyrometer during the rolling of each gage. Figure 4.3 shows the method used to calculate the cooling rate. The slope of the curve between the temperature and time prior to the austenite to pearlite transformation illustrates the cooling rate.
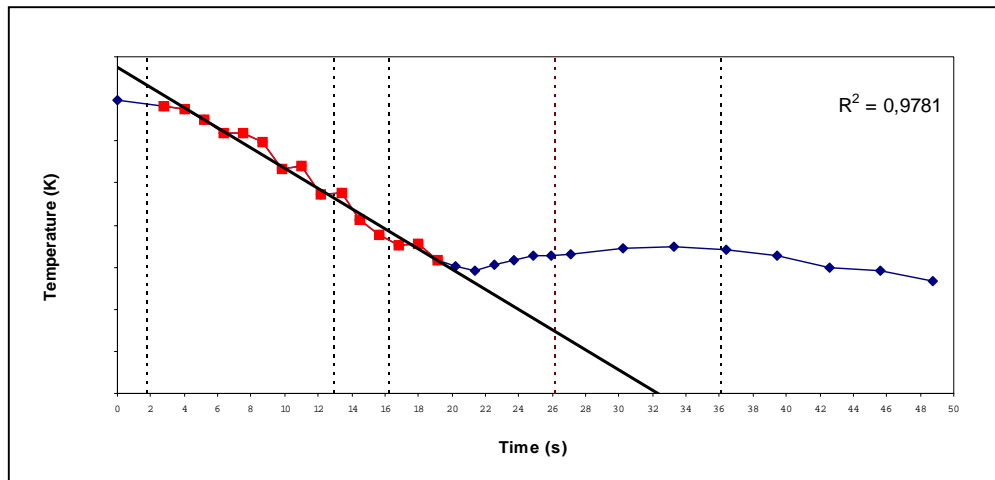
Figure 4.3 - Temperature versus time curve used to calculate the cooling rate on the cooling conveyor before the start of transformation, which is indicated by the deviation from the straight line, around 20 seconds.

5.0 RESULTS

5.1 CHARACTERIZATION OF THE PROEUTECTOID CEMENTITE NETWORK

The characterization of the proeutectoid cementite network in the studied material (Table 4.1) was done for different wire rod diameters. For small diameter samples (5.5, 7.0, and 8.0mm), proeutectoid cementite was observed only in the center of the samples but no network was observed. Figure 5.1 shows an optical microscopy of the proeutectoid cementite detected in a 5.5mm diameter sample.

50 μm
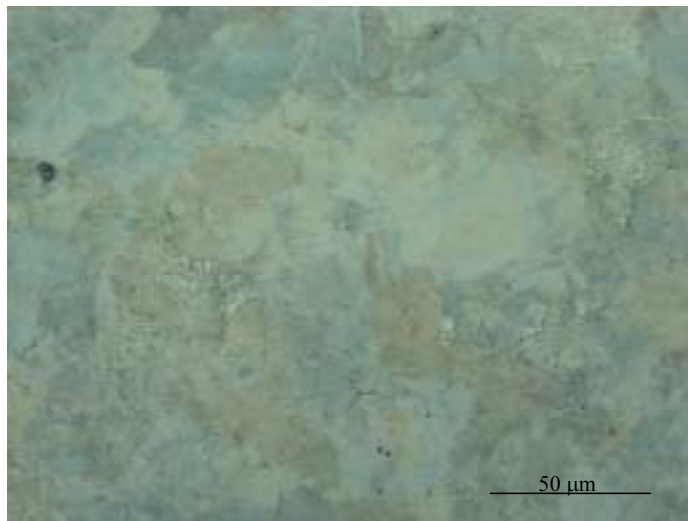
Figure 5.1 - Optical micrograph of a 5.5mm diameter sample free of proeutectoid cementite network. Magnification of 400X.

On the other hand, the characterization for large diameters (10.0, and 11.5mm) showed not only proeutectoid cementite network on the center of the samples but also another network on the edge. Here, proeutectoid cementite network is defined when there are more than five adjacent grains with all boundaries covered with Fe_3C. In Figures 5.2 a, and 5.2 b, proeutectoid cementite networks are detected in the center and close to the edge of a 10mm diameter sample.

50 μm
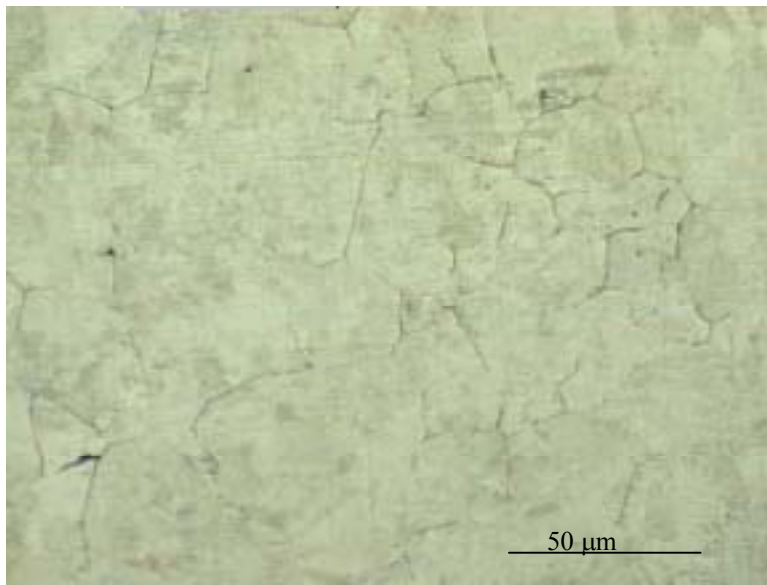
Figure 5.2.a - Optical micrograph of the proeutectoid cementite network in the center of a 10.0mm diameter sample. Magnification of 400X.
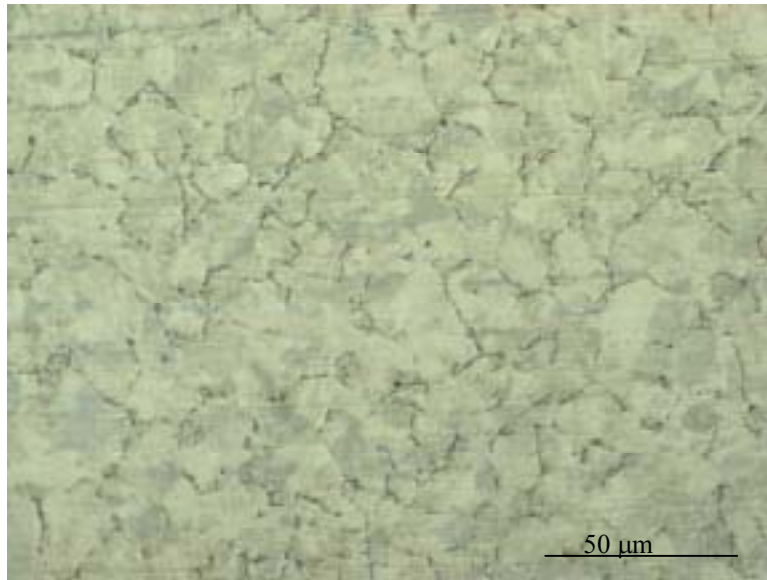
Figure 5.2.b - Optical micrograph of the proeutectoid cementite network on the edge of a 10.0mm diameter sample. Magnification of 400X.

The proeutectoid cementite networks present in a 10.0mm sample were also observed using the SEM. Figures 5.3 shows the proeutectoid cementite network observed at the surface of a 10.0mm sample.
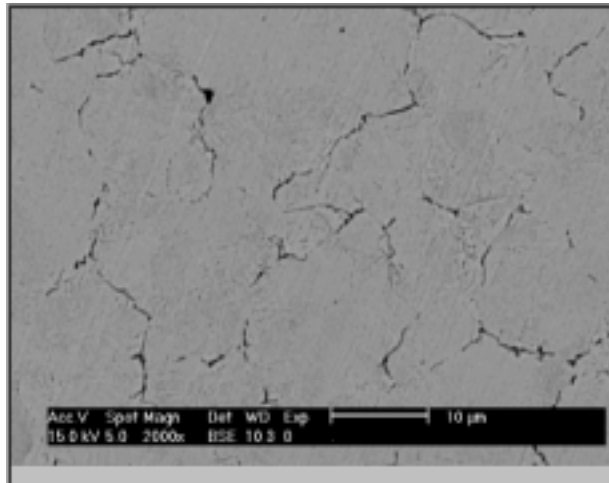
Figure 5.3 – SEM micrograph of the proeutectoid cementite network in the center of a 10.0mm diameter sample. Magnification of 400X.

5.2 ELECTRON BACKSCATTERED DIFFRACTION ANALYSES (EBSD)

In order to identify the relationship between the proeutectoid cementite network formation and the grain boundaries, EBSD analyses were performed on four regions of the transversal section of a 10.0mm diameter sample close to the edge, at some locations around the perimeter. Figure 5.4.1 shows a schematic of a misorientation map, which provides a qualitative view of the misorientation results. Here, grain boundaries showing low misorientation (5-15°) between two grains are represented in orange while grain boundaries in yellow represents high misorientation (>15°). Figure 5.4.2 shows the maps of the misorientation for the four analyzed regions of a 10.0mm diameter sample. From these maps, it is possible to verify that in the region of the proeutectoid cementite network, few grain boundaries are represented in orange (low misorientation, i.e. 5 to 15°). On the other hand, many more grain boundaries are represented

with orange at the regions out of the proeutectoid cementite network region. The proeutectoid cementite network region was the first analyzed one. The region where the proeutectoid cementite network close to the edge was observed was identified as 0°. The second, third, and fourth regions were called as 90°, 180°, and 270°, respectively.
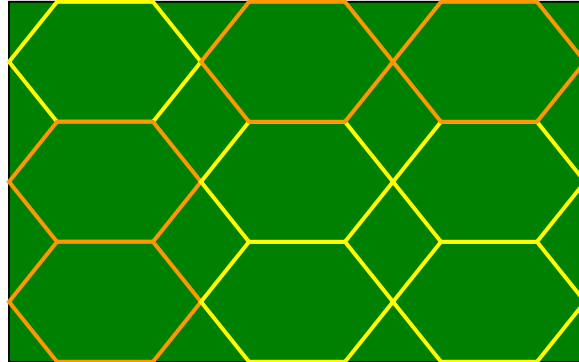
Figure 5.4.1 - Schematic representation of a misorientation map. It shows grain boundaries represented in orange that means low misorientation (5-15°) between the two grains and grain boundaries represented in yellow that means high misorientation (> 15°) between two grains.
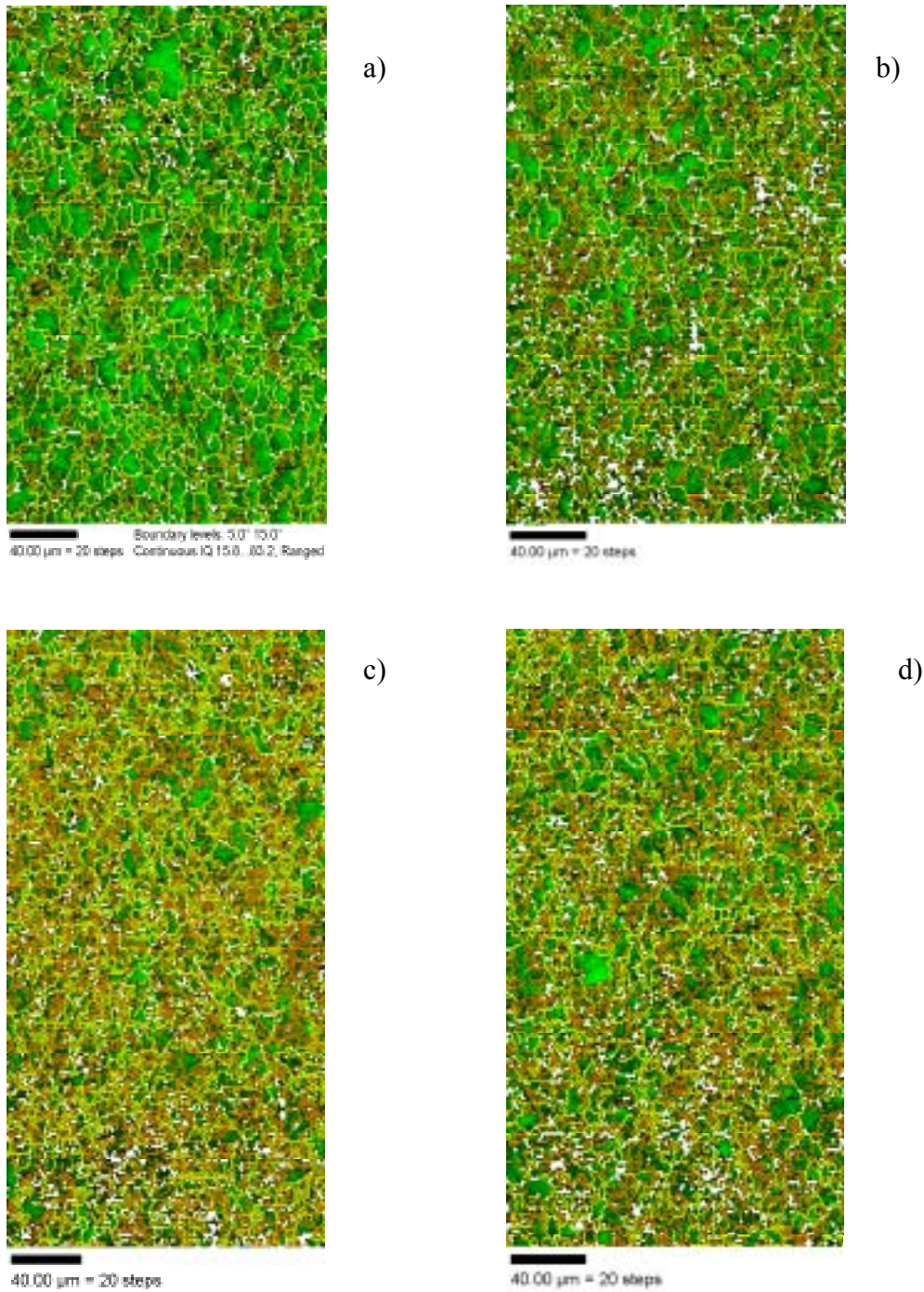
Figure 5.4.2 - Misorientation map of four regions of a 10.0mm diameter. The green color represents the ferrite of the pearlitic matrix, orange color the grain boundaries with misorientation between 5-15°, and the yellow color represents grain booundaries with misorientation greater than 15°. a) region of the proeutectoid cementite network. b) 90° from the network region. c) 180° from the network region. d) 270° from the network region.

Figure 5.5 shows a more quantitative result of the misorientation profile among grains for a 10.0mm diameter sample. The circle in the middle of the four graphs represents the transversal section of a 10.0mm diameter sample. The numbers inside of the circle represent regions where the analyses were performed. The region where the proeutectoid cementite network close to the edge was observed was identified as 0°. The second, third, and fourth regions were called as 90°, 180°, and 270°, respectively. Regions without the network show just one peak in the misorientation profile graph. This is a characteristic of the low misorientation among grains. The region covered with the network is characterized by a bimodal distribution around 5-10° and 35-60°. The first one represents low misorientation among grains and the second one demonstrates the high misorientation among them.
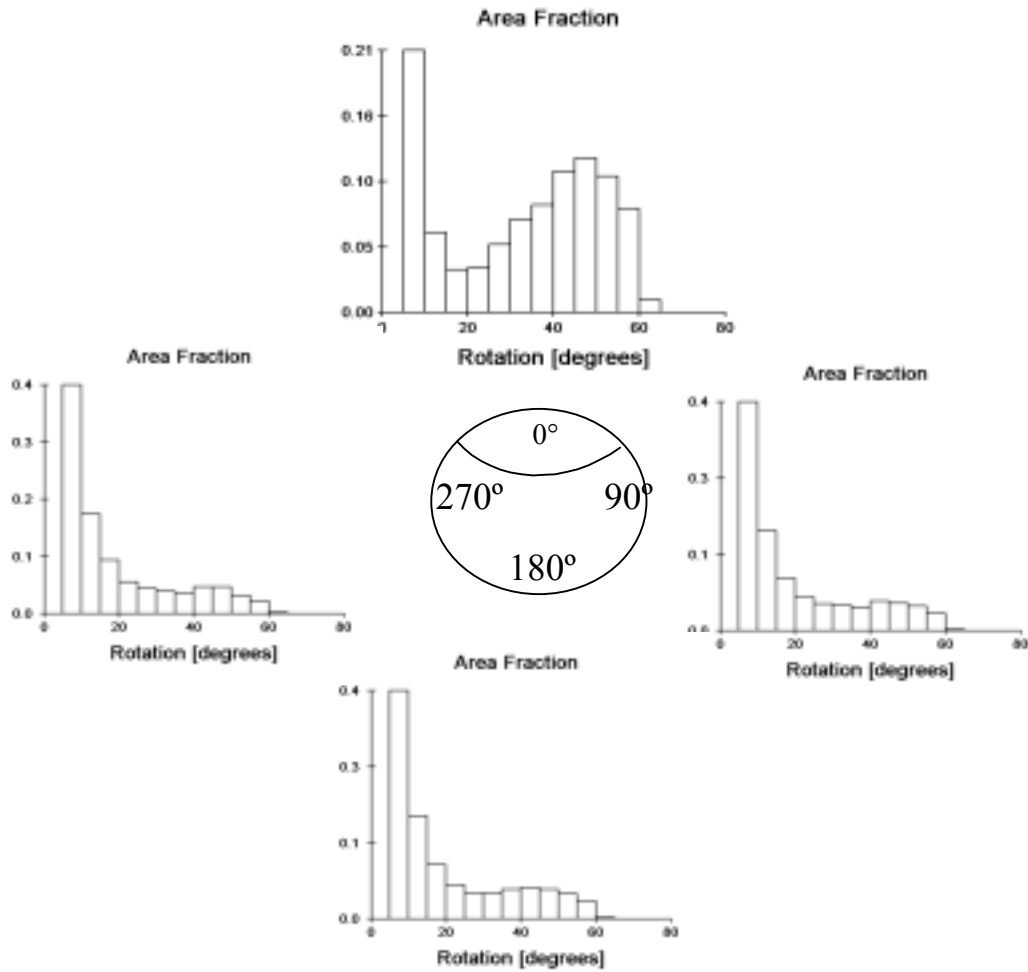
Figure 5.5 – The misorientation profile among grains of the 10.0mm diameter sample.

Four regions were also analyzed on the 5.5mm diameter wire rod sample. The difference was that the first region was randomly chosen since there was no proeutectoid cementite network close to the edge. The first analyzed region was identified as 0°. The others were chosen in the same way as before. Then, the second, third, and fourth analyzed regions were identified as 90°, 180°, and 270°, respectively. Figure 5.6 shows that according to these analyses, no region with a bimodal distribution of the misorientation among grain boundaries was found. The circle in the

middle of the four graphs represents the transversal section of a 5.5mm diameter sample. The numbers inside of the circle represents the regions where the analyses were performed.
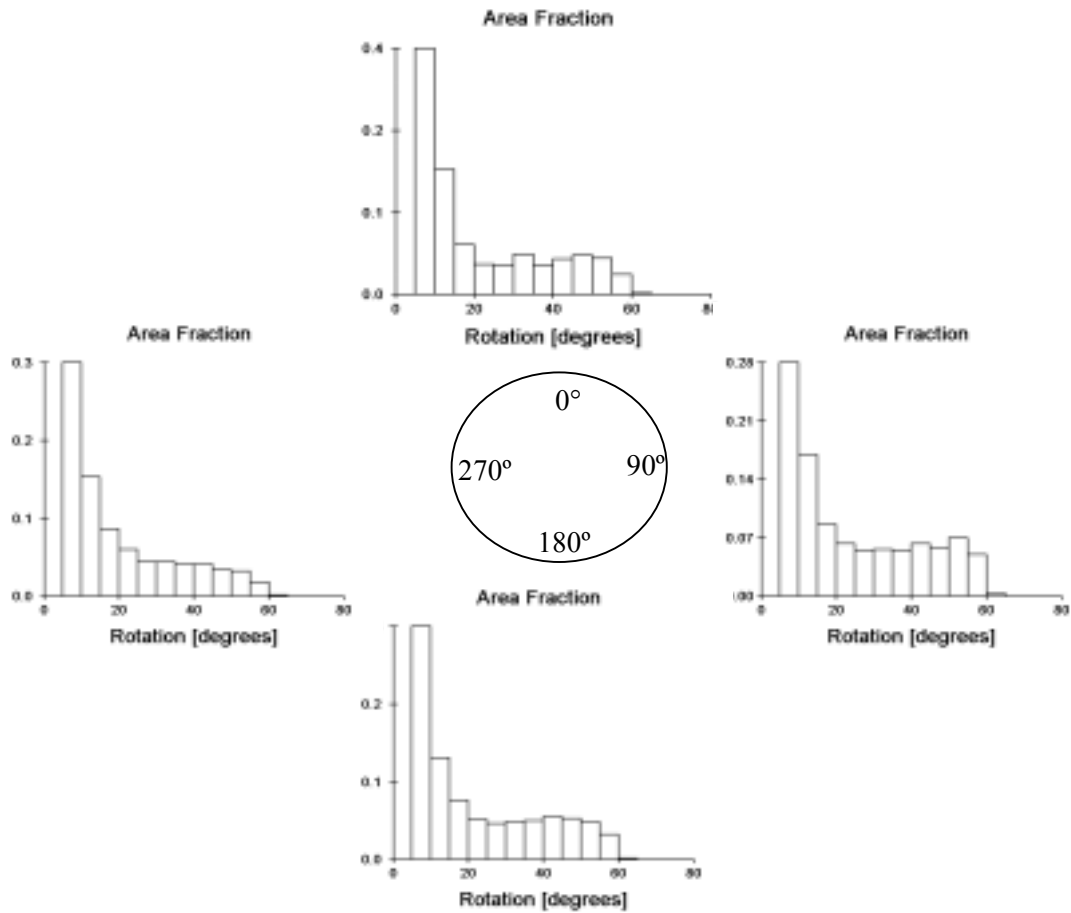
Figure 5.6 – The misorientation profile among grains of the 5.5mm diameter sample.

5.3 DILATOMETRIC RESULTS

Dilatometric experiments were performed in order to estimate the minimum cooling rate necessary to avoid the formation of the proeutectoid cementite. However, while conducting the experiments, the idea of testing different atmospheres arose. The results using helium to cool down the samples will be shown first. Here, a CCT diagram for this hypereutectoid steel is also included, and later on the results of the other atmospheres (air, and vacuum) are presented.

5.3.1 Dilatometric Results in Helium

Figure 5.7 a shows the dilatometric results for the cooling rate of 1K/s. It shows a complete curve, including the heating of the sample from room temperature up to 1193K with a 10K/s heating rate and the cooling of the sample from 1193K down to room temperature with a cooling rate of 1K/s. Here, the extension of the sample can be read on the left axis (blue dashed line) and dT/dt is read on the right axis (red solid line). Other dilatometric experiments were performed in the same way, varying only the cooling rate and the atmosphere in each case. However, only the region of the austenite to proeutectoid cementite and carbon depleted austenite to pearlite transformations are shown in the following figures. Therefore, they have to be read from the right to the left. Figure 5.7 b shows a detailed view of the two transformation regions presented in Figure 5.7 a. The beginning of the first transformation indicated here by (Cs) is the austenite to proeutectoid cementite transformation, and the start of the second one, (Ps), is the carbon depleted austenite to pearlite transformation.

Figure 5.7.a – Dilatrometric results of the 1K/s cooling rate curve in which the sample was cooled in helium.

Figure 5.7.b – Detailed view of the two transformations observed in the dilatometric results of the 1K/s cooling rate curve in which the sample was cooled in helium.

When the transformation is completed, the cooling rate tends to be constant again. At Cs and Ps, a certain amount of released heat decreases dT/dt. The dilatometer reacts, thereby increasing the flow of helium gas to reach the set cooling rate (1K/s). This phenomenon is very clear in Figure 5.9. This causes the cooling rate to reach values below the set one (Figure 5.10). When this happens, the dilatometer immediately regulates the flow of gas to reestablish the set cooling rate.

As the cooling rate increases, the first transformation becomes less evident. At the cooling rate of 12K/s and above, just one transformation (austenite to pearlite) is observed. Figures 5.8 to 5.15 show a detailed view of the dilatometric experiments using cooling rates of 2, 3, 6, 9, 12, 15,18, and 21K/s, respectively.
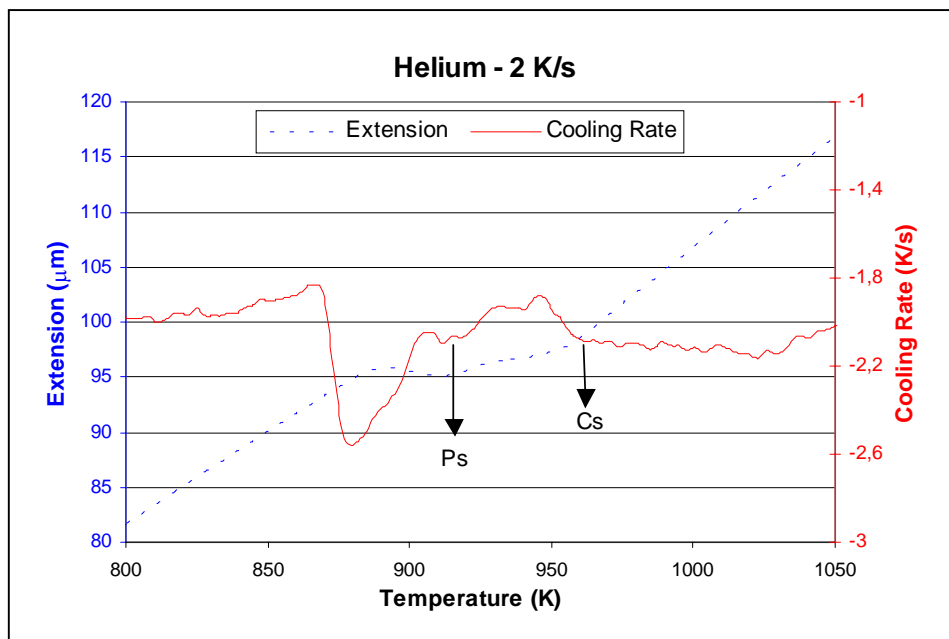
Figure 5.8 – Detailed view of two transformations (austenite to proeutectoid cementite and remaining austenite to pearlite) observed in the dilatometric results of the 2K/s cooling rate curve in which the sample was cooled in helium.
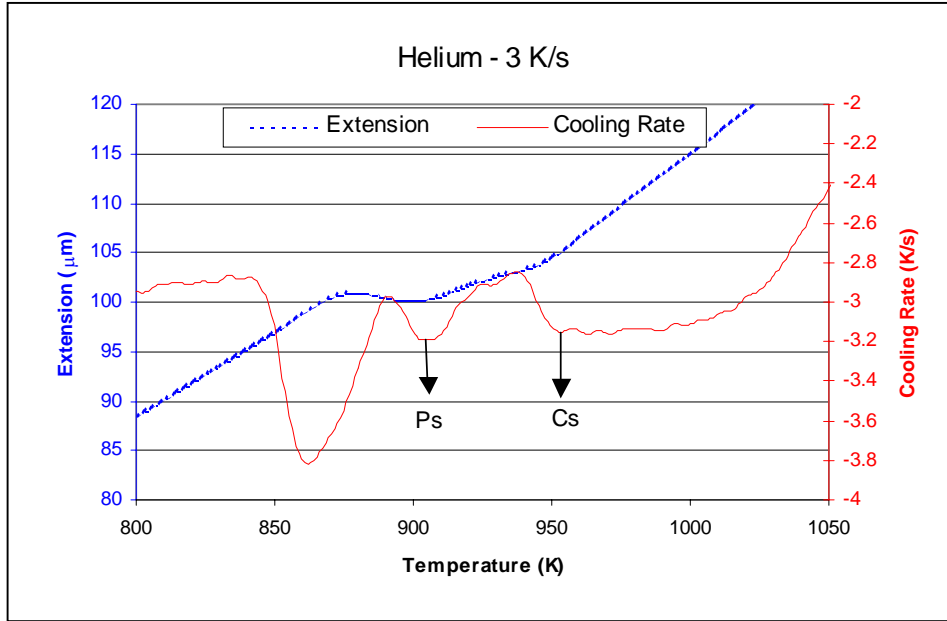
Figure 5.9 – Detailed view of two transformations (austenite to proeutectoid cementite and remaining austenite to pearlite) observed in the dilatometric results of the 3K/s cooling rate curve in which the sample was cooled in helium.
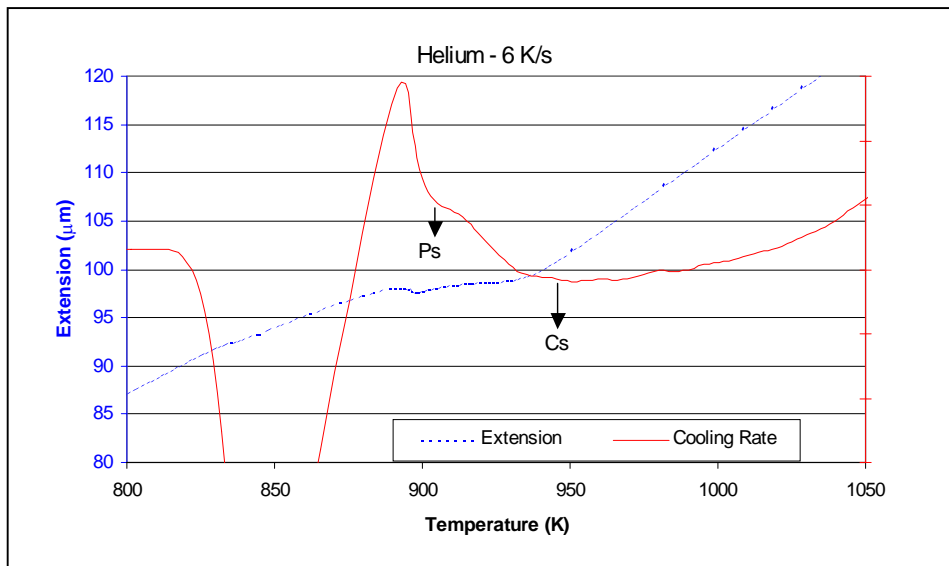
Figure 5.10 – Detailed view of two transformations (austenite to proeutectoid cementite and remaining austenite to pearlite) observed in the dilatometric results of the 6K/s cooling rate curve in which the sample was cooled in helium.
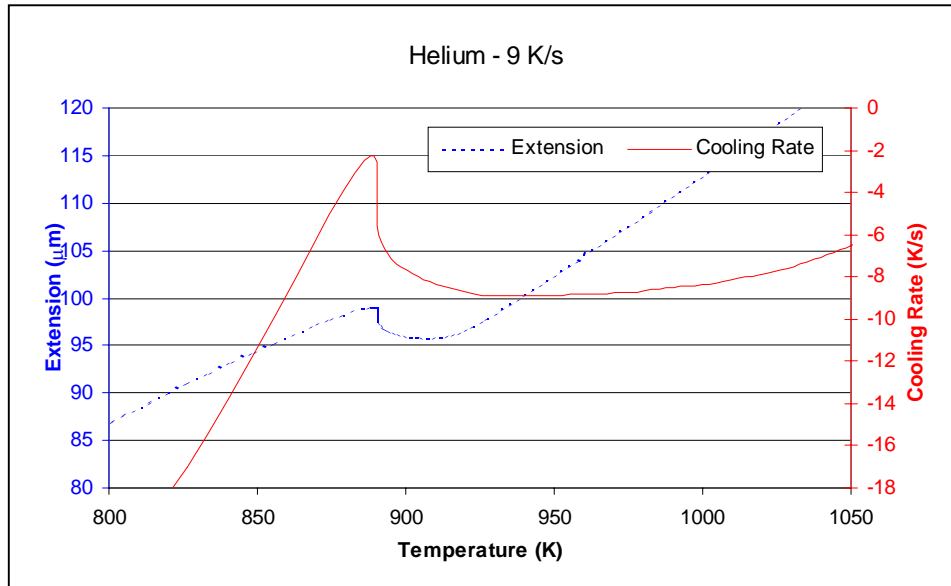
Figure 5.11 – Detailed view of two transformations (austenite to proeutectoid cementite and remaining austenite to pearlite) observed in the dilatometric results of the 9K/s cooling rate curve in which the sample was cooled in helium.

Figure 5.12 – Detailed view of the austenite to pearlite transformation observed in the dilatometric results of the 12K/s cooling rate curve in which the sample was cooled in helium.

Figure 5.13 – Detailed view of the austenite to pearlite transformation observed in the dilatometric results of the 15K/s cooling rate curve in which the sample was cooled in helium.

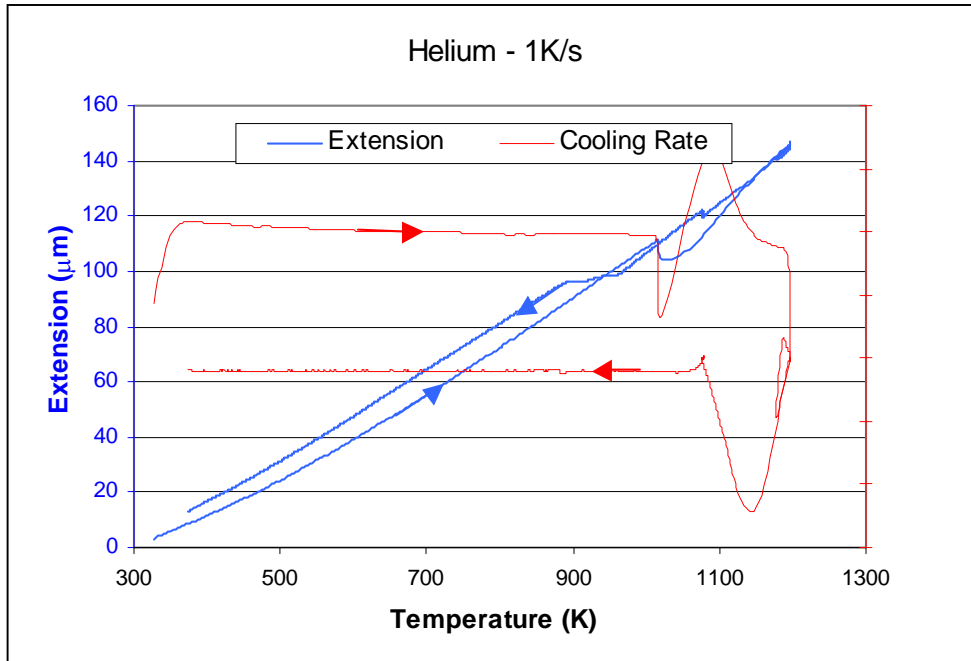Figure 5.14 – Detailed view of the austenite to pearlite transformation observed in the dilatometric results of the 18K/s cooling rate curve in which the sample was cooled in helium.

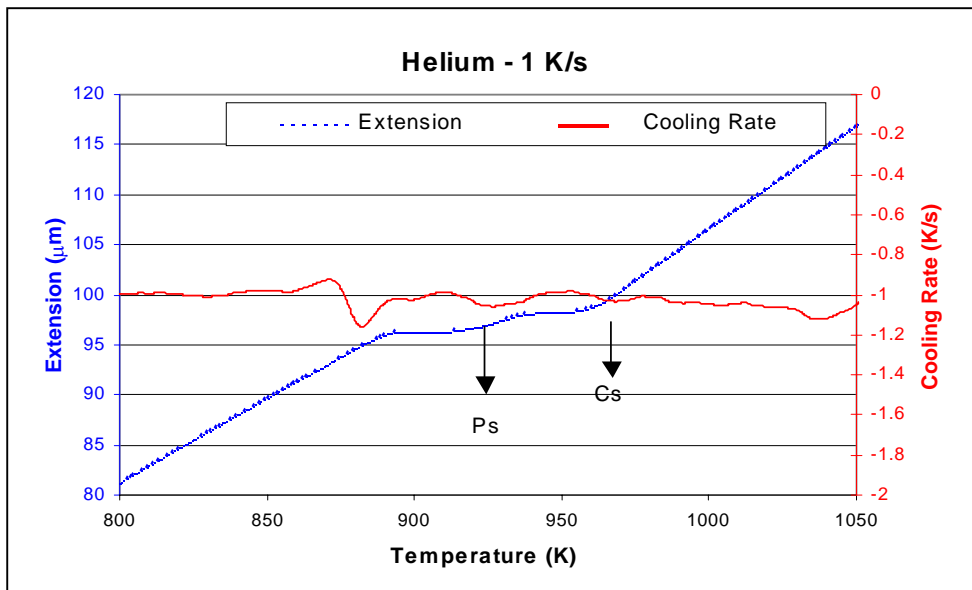Figure 5.15 – Detailed view of austenite to pearlite transformation observed in the dilatometric results of the 21K/s cooling rate curve in which the sample was cooled in helium.

A CCT curve for the SAE 1092 was created based on the dilatometric data in which the samples were cooled in helium. A polynomial derivative,[46] dE/dT, was used to determine the exact point of the beginning of the transformations. The equation used for this polynomial derivative is:

$$\frac{dE}{dT} = \frac{\left(E_1 - 8*E_2 + 8*E_4 - E_5\right)}{12\Delta T} \qquad (5.1)$$

Where:

$\dfrac{dE}{dT}$ is the derivative of the extension over the temperature;

E_1, E_2, E_4 e E_5 are the extension at four consecutive points;

ΔT corresponds to the temperature difference between T_5 and T_1 divided by 4.

Five percent of the deviation on the dE/dT vs. temperature curve was the criterion used to determine the start of the transformations. The temperature at the end of the pearlite to austenite transformation upon heating was taken upon cooling as the start point to measure the time for each transformation. Figure 5.16 shows the dE/dT and dT/dt versus temperature curves for the cooling rate of 1K/s. The temperatures used to build the CCT diagram are marked over the dE/dT curve. Where Cs stands for the beginning of the proeutectoid cementite, Ce end of the proeutectoid cementite, Ps beginning of pearlite, and Pe end of pearlite.

At low cooling rates (up to 9K/s), austenite to proeutectoid cementite and carbon-depleted austenite to pearlite transformations were observed. However, at cooling rates higher than 9K/s, only the austenite to pearlite transformation was observed. Figure 5.17 shows a CCT curve and four photomicrographs characterizing the microstructure of the dilatometric results using the cooling rate of 1, 3, 12, and 21K/s, respectively.
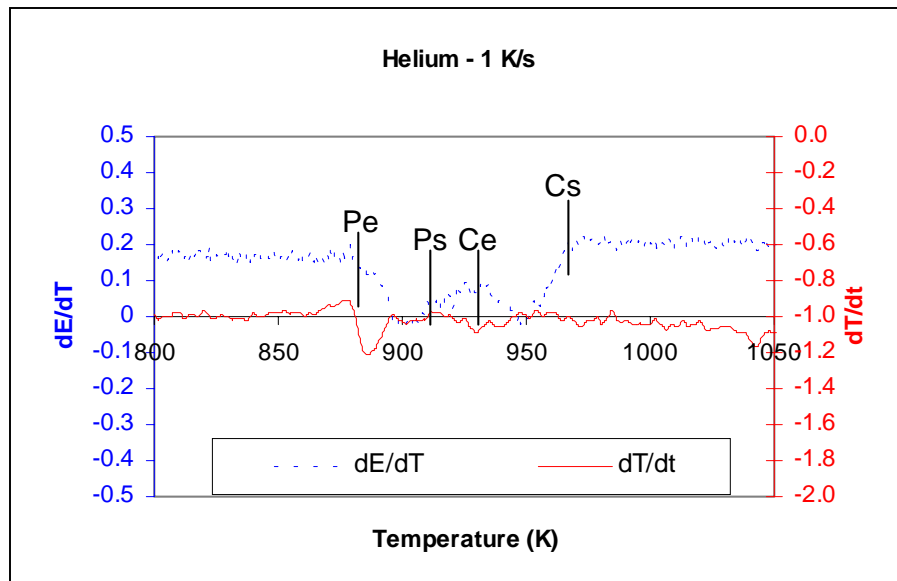
Figure 5.16 – dE/dT and dT/dt versus temperature curves used to build the CCT diagram for SAE 1092.

According to the CCT curve, 12K/s is the minimum cooling rate to avoid the formation of the proeutectoid cementite.
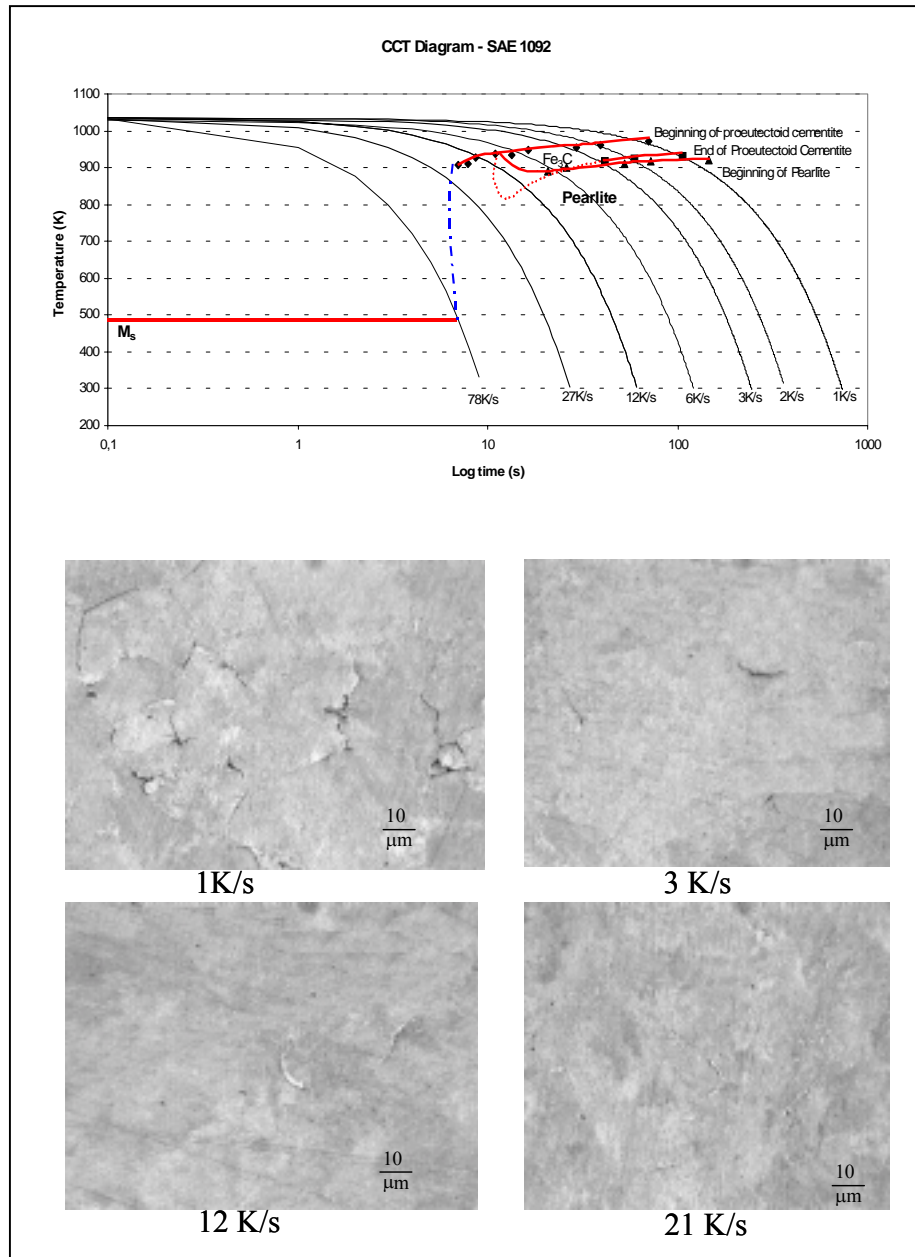
Figure 5.17 – CCT curve of SAE 1092 and four photomicrographs characterizing the microstructure of the dilatometric results using the cooling rate of 1, 3, 12, and 21K/s, respectively.

5.3.2 Dilatometric Results in Air

The dilatometric experiments were also performed in air. Figures 5.18 to 5.24 show a detailed view of the dilatometric experiments using air to cool the samples in the chamber with cooling rates of 1, 2, 3, 6, 9, 12, and 15K/s, respectively. Figure 5.18 shows that the deviation of the cooling rate of the set one is smoother than the one in which the samples were cooled in helium. When the samples are cooled in air, 9K/s is enough to avoid the formation of the proeutectoid cementite. In other words, just one transformation (austenite to pearlite) is present for cooling rates of 9K/s in air and above.
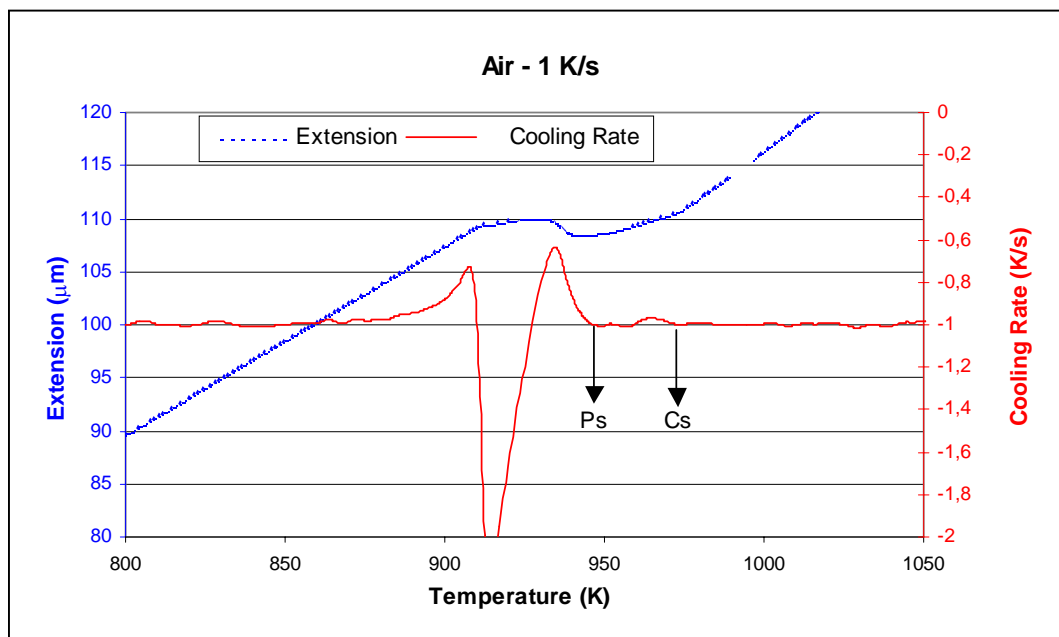
Figure 5.18 – Detailed view of two transformations (austenite to proeutectoid cementite and remaining austenite to pearlite) observed in the dilatometric results of the 1K/s cooling rate in which the sample was cooled in air.
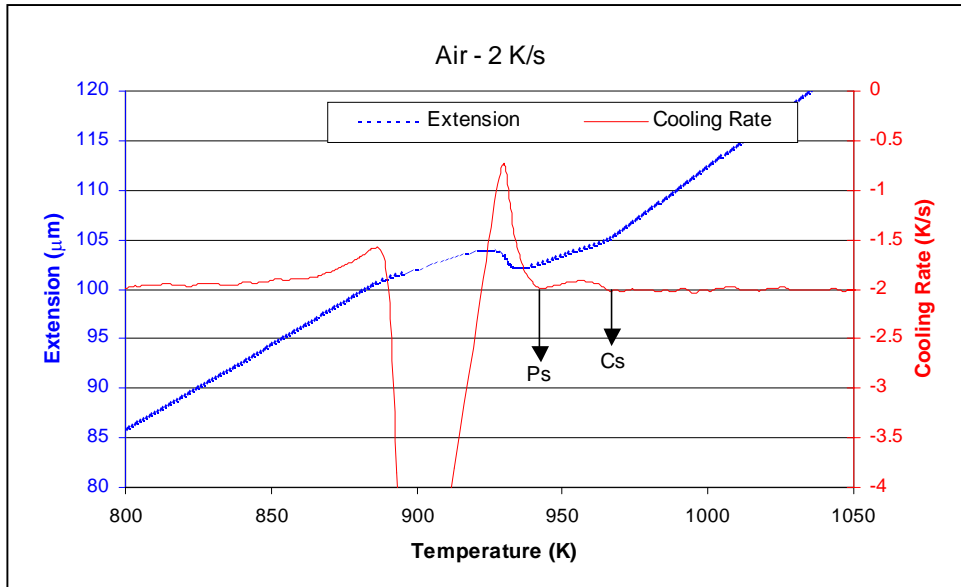
Figure 5.19 – Detailed view of two transformations (austenite to proeutectoid cementite and remaining austenite to pearlite) observed in the dilatometric results of the 2K/s cooling rate curve in which the sample was cooled in air.
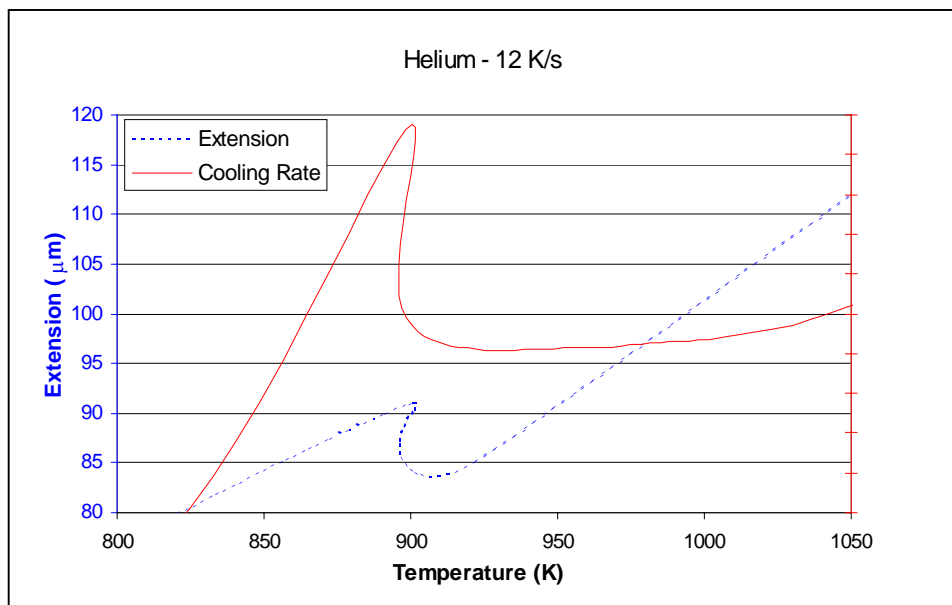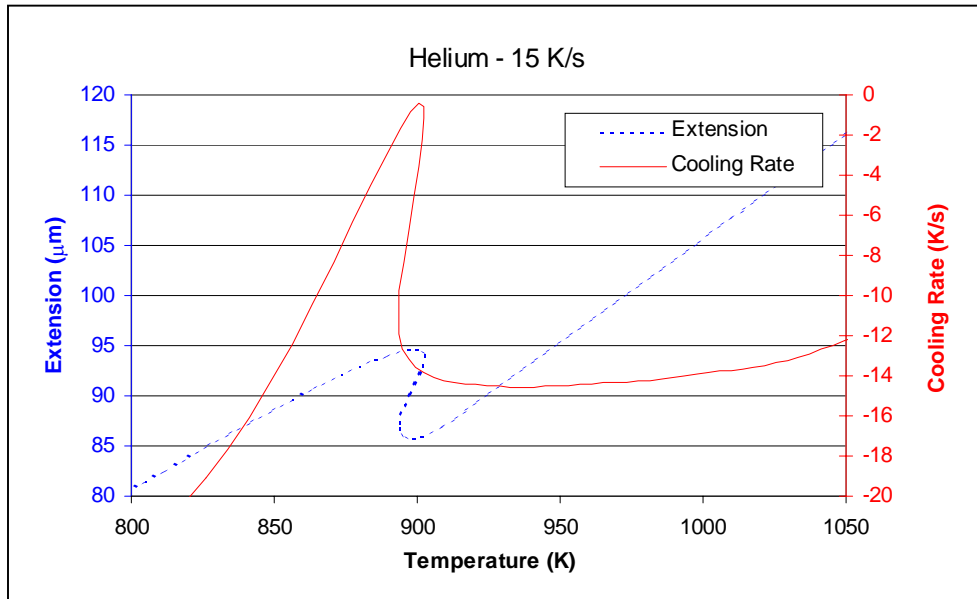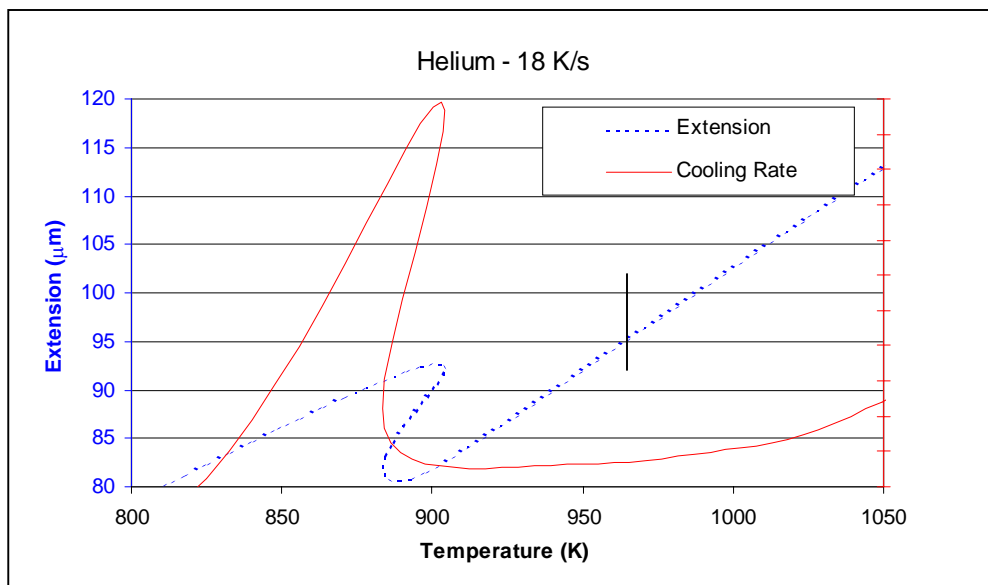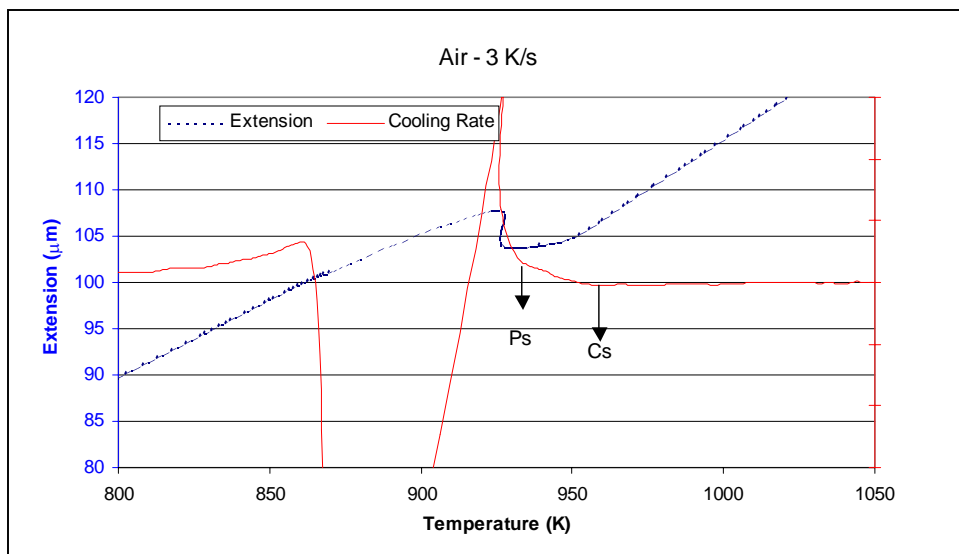

Figure 5.20 – Detailed view of two transformations (austenite to proeutectoid cementite and remaining austenite to pearlite) observed in the dilatometric results of the 3K/s cooling rate curve in which the sample was cooled in air.
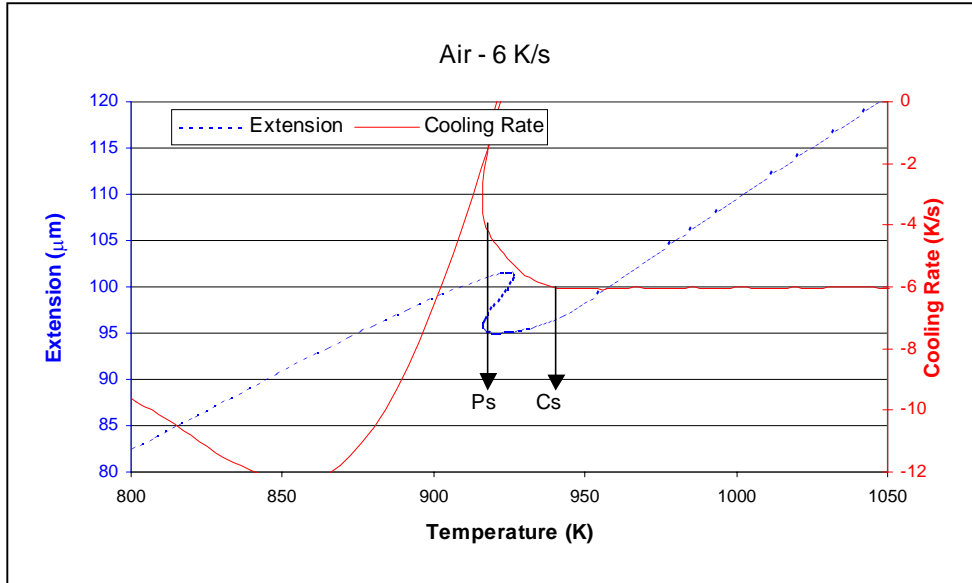
Figure 5.21 – Detailed view of two transformations (austenite to proeutectoid cementite and remaining austenite to pearlite) observed in the dilatometric results of the 6K/s cooling rate curve in which the sample was cooled in air.
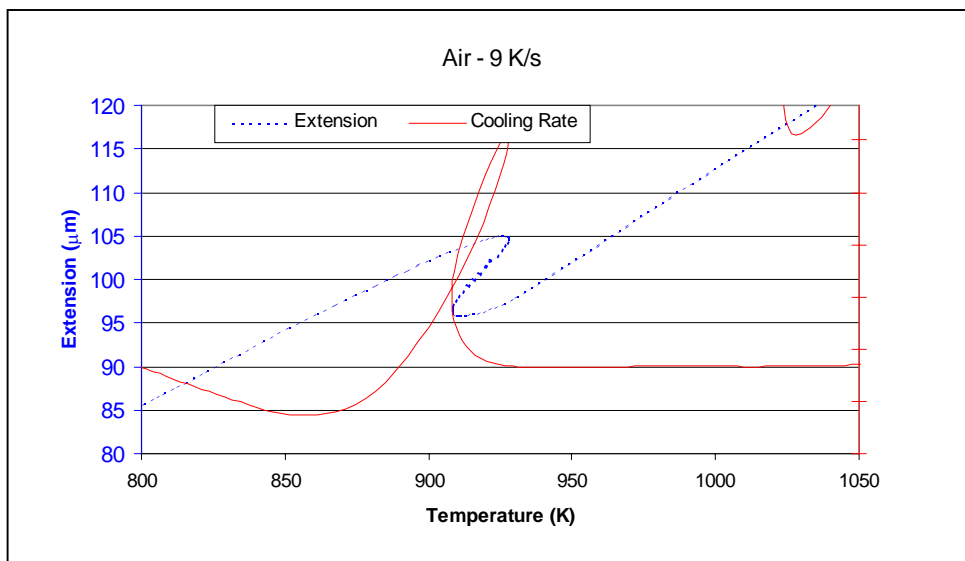
Figure 5.22 – Detailed view of the austenite to pearlite transformation observed in the dilatometric results of the 9K/s cooling rate curve in which the sample was cooled in air.
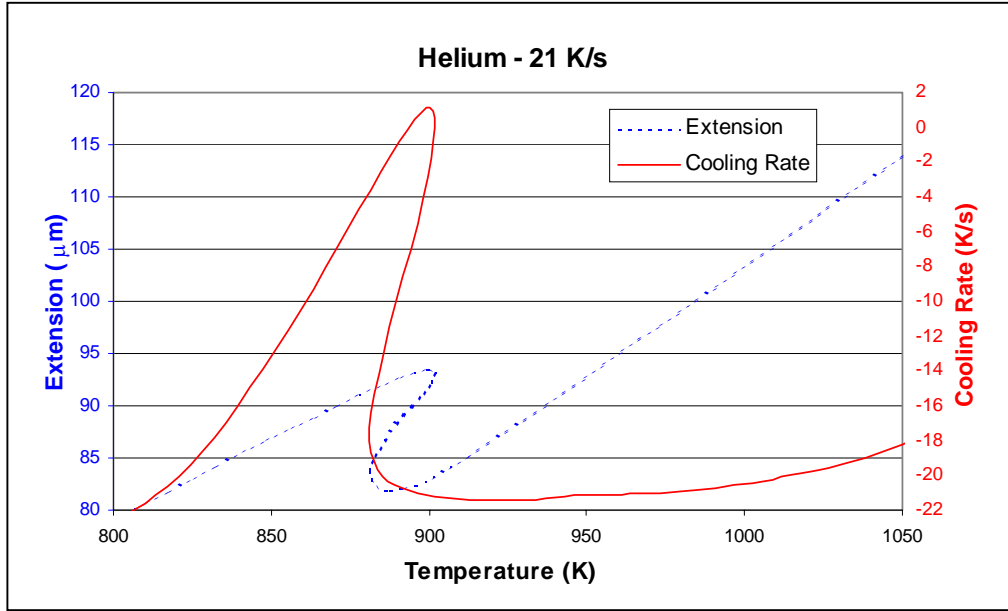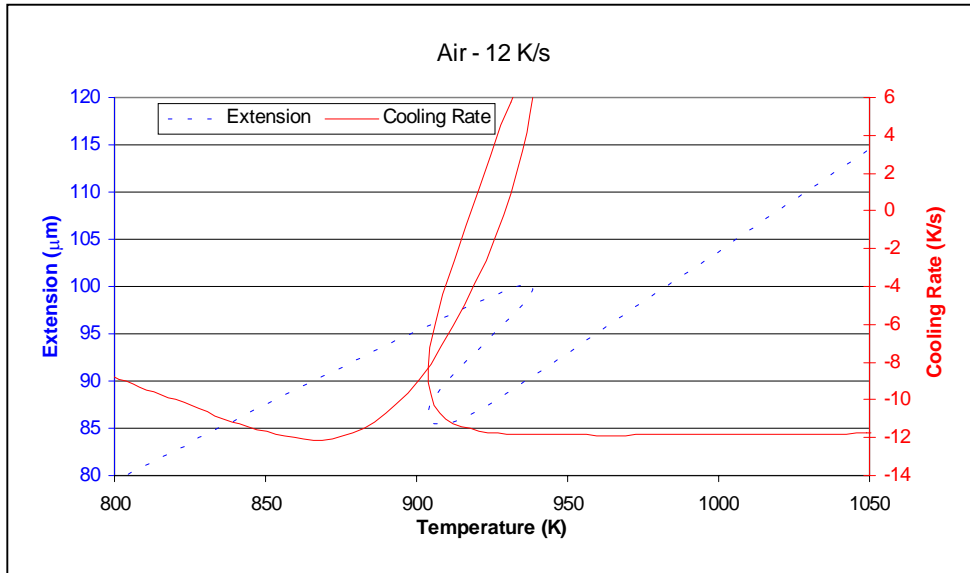
Figure 5.23 – Detailed view of the austenite to pearlite transformation observed in the dilatometric results of the 12K/s cooling rate curve in which the sample was cooled in air.
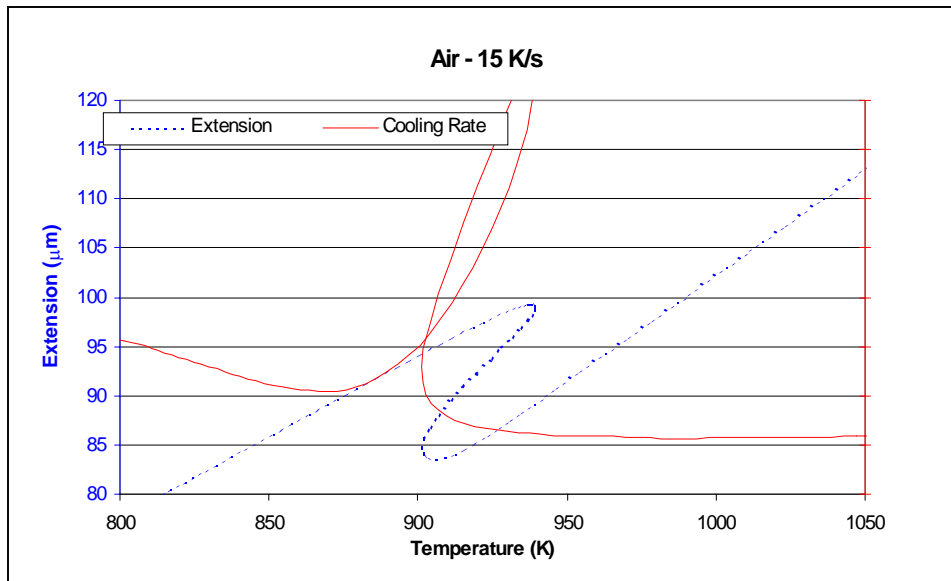
Figure 5.24 – Detailed view of the austenite to pearlite transformation observed in the dilatometric results of the 15K/s cooling rate curve in which the sample was cooled in air.

5.3.3 Dilatometric Results under Vacuum

Figures 5.25 to 5.30 show a detailed view of the dilatometric studies in which the samples were cooled under vacuum. The cooling rates used were 1, 2, 3, 6, 9, and 12K/s, respectively. Figure 5.25 shows only the austenite to pearlite transformation. Therefore, the austenite to proeutectoid cementite transformation was suppressed when the sample was under vacuum even for very low cooling rates, e.g., 1K/s.
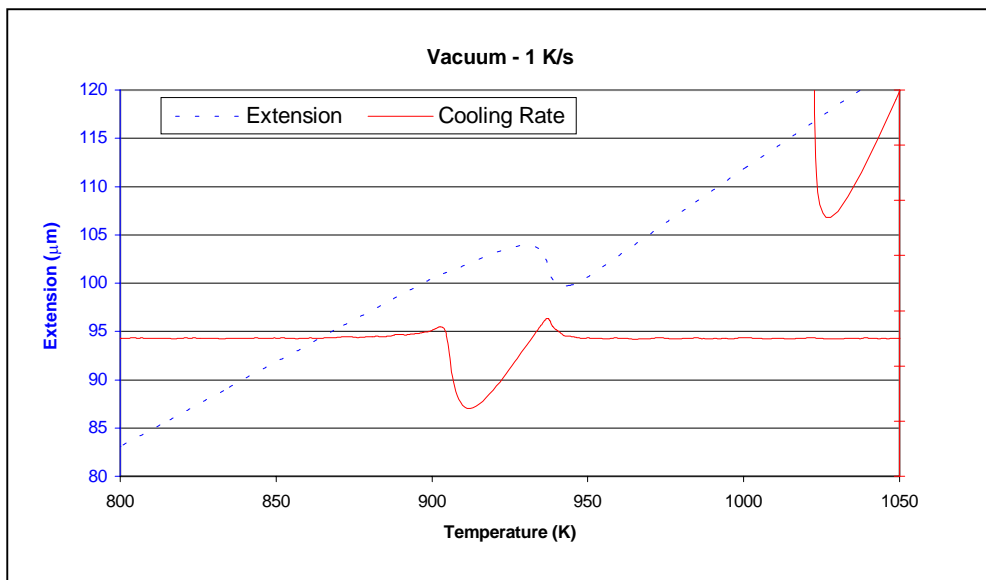
Figure 5.25 – Detailed view of the austenite to pearlite transformation observed in the dilatometric results of the 1K/s cooling rate curve in which the sample was cooled under vacuum.
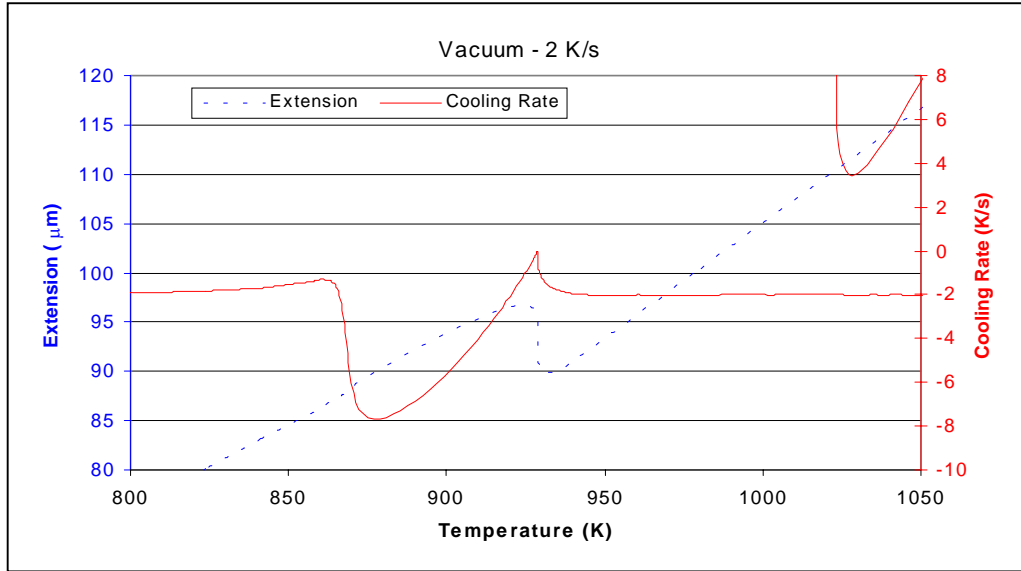
Figure 5.26 – Detailed view of the austenite to pearlite transformation observed in the dilatometric results of the 2K/s cooling rate curve in which the sample was cooled under vacuum.
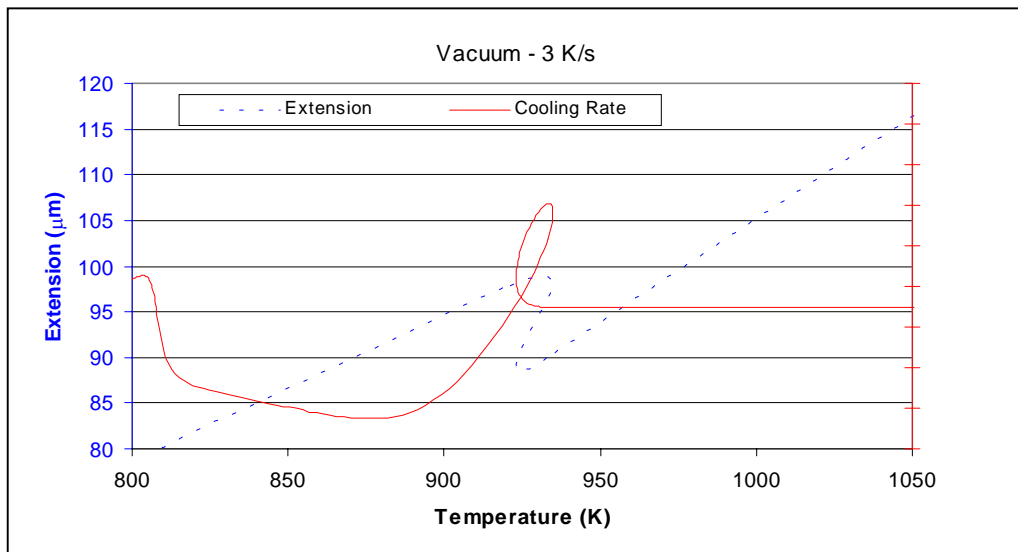
Figure 5.27 – Detailed view of the austenite to pearlite transformation observed in the dilatometric results of the 3K/s cooling rate curve in which the sample was cooled under vacuum.
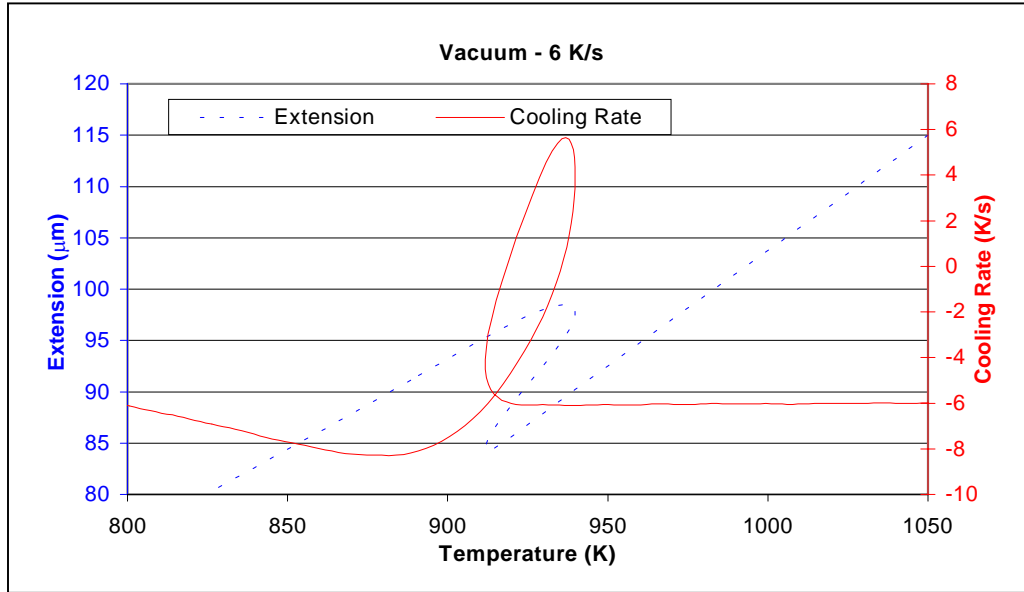
Figure 5.28 – Detailed view of the austenite to pearlite transformation observed in the dilatometric results of the 6K/s cooling rate curve in which the sample was cooled under vacuum.
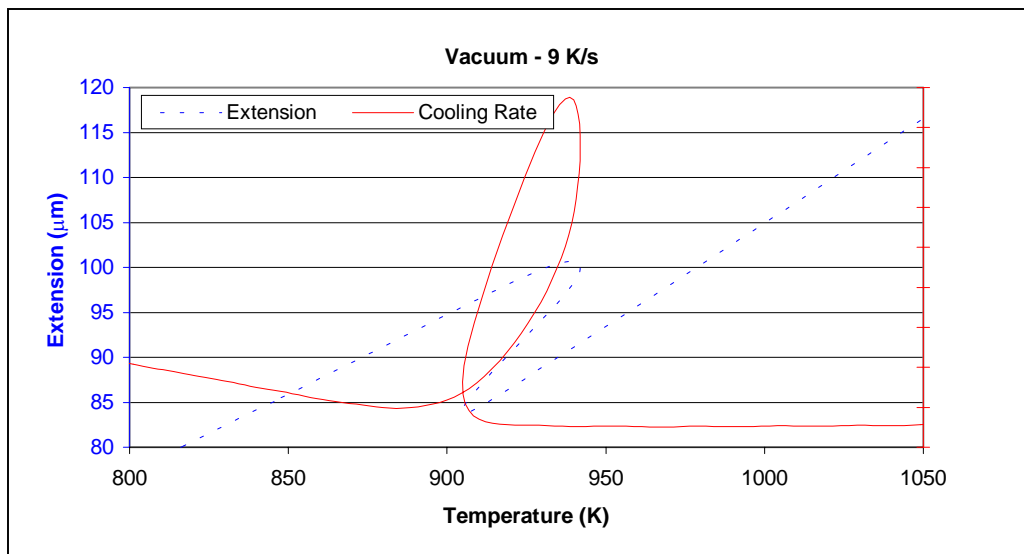
Figure 5.29 – Detailed view of the austenite to pearlite transformation observed in the dilatometric results of the 9K/s cooling rate curve in which the sample was cooled under vacuum.
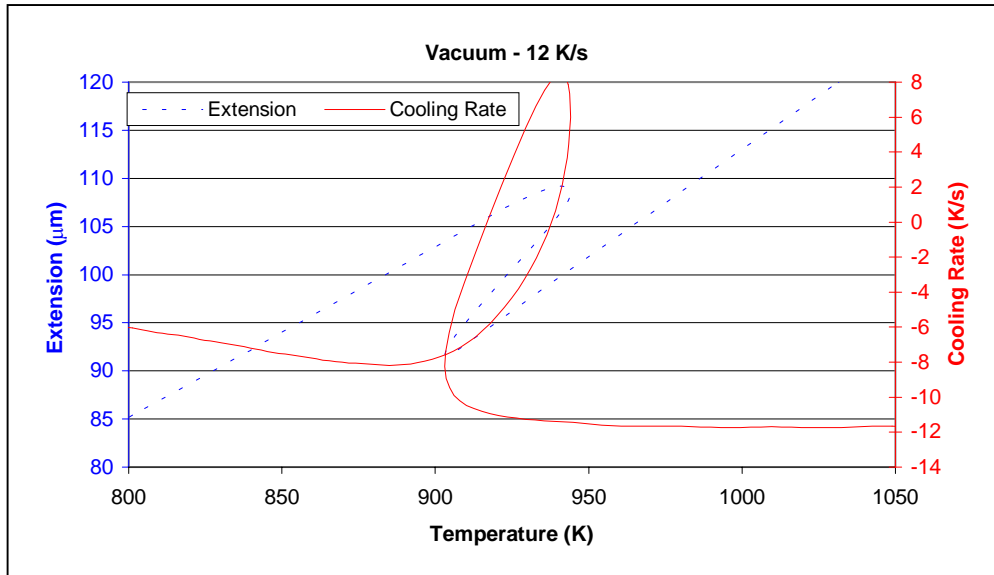
Figure 5.30 − Detailed view of the austenite to pearlite transformation observed in the dilatometric results of the 12K/s cooling rate curve in which the sample was cooled under vacuum.

5.3.4 Microstructural Results of the Dilatometric Samples

After the experiments were performed, all samples were analyzed to quantify the amount of proeutectoid cementite formed under each condition. Figure 5.31 shows how many austenitic grain boundaries are covered with proeutectoid cementite. Figure 5.31 shows that for low cooling rates, the austenite to proeutectoid cementite transformation is very dependent on the environment in which the sample is cooled. For very low cooling rates, i.e., 1K/s, much more proeutectoid cementite is formed when the sample is cooled in helium than when it is done under vacuum. As the cooling rate increases, the difference of the amount of proeutectoid cementite formed under the three tested conditions (vacuum, air, and helium) decreases. At high cooling rates (above 9K/s), the environment does not strongly influence the formation of the proeutectoid cementite.

Effect of the atmosphere on the formation of the proeutectoid cementite
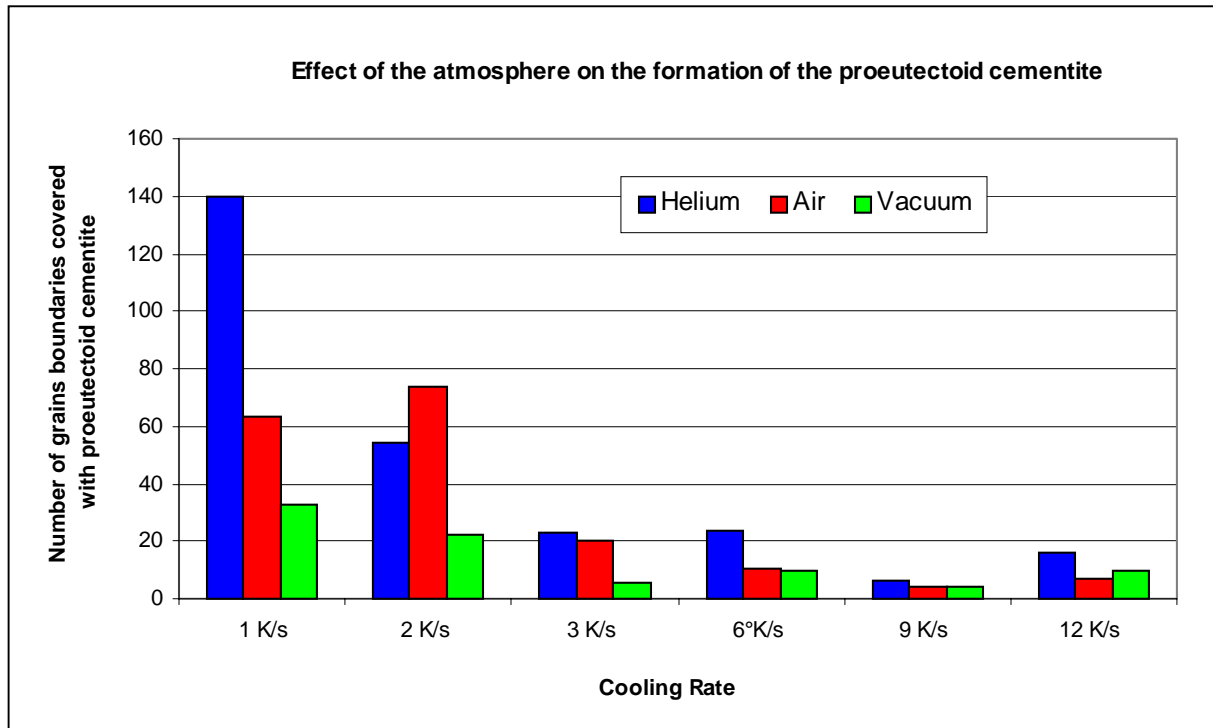
Figure 5.31 – Number of austenitic grain boundaries covered with proeutectoid cementite as a function of the cooling rate and the atmosphere.

5.4 COOLING RATES MEASURED AT THE INDUSTRIAL ROLLING MILL

After checking the minimum cooling rate necessary to avoid the formation of the proeutectoid cementite from the literature, and calculating it from dilatometric data, it was necessary to calculate it in the conveyor process of Belgo at Monlevade's plant.

The temperature as a function of time was measured along a coil on the conveyor for several wire rod diameters. Figure 5.32 shows the cooling rate as a function of the diameter of the wire rod. Figure 5.32 shows that a proeutectoid cementite network is observed in wire rods with diameters above 8.0mm. Thus characterizing safe region regarding the precipitation of this brittle phase if size is larger than 8.0mm.
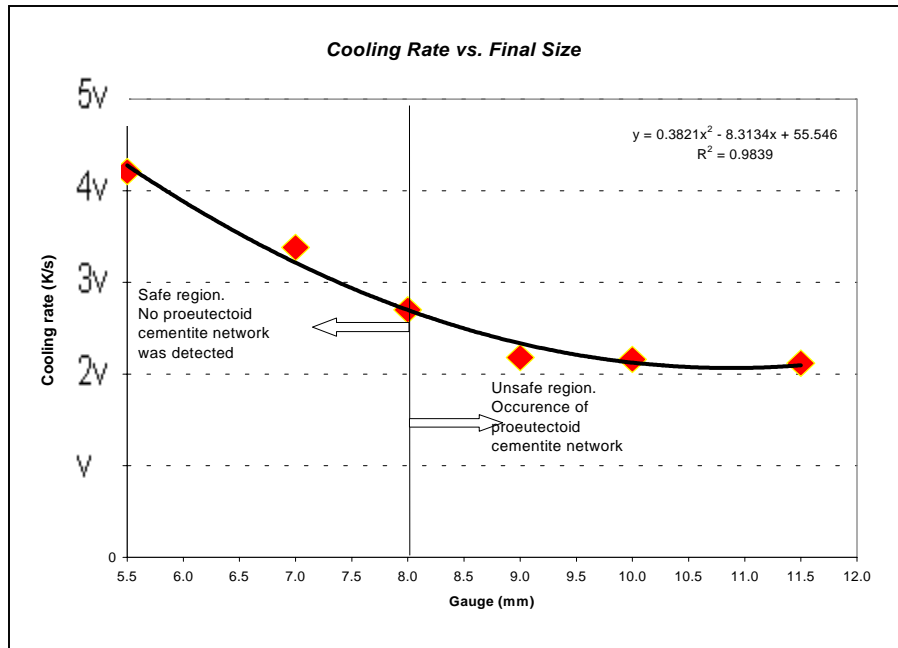
Figure 5.32 – Calculated cooling rate as a function of the diameter of the wire rod for the Belgo's conveyor at Monlevade's plant.

For the remainder of this discussion, all of the cooling rates measured in the plant will be given as a function of V. Here, V is the interval obtained in Figure 5.32.

Two experiments were performed in order to evaluate the influence of the laying head temperature on the cooling rate and on the amount of proeutectoid cementite formed in the industrial process, as well. The first experiment was carried out using the standard laying head temperature and the second was conducted using a lower temperature. For the standard and low laying head temperatures, the calculated cooling rates were 2.4*V, and 1.5*V K/s, respectively.

Table 5.1 shows the established criterion to quantify the proeutectoid cementite observed in the center of the wire rod. For the network close to the surface, the response of the experiments was the length of the network measured in millimeters.

Table 5.1: Criterion used to quantify the amount of cementite in the center of the wire rod.

Index for each experiment	Proeutectoid Cementite
0	Free of proeutectoid cementite.
2	Isolated grain boundaries covered with proeutectoid cementite.
4	Some covered grain boundaries with proeutectoid cementite connected. However, there are no grains in which all boundaries are covered with proeutectoid cementite.
8	One to four grains have all the boundaries covered with proeutectoid cementite.
16	Five or more grains have all the boundaries completed covered with proeutectoid cementite.

Tables 5.2 and 5.3 show the results of proeutectoid cementite for both conditions.

Table 5.2: Results of proeutectoid cementite for the rolling using the standard laying head temperature

Coil	Index of proeutectoid cementite in the center of the wire rod according to table 5.1		Extension of the proeutectoid cementite network close to the surface of the wire rod (mm/sample)	
	Head	Tail	Head	Tail
1	2	8	0	9
2	2	2	7	0
3	2	2	0	11
4	8	4	0	10
5	2	2	0	12
6	2	2	0	11
7	2	2	0	12
8	8	2	0	13
Average	4	3	1	10

Table 5.3: Result of proeutectoid cementite for the rolling using a lower laying head temperature

Coil	Index of proeutectoid cementite in the center of the wire rod according to table 5.1		Extension of the proeutectoid cementite network close to the surface of the wire rod (mm/sample)	
	Head	Tail	Head	Tail
1	0	0	16	14
2	0	0	9	14
3	0	2	15	9
4	2	8	10	11
5	2	4	14	12
6	0	2	9	11
7	2	0	0	11
8	0	0	0	10
Average	1	2	9	12

5.5 EXPERIMENTS DESIGNED TO REDUCE THE PROEUTECTOID CEMENTITE

In order to determine the best parameters to produce the SAE 1092 free of proeutectoid cementite network at Belgo's plant, a statistically designed experimental program was carried out. This program was composed of three variables, each having two levels. Therefore, eight experiments were necessary to carry out a full factorial (matrix of experiments is equal to 2^3). The tested variables were selected based on previous results of EBSD, dilatometer, and literature review. The variables are listed below.

➢ Laying head temperature;

➢ Speed of the cooling conveyor;

➢ Electromagnetic stirring in the mold during the continuous casting process.

The levels were always low and high, respectively. Table 5.4 shows the DOE as the experiments were conducted during the rolling process.

Table 5.4: Statistically Designed Experiments carried out to determine the parameters to produce the SAE 1092 free of proeutectoid cementite network. Full factorial, three factors, two levels, eight experiments.

Experiment	Electromagnetic Stirring	Speed of the Cooling Conveyor	Laying Head Temperature
1	Low	Low	Low
2	High	Low	Low
3	Low	High	Low
4	High	High	Low
5	Low	Low	High
6	High	Low	High
7	Low	High	High
8	High	High	High

5.6 RESULTS OF THE STATISTICALLY DESIGNED EXPERIMENTS TO MINIMIZE THE

PROEUTECTOID CEMENTITE

The responses to evaluate the best level of each variable were proeutectoid cementite, tensile strength, and cooling rate. The proeutectoid cementite was evaluated according to Table 5.1. Table 5.5 summarizes all responses (obtained results) and Figures 5.33 to 5.35 show the response diagrams.

Table 5.5: Summary of the responses of the experiments of the Statistically Design of Experiments.

| Experiment | Responses | | |
	Index of proeutectoid cementite in the center of the wire rod according to Table 5.1	Tensile Strength (MPa)	Calculated Cooling Rate (K/s)
1	5	1175	1.12*V
2	5	1173	
3	3	1180	1.98*V
4	2	1172	
5	2	1172	1.32*V
6	6	1194	
7	2	1178	2.16*V
8	2	1185	

The first observation was that no proeutectoid cementite close to the surface was detected. Here, all tested conditions were already optimized in order to suppress the formation of this network.
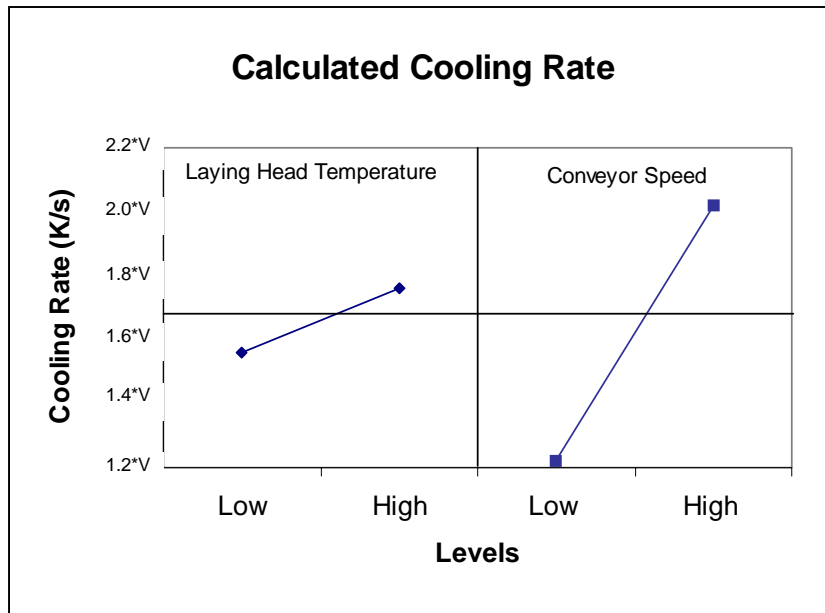
Figure 5.33 – Response diagram for "Cooling Rate".
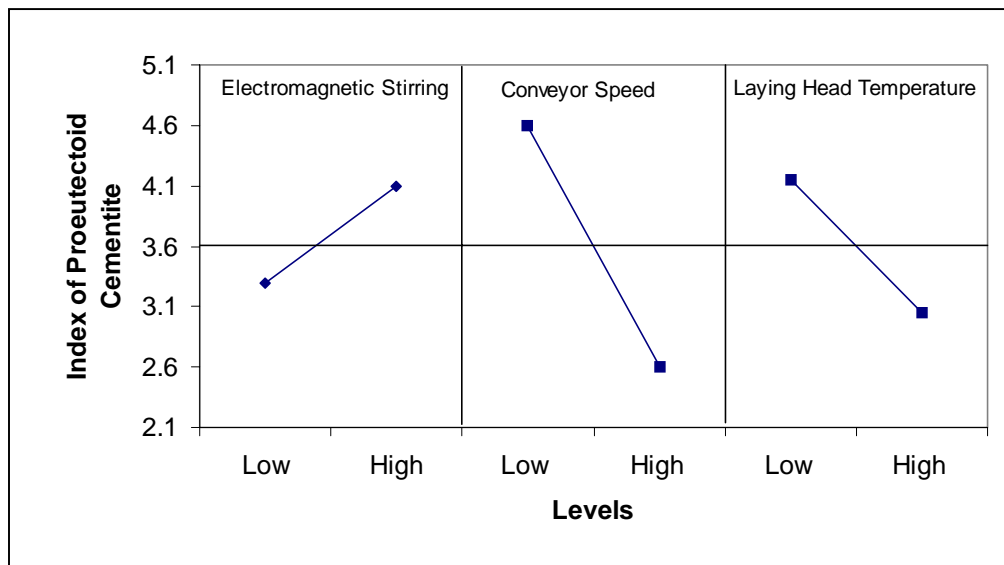
Figure 5.34 – Response diagram for "Index of Proeutectoid Cementite".
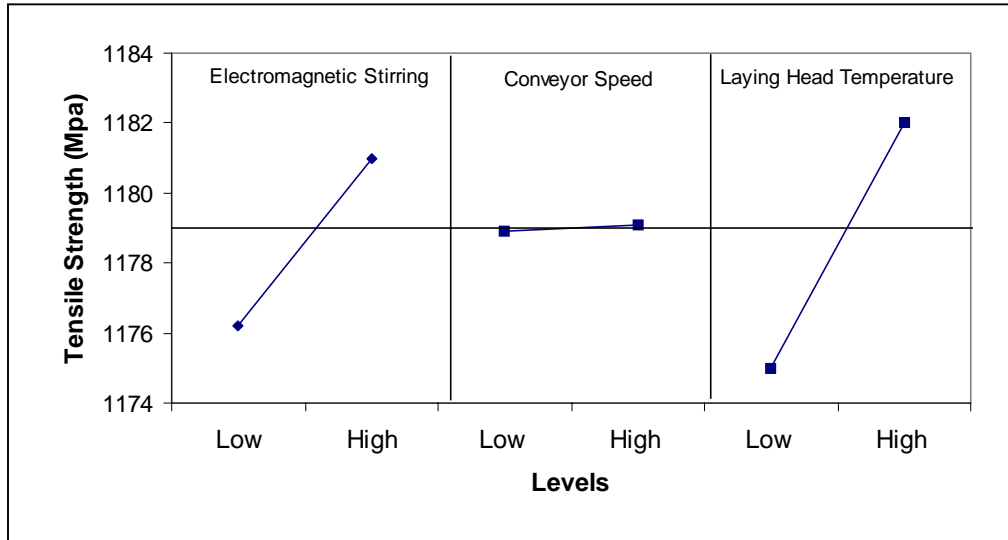
Figure 5.35 – Response diagram for "Tensile Strength".

6.0 DISCUSSION OF THE RESULTS

6.1 CHARACTERIZATION OF THE PROEUTECTOID CEMENTITE

The microstructural characterization showed that for small diameter wire rods (5.5, 6.5, and 8.0mm), the proeutectoid cementite network was not observed. On the other hand, a proeutectoid cementite network was observed in the center and also close to the edge on large diameter wire rod samples (10.0, and 11.5mm).

6.2 FORMATION OF THE PROEUTECTOID CEMENTITE NETWORK IN THE CENTER AND CLOSE TO THE SURFACE

The formation of the proeutectoid cementite network in the center and close to the surface has distinct causes. One of the reasons for the proeutectoid cementite network in the center of large diameter wire rods is a lower cooling rate than that in wire rods with small diameters when the cooling conditions are the same. In addition to this, segregation of the carbon in the center of the billet during the continuous casting process also contributes to the formation of the proeutectoid cementite in the center of the wire rod. However, electromagnetic stirring in the mold of the continuous casting machine tested at higher levels did not show any better results regarding the reduction of the proeutectoid cementite in the center of the 11.5mm diameter wire rods. This

means that the current electromagnetic stirring level is on the limit regarding its influence on decreasing the amount of formed proeutectoid cementite. According to Ikuo Ochiai et al.,[20] no proeutectoid cementite is precipitated on a cooling conveyor cooled wire rod as long as the C content of steel is less than approximately 1.10 wt percent. However, it was observed that for the conveyor process at Belgo's plant the Ochiai and co-workers observation was only confirmed for sizes below 8.0mm. Therefore, as shown in Figure 5.32, wire rods with diameters above 8.0mm do show proeutectoid cementite network in the center of the wire rod.

The formation of the proeutectoid cementite network close to the edge has another cause. As shown by the EBSD results in Figure 5.5, on the region of this network a bimodal curve of the frequency of the misorientation among grains is observed. This is a characteristic of a recrystallized region. On the other three regions, the curve has just one peak, which means that these regions have a stronger texture than that of the proeutectoid cementite network region.

The recrystallized or the proeutectoid cementite region has a high frequency of the high misorientation among grains, higher than 15° of misorientation. As the misorientation among grains increases, the free energy of the grain boundary also increases. As is known, the interstitial elements have a tendency to segregate to the grain boundaries to decrease their free energy. As all systems tend toward the most stable state, this leads to an increase in the driving force of interstitial elements to segregate to the grain boundaries. Carbon is one interstitial element present in this hypereutectoid steel in a considerable amount. This hypereutectoid steel contains 0.92wt%C.

In order to explain the formation of the proeutectoid cementite network close to the edge at some spots and not at the others, three sketches were drawn. Figure 6.1 (a) shows, schematically, the austenitized steel with the carbon in solid solution homogeneously distributed.

Figure 6.1 (b) shows the carbon atoms segregated to the grain boundaries in a recrystallized region. Figure 6.1 (c) shows carbon atoms distributed in a non-recrystallized region. In a recrystallized region, carbon has a much higher driving force to segregate to the grain boundaries to decrease their free energy than in a non-recrystallized region because in a recristallized region the free energy of the grain boundaries are higher. Therefore, in the recrystallized region, the carbon will segregate to the grain boundary forming the proeutectoid cementite.

b)

Recrystallized region

Austenitized sample

a)

c)

Non-recrystallized region
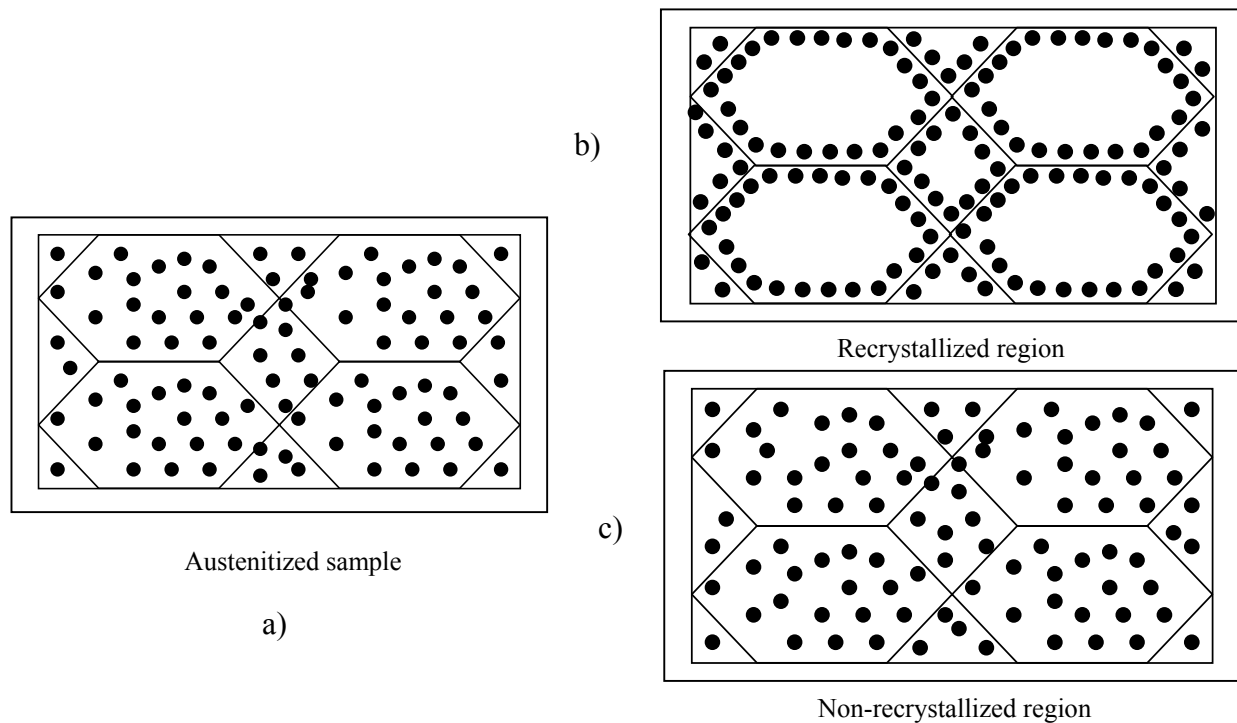
Figura 6.1 – Representation of the carbon atoms in a austenitized sample, (a) segregating to the grain boundaries in the recrystallized region, (b) and staying in the pearlitic matrix in the non-rectystallized region, (c).

6.3 DILATOMETRIC EXPERIMENTS SHOWING THE EFFECT OF THE ENVIRONMENT

ON PHASE TRANSFORMATIONS

The dilatometric tests using helium showed that the minimum cooling rate necessary to avoid the formation of the proeutectoid cementite is 12K/s. The maximum cooling rate that was possible to visualize two distinct deviations on the cooling rate versus temperature curve was 9K/s. After that, i.e., 12K/s, only one deviation was observed. For low cooling rates, the dilatometric results showed two deviations on either the cooling rate versus temperature or extension versus temperature curves. Figure 5.9 shows these two deviations very clearly.

As the cooling rate increases, the amount of heat released during the austenite to pearlite transformation increases. Therefore, the reaction of the dilatometer to restore the set cooling rate becomes more evident and the cooling rate after transformation deviates farther from the set one.

When the dilatometric samples were cooled in air or vacuum, a huge difference appeared. In the case of 1K/s under vacuum, only one deviation on the extension versus temperature was observed. For the same cooling rate in air, the first deviation was much less evident compared with samples cooled in helium. Figure 6.2 shows this difference.

Figures 6.2 to 6.7 show that the first deviation on the extension versus temperature curve for samples cooled in helium and air was getting smaller as the cooling rate increased. They also show that when the samples were cooled under vacuum the curve extension versus temperature had a reversion, even for very low cooling rates. In other words, at the same time that the sample was expanding its length, the temperature was increasing. Here, this phenomenon is due to the exothermic austenite to pearlite reaction. For vacuum, this phenomenon occurred at 3K/s; for air

at 6K/s; and for helium, 12K/s. This phenomenon can be attributed to the fact that helium has the highest thermal conductivity when compared to air and vacuum.

As the pearlitic reaction is exothermic, it gives off heat. Therefore, helium extracts heat out of the sample with efficiency. On the other hand, air does not do it so efficiently, and vacuum even less. Therefore, the heat is held in the sample giving rise to a heat accumulation. This leads to an increase of temperature and the reverse on the curve that it is observed.

Figure 5.31 shows that for low cooling rates, the atmosphere can determine the amount of the proeutectoid cementite formed on the austenitic grain boundaries. For a very low cooling rate, i.e., 1K/s, much less cementite was formed when the samples were cooled within a vacuum. This effect disappears at a cooling rate of 9K/s. As the austenite to proeutectoid cementite is an exothermic reaction, it gives off heat. Therefore, helium removes this heat very efficiently. In this way, it helps the reaction to occur. Therefore, more proeutectoid cementite is formed.

On the other hand, when samples are cooled within vacuum, when the austenite to proeutectoid cementite reaction starts, the heat that was supposed to be given off is held in the sample since the environment is not able to remove it. Therefore, the rate of reaction is decreased. Here, much less cementite is formed.
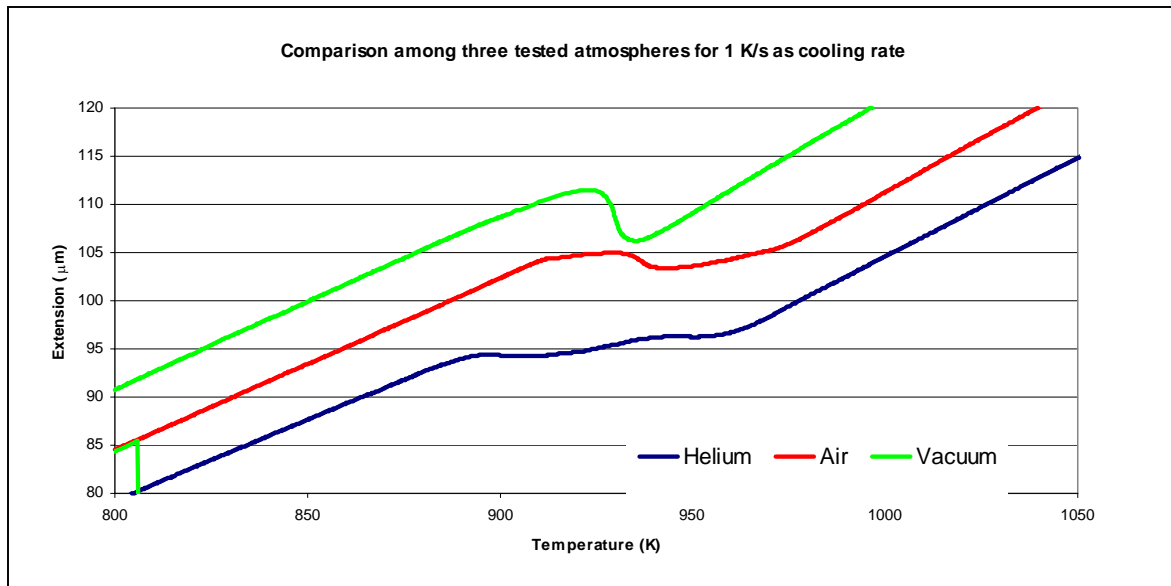
Figura 6.2 – Extension versus temperature curve for the three tested atmospheres for a cooling rate of 1K/s
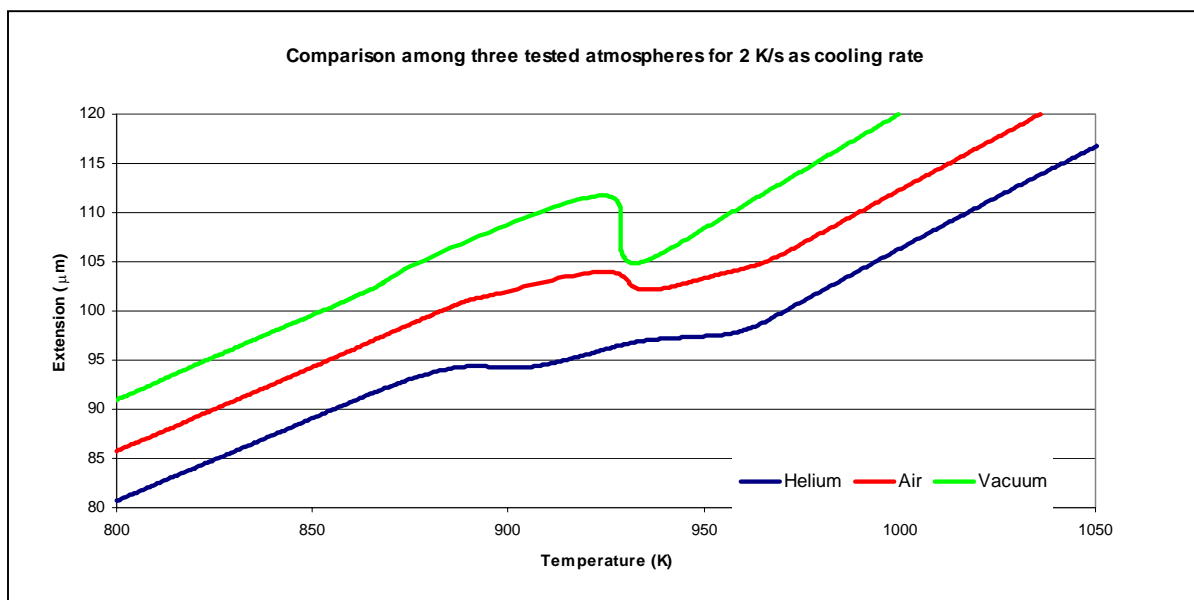
Figura 6.3 – Extension versus temperature curve for the three tested atmospheres for a cooling rate of 2K/s
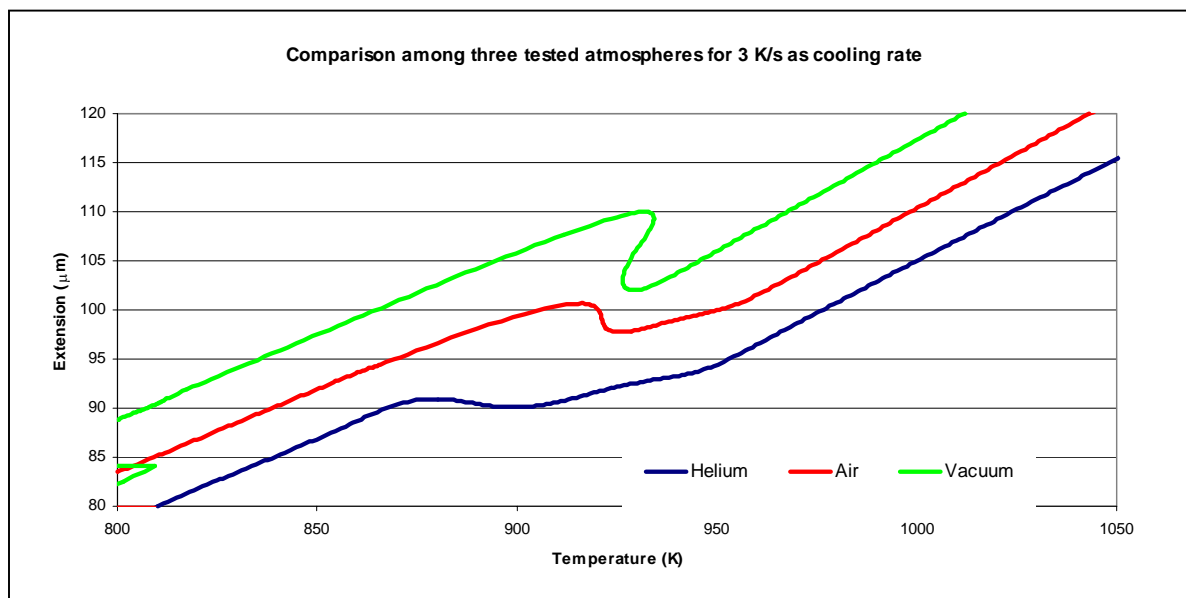
Figura 6.4 – Extension versus temperature curve for the three tested atmospheres for a cooling rate of 3K/s.
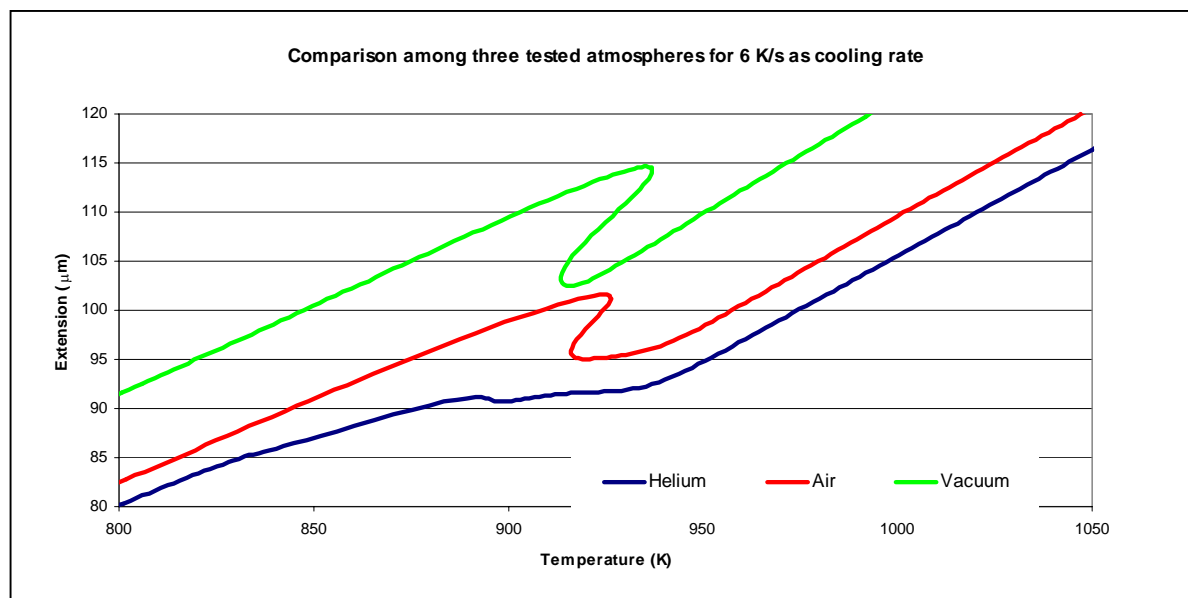
Figura 6.5 – Extension versus temperature curve for the three tested atmospheres for a cooling rate of 6K/s
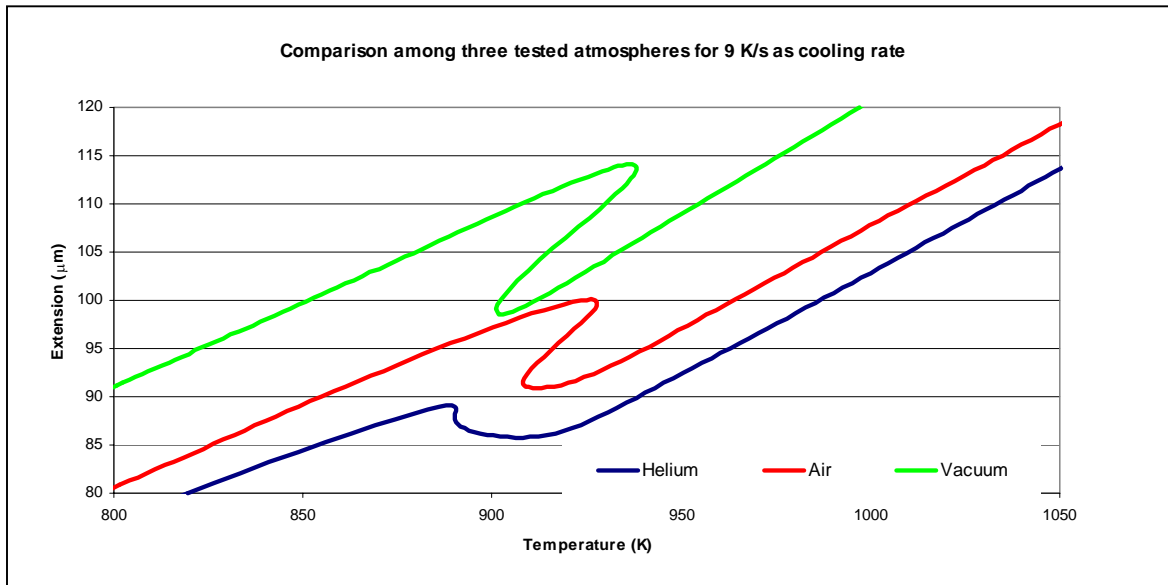
Figura 6.6 – Extension versus temperature curve for the three tested atmospheres for a cooling rate of 9K/s.
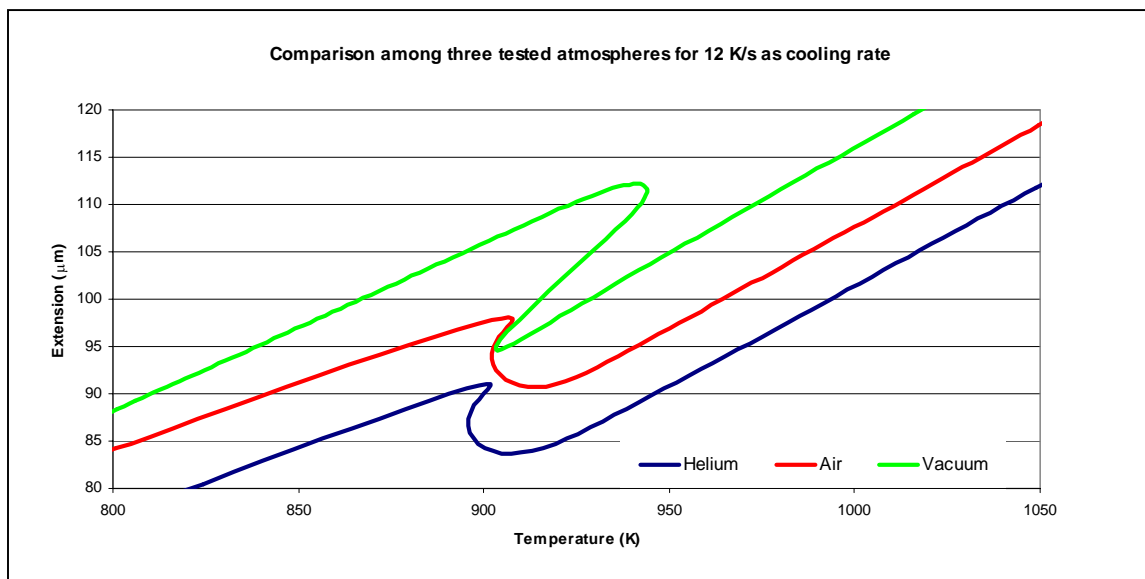
Figura 6.7 – Extension versus temperature curve for the three tested atmospheres for a cooling rate of 12K/s.

Figure 5.17 shows that 12K/s is the minimum cooling rate necessary to avoid the formation of the proeutectoid cementite. Besides this, for low cooling rates (up to 3K/s), it also shows that between the end of the proeutectoid cementite formation and the beginning of the pearlite formation there is a gap where no reaction is happening. The reason to draw this gap is very clear in Figure 5.9. This gap is seen in the magnified region of the CCT diagram in Figure 6.8.
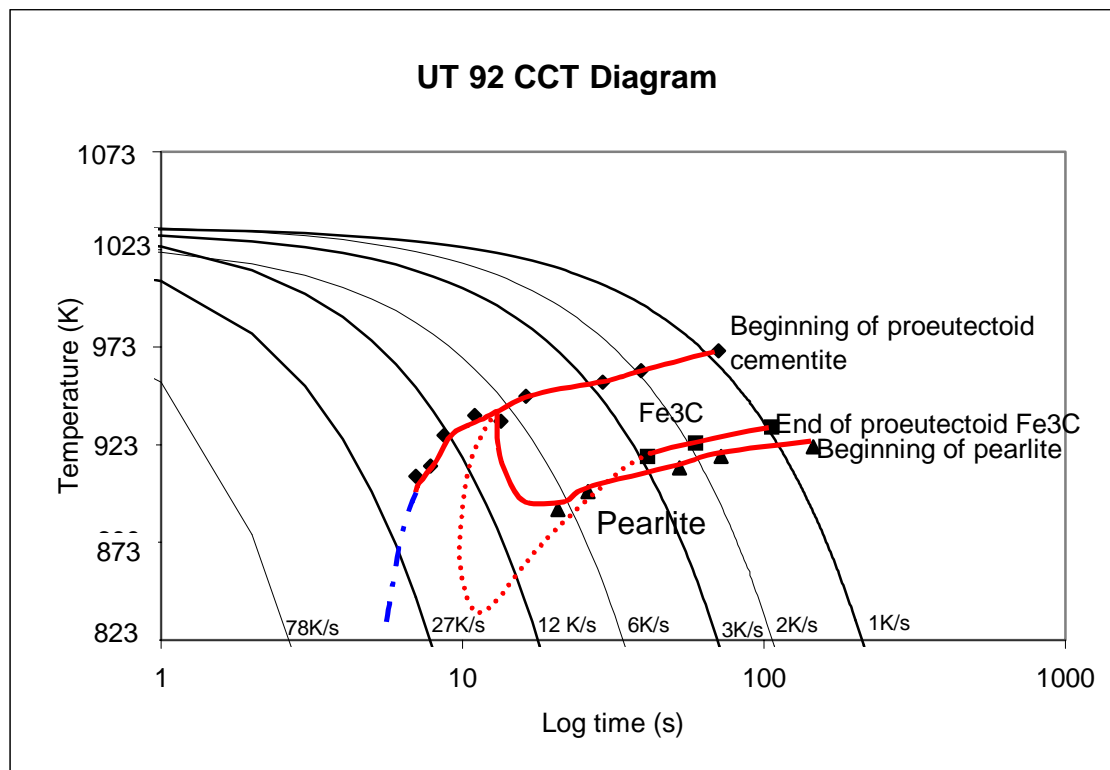
Figura 6.8 – Magnified region of the CCT diagram for SAE 1092.

Figure 6.9 shows that the beginning of pearlite formation for low cooling rates (1, 2, 3, 6, and 9K/s) is shifted upwards when helium is compared either with air or vacuum. However, this difference disappears when the cooling rate is 12K/s. This point characterizes the end of the proeutectoid cementite transformation when the dilatometric samples are cooled in helium.

UT 92 CCT Diagram
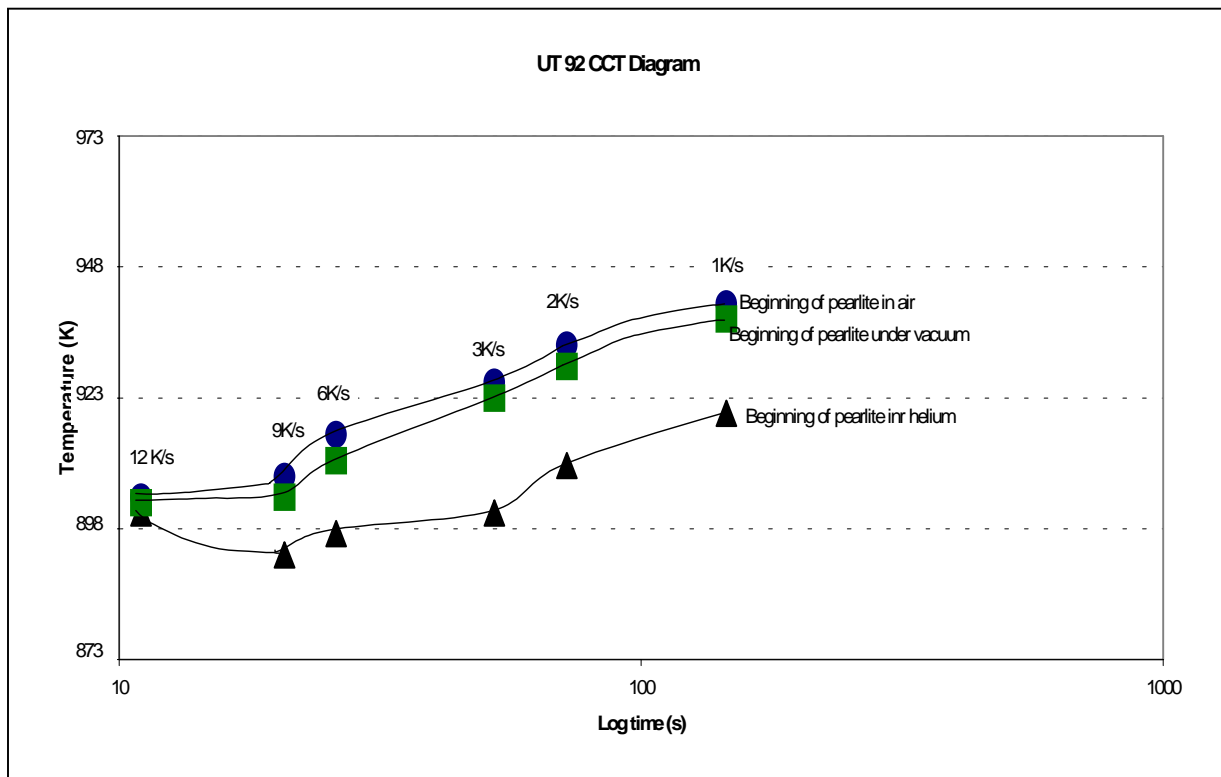
Figura 6.9 – Beginning of the pearlite formation for helium, air, and vacuum using cooling rates of 1, 2, 3, 6, 9, and 12K/s.

S. Gialanella et al.,[47] has been studying the effect of some processing parameters, such as heating rate, pre-sintering compaction pressure, and atmosphere, on the properties of materials obtained by the powder metallurgy process.

In one of the binary materials tested, (Ni-25Al at %), the vacuum in the dilatometer was replaced by hydrogen. The amount of the intermetallic phase, (Ni_3Al), formed was considerably reduced.

Two possible reasons were postulated by the authors in order to justify this effect of the hydrogen atmosphere:

1. The enthalpy of the reaction had been removed by the hydrogen flux. Doing so, the total heat developed by the solid state is too small to trigger the liquid phase formation;

2. Some NiH_2 could be formed at high temperatures in competition with the intermetallic phase. However, hydrides are not stable at room temperature, therefore they were not detected.

The former one is usually detected in high carbon steels, i.e., eutectoid steels with small cooling rates.

6.4 INDUSTRIAL RESULTS

6.4.1 Laying head temperature tests

Laying head temperature is measured at the end of the rolling mill when the wire rod is being coiled. The first idea was to decrease the laying head temperature as much as possible in order to decrease the time for the formation of proeutectoid cementite. However, decreasing the laying head temperature decreased the cooling rate drastically, from 2.4*V to 7.5*V K/s. This is not the proper way to avoid the formation of the proeutectoid cementite according to the dilatometric

110

experiments presented in this work. It was shown that the higher the cooling rate, the easier it is to suppress the formation of the proeutectoid cementite.

The results of the proeutectoid cementite presented in Tables 5.2 and 5.3 showed that when the laying head temperature was decreased, the amount of proeutectoid cementite formed close to the surface increased significantly, from 0.82 to 9.2 in the head of the coil and from 9.56 to 11.48 in the tail of the coil. Therefore, the first idea of decreasing the laying head temperature was going in the wrong direction.

6.4.2 Results from the Statistically Designed Experiments

The first positive response of this experiment was that no proeutectoid cementite was detected close to the surface of the wire rods. This is attributed to the fact that using high laying head temperature, the heterogeneity of the misorientation profile along the perimeter of the wire rod detected in the EBSD results was eliminated. Therefore, that recrystallized region where the proeutectoid cementite network was precipitated should not exist any more. This consideration has to be confirmed with further EBSD analyses along the perimeter of 11.5mm diameter wire rods free of proeutectoid cementite network.

According to the dilatometric experiments, the higher the cooling rate, the easier it is to suppress the formation of the proeutectoid cementite. Therefore, from Figure 5.33, the chosen levels for the two tested variables should be:

➢ High speed of the cooling conveyor;

➢ High laying head temperature.

These two variables controlled in these two levels are going to maximize the cooling rate, thereby helping to promote the suppression of the proeutectoid cementite.

The second and most important response is the amount of proeutectoid cementite precipitated in each condition. Now, in order to minimize the response, the chosen levels were the ones which gave smaller amounts of precipitated proeutectoid cementite. Therefore, from Figure 5.34, the chosen levels for the three tested variables should be:

➢ High speed of the cooling conveyor;

➢ High laying head temperature;

➢ Low electromagnetic stirring.

The last response is the tensile strength in each condition. Now, in order to maximize the response, the chosen levels were the ones which gave higher tensile strength. Therefore, from Figure 5.35, the chosen levels for the three tested variables should be:

➢ High laying head temperature;

➢ High electromagnetic stirring.

As the speed of the cooling conveyor showed almost no influence on the tensile strength, the chosen level is going to be based only on the amount of formed proeutectoid cementite.

The electromagnetic stirring showed a conflict between the amount of precipitated proeutectoid cementite and the tensile strength. As the main goal here is to suppress the formation of the proeutectoid cementite, the chosen levels for each variable to process the SAE 1092, are:

➢ High speed of the cooling conveyor;

➢ High laying head temperature;

➢ Low electromagnetic stirring.

Using these parameters at Belgo's plant, it is possible to produce the SAE 1092 steel grade completely free of proeutectoid cementite network.

7.0 CONCLUSIONS

According to the results obtained in this study, the following conclusions can be drawn:

- ➢ The cause of the formation of the proeutectoid cementite network close to the surface of the wire rod is different from the one precipitated in the center. Here, it was concluded that the formation of the network close to the surface of the wire rod occurs because of the higher misorientation profile among grains of the region where the proeutectoid cementite is present. The formation of the proeutectoid cementite occurs more easily at grain boundaries with high angles.

- ➢ Dilatometric results showed that the environment in which the sample is cooled reveals the amount of precipitated proeutectoid cementite when low cooling rates are used (up to 9K/s).

- ➢ The minimum cooling rate necessary to avoid the formation of the proeutectoid cementite network at Belgo's standard process is 2.8*V K/s.

- ➢ All proeutectoid cementite can be eliminated by the proper design of cooling parameters in the industrial plant, even for large size (11.5mm diameter) wire rod.

8.0 PROPOSED FUTURE WORK

Perform EBSD analyses on the 11.5mm diameter wire rods free of proeutectoid cementite network close to the surface along the perimeter to check whether any recrystallized region is detected. This analyses must be carried out on wire rods processed under the new set of conditions.

BIBLIOGRAPHY

1) E. Grethen. A Quarter Century of Steel Cord Manufacture State-of-the Art Technology and Critical Topics for the Future. Metallurgy, Processing and Applications of Metal Wires. p. 97-107.

2) J. Lombaerts. Rod Requirements for Steel Cord filaments. Wire Industry. 1974. p.471-472.

3) M. Kaiso, N. Ibaraki, Y. Oki and T. Minamida, Wire Journal International, Feb. 2002, p. 116-121.

4) Y. Kanetsuk, N. Ibaraki and S. Ashida: ISIJ International, Volume 31, 1991, p. 304.

5) D. R. Lesuer, C. K. Syn, O. D. Sherby, D. K. Kim and W. D. Whittenberger. Mechanical Behavior of Ultrahigh Strength, Ultrahigh Carbon Steel Wire and Rod. Thermomechanical Processing and Mechanical Properties of Hypereutectoid Steels and Cast Irons. p. 175-188.

6) D. K. Nesterov, N. F. Levchenko, V. E. Sapozhkov, and A. I. Schevchenko. Properties of Heat Treated Rails from Continuously Cast Blooms of Hypereutectoid Steel. Steel Translation. Volume 22 N° 4, April 1992, p. 10,1-192.

7) R. W. Heckel and H. W. Paxton. Rates of Growth of Cementite in Hypereutectoid Steels. Trans. Am. Soc. AIME, Volume 218, 1960, p. 799.

8) W. F. Smith. Structure and Properties of Engineering Alloys. McGraw Hill, Second Edition, 1993.

9) A. J. DeArdo, C. I. Garcia, and E. J. Pamiere, Heat Treatment of Steel – Thermomechanical Processing of Steel, p. 237 – 255.

10) E. M. Taleff, C. K. Syn, D. R. Lesuer, and O. D. Sherby – Metalurgical and Materials Transactions A – Volume 27 A, January 1996, p. 111 – 118.

11) Metals Handbook. Metallographic Techniques and Microstructures. Eighth Edition. p. 178

12) W. S. Owen. The Carbide Phase in Iron-Carbon-Silicon Alloys. Journal of the Iron and Steel Institute. February 1951, p. 117

13) E. J. Fasika, On the Cementite Structure – University of Pittsburgh, 1965.

14) W. J. Kim and O. D. Sherby. Tensile Elongation Behavior of Fine-Grained Fe-C Alloys at Elevated Temperatures. Thermomechanical Processing and Mechanical Properties of Hypereutectoid Steels and Cast Irons. p. 209-218.

15) F. G. S. Araujo, B. M. Gonzalez, P.R.Cetlin, A. R. Z. Coelho, and R. A. Mansur. Cementite decomposition and the second stage static strain aging of pearlitic steel wires. Wire Journal International, February 1993, p. 191-194.

16) M. A. Mangan and G. J. Shiflet. The Pitsch-Petch Orientation Relationship in Ferrous Pearlite at Small Undercooling. Metalurgical and Materials Transactions A. Volume 30A, November 1999. p. 2767-2781.

17) M. V. Kral and G. Spanos. Three Dimensional Morphology of Cementite Precipitates. Scripta Materialia, Vol. 36, Nº 8, pp 875-882. 1997.

18) C. M. Bae, Y. J. Song, and S. W. Yim. Pearlitic steel wire rods with low cementite volume fraction for direct drawing. Posco. Korea. p. 157-163.

19) Metals Handbook. Microstructures, Processing, and Properties of Steel. Eighth Edition. p. 129.

20) I. Ochiai, S. Nishida and H. Tashiro, Effects of metallurgical factors on strengthening of steel tire cord, Wire Journal International, p. 50-61.

21) J. D. Baird and R. R. Preston Research Center (Scotland), Meadow Road, Motherwell, UK. Relationships Between Processing, Structure And Properties in Low Carbon Steels – Processing and Properties in Low Carbon Steels, p. 1-26

22) W. C. Leslie and G. C. Rauch. Precipitation of Carbides in Low-Carbon Fe-Al-C Alloys. Metallurgical Transactions A, Volume 9A, 1978, p.343.

23) D. A. Porter and K. E. Esaterling. Phase Transformations in Metals and Alloys. Second Edition. P. 326-334.

24) F. Rhines. Phase Diagrams in Metallurgy. Chapter5 - Binary Eutectoid Systems, p.57-71.

25) www.webelements.com

26) J. P Houin, A. Simon and G. Beck. Relationship between Structure and Mechanical Properties of Pearlite between 0.2 % and 0.8% C. Trans. Iron Steel Inst. Jpn., 1981, p. 726-731.

27) K. Han, G. D. W. Smith, and D. V. Edmonds. Pearlite Phase Transformation in Si and V Steel. Metallurgical and Materials Transactions A. Volume 26A, July 1995 p.1617-1631.

28) Y. Yamaoka, K. Hamada, H. Tsubono, H. Kawakami, Y. Oki and Y. Kawaguchi. Development of Galvanized High-strength High-carbon Steel Wire. Transactions ISIJ, Vol. 26, 1986. p. 1059-1064.

29) H. Tashiro, T. Yamasaki, H. Sato, T. Takahashi and T. Tarui. Alloying effect on the Strength of Directly Annealed Steel Wire rods. Transactions ISIJ, Volume 28, 1988. p. 29.

30) C. E. Lacy and M. Gensamer. The Tensile Proprieties of Alloyed Ferrites. Trans. ASM, Volume 32. 1944. p. 88-105.

31) T. Ando and G. Krauss. The Effect of Phosphorus Content on Grain Boundary Cementite Formation in AISI 52100 Steel. Metallurgical Transactions A, Volume 12A, 1981. p. 1981-1283.

32) S. K. Ray, S. Mishra and O. N. Mohanty. Magnetic Aging Characteristics of a Phosphorous-Bearing Low Carbon Steel. Scripta Metallurgica, Volume 15, 1981, p. 971-973.

33) S. K. Ray, S. Mishra and O. N. Mohanty. TEM Study of Carbide Precipitation in a Phosphorous-Bearing Low-Carbon Steel. Scripta Metallurgica, Volume 16, 1982, p. 43-47.

34) J. A. Wasynczuk, R. M. Fisher and G. Thomas: Metallurgical Transactions A, Volume 17A 1986, p. 2163-2173.

35) G. Fourlaris, A. J. Baker and G. D. Papadimitriou. Effect of Copper Additions on the Isothermal Bainitic Transformation in Hypereutectoid Copper and Copper-Nickel Steels. Acta Materialia. Volume 44, N° 12, 1996, p. 4791-4805.

36) Y. Ichida. 21st Century Trends in Steel Wire rod and Bar. Kobelco Technology. Review Nº 25 April 2002. p.3-7.

37) M. E. Nicholson. Solubility of Boron in Fe_3C and Variation Of Saturation Magnetization, Curie Temperature, And Lattice Parameter of $Fe_3(C,B)$ With Composition. Journal of Metals. January 1957. p. 1-6.

38) L. Lanier, G. Metauer, and M. Moukassi. Microprecipitation in Boron-Containing High-Carbon Steels. Mikrochimica Acta. 1994. p. 353-361.

39) K. Han, T.D. Mottishaw, G. D. W. Smith, D.V. Edmonds, A. G. Stacey. Effects of vanadium additions on microstructure and hardness of hypereutectoid pearlitic steels. Material Science and Engineering A. 190, 1995, p. 207-214.

40) K. Han, D. V. Edmonds, and G. D. W. Smith. Optimization of Mechanical Properties of High-Carbon Pearlite Steels with Si and V Additions. Metallurgical and Materials Transactions A. Volume 32A, June 2001. p.1313-1324.

41) S. G. Lewis. Cold Work Embrittlement in Strip Steels. University of Wales. Oct. 1998.

42) G. A. Chadwick, and D. A. Smith. Grain Boundary Structure and Properties – London ; New York : Academic Press, 1976, p. 265-299.

43) D. McLean. Grain Boundary in Metals. Oxford, Clarendon Press, 1957, p. 116-149.

44) A. F. Gourgues. Electron Backscatter Diffraction and Cracking. Materials Science and Technology. February 2002. Volume 18. p. 119-133.

45) M. C. Kim, Y. J. Oh, and J. H. Hong. Characterization of Boundaries and Determination of Effective Grain Size in Mn-Mo-Ni Low Alloy Steel from the View of Misorientation. Scripta Materialia. Volume 43 2000. p. 205-211.

46) F. Boratto. BASIC para Engenheiros e Cientistas, Third Edition, LTC Editors, 1987.

47) S. Gialanella, L. Lutterotti, A. Molinari, J. Kazior, and T. Pieczonka. Reaction-sintering of intermetallic alloys of the Ni-Al-Mo system. Intermetallics 8, 2000, p. 279-286.